Rainfall-Runoff Modeling Under Changing Climate and Land Use Land Cover: A Case of Mille River Watershed, Lower Awash Sub-Basin, Ethiopia

Hussen Mohammed Dagne

A Thesis Submitted to the Department of Water Resources Engineering,

College of Civil Engineering and Architecture

Presented in Partial Fulfillment of the Requirements for the Degree of Master of Science in Water Resource Engineering (Hydraulic Engineering)

Office of Graduate Studies

Adama Science and Technology University

March, 2025

Adama, Ethiopia

Rainfall-Runoff Modeling Under Changing Climate and Land Use Land Cover: A Case of Mille River Watershed, Lower Awash Sub-Basin, Ethiopia

Hussen Mohammed Dagne

Advisor: Abdulkerim Bedewi (PhD)

A Thesis Submitted to the Department of Water Resources Engineering,

College of Civil Engineering and Architecture

Presented in Partial Fulfillment of the Requirements for the Degree of Master of Science in Water Resource Engineering (Hydraulic Engineering)

Office of Graduate Studies

Adama Science and Technology University

March, 2025

Adama, Ethiopia

DECLARATION

I hereby declare that this Master Thesis entitled "**Rainfall-Runoff modeling Under Changing Climate and Land use Land Cover: A case of Mille River Watershed, Lower Awash Sub-Basin, Ethiopia**" is my original work. That is, it has not been submitted for the award of any academic degree, diploma or certificate in any other university. All sources of materials that are used for this thesis have been duly acknowledged through citation.

Hussen Mohammed Dagne	______________________	_______________
Name of the student	Signature	Date

RECOMMENDATION

I, the advisor(s) of this thesis, hereby certify that I have read the revised version of the thesis entitled "**Rainfall-Runoff modeling Under Changing Climate and Land use Land Cover: A case of Mille River Watershed, Lower Awash Sub-Basin, Ethiopia**" prepared under my/our guidance by **Hussen Mohammed Dagne**. Submitted in partial fulfillment of the requirements for the degree of Mater's of Science in Water Resources Engineering (Hydraulic Engineering). Therefore, I recommend the submission of revised version of the thesis to the department following the applicable procedures.

Abdulkerim Bedewi (PhD)	__________________	_____________
Major Advisor	Signature	Date

APPROVAL PAGE OF M.Sc. THESIS

I, the advisors of the thesis entitled "**Rainfall-Runoff modeling Under Changing Climate and Land use Land Cover: A case of Mille River Watershed, Lower Awash Sub-Basin, Ethiopia**" developed by Hussen Mohammed Dagne, hereby certify that the recommendation and suggestions made by the board of examiners are appropriately incorporated into the final version of the thesis.

________________________	______________________	_______________
Major Advisor/Supervisor	Signature	Date

We, the undersigned, members of the Board of Examiners of the thesis by Hussen Mohammed Dagne have read and evaluated the thesis entitled "**Rainfall-Runoff modeling Under Changing Climate and Land use Land Cover**" and examined the candidate during open defense. This is, therefore, to certify that the thesis is accepted for partial fulfillment of the requirement of the degree of Master of Science in Water Resources Engineering (Hydraulic Engineering).

________________________	______________________	_______________
Chairperson	Signature	Date
________________________	______________________	_______________
Internal Examiner	Signature	Date
________________________	______________________	_______________
External Examiner	Signature	Date

Final approval and acceptance of the thesis is contingent upon submission of its final copy to the Office of Postgraduate Studies (OPGS) through the Department Graduate Council (DGC) and School Graduate Committee (SGC).

________________________	______________________	_______________
Department Head	Signature	Date
________________________	______________________	_______________
School Dean	Signature	Date
________________________	______________________	_______________
Office of Postgraduate Studies, Dean	Signature	Date

ACKNOWLEDGMENTS

First and for the most, I want to express my enormous thanks and praise be unto the almighty Allah who gave me all the courage and power to finish my graduate studies successfully. Very special thanks to my supervisor Abdulkerim Bedewi Surur (PhD) for his supervision, friendly attitude, and sharing of many good ideas. Regardless of his often high workload, he always makes time to answer questions as well as give encouraging advice. You are highly appreciated.

I would moreover like to thank my friend Abdi Abdela Utur (MSc.) for his patience, helpful attitude, and sharing of his work regarding the organization of documents used in this thesis.

My appreciation also extends to Ministry of Water and Energy Department of Hydrology as well as the National Meteorological Agency of Ethiopia for providing all required data for my study free of charge. I am greatly indebted to my friends: Hashim Siraj, Mohammed Hassen, and Amana Meko for their valuable ideas, encouragement, and technical and moral support during my thesis writing.

Last but not least, I want to thank the staffs of Adama Science and Technology University in general in particular for their admitting and serving me in all aspects during my study. Finally, yet importantly, my thanks go to my parents, relatives, and friends who helped me in one way or another during the study. I am strongly indebted to my mom Safia Keso, Grandmother Maryam Musa, and my wife Chaltu Nejash, who toiled hard to offer me the opportunity of education from the very beginning.

TABLE OF CONTENTS

LIST OF TABLES

Table……………………………………………………………………………………..………Page

LIST OF FIGURES

LIST OF TABLES IN APPENDIX

Appendix Table…......……………………………………………………………..….Page

LIST OF FIGURES IN THE APPENDIX

Appendix Figure…......…………………………………………………….……………..… Page

LIST OF ABBREVIATION AND ACRONYMS

CanESM5	Canadian Earth System Model version 5
CMIP6	Coupled Model Inter-Comparison Project Phase 6
ERDAS	Earth System Data Analysis System
DEM	Digital Elevation Model
EROS	Earth Resources Observation and Science
GIS	Geographic Information System
HRUs	Hydrological Response Units
FAO	Food Agriculture and Organization
IPCC	Inter Government Panel on Climate Change
SRES	Special Report on Emission Scenarios
LARB	Lower Awash River Basin
ITCZ	Intertropical Convergence Zone
ASF	Alaska Satellite Facility
GHG	Greenhouse Gases
LULC	Land Use Land Cover
MOWE	Ministry of Water and Energy
SSP	Shared Socio-Economic Pathway
CMIP5	Coupled Model Inter-Comparison Project Phase 5
GCM	General Circulation Model
SDSM	Statistical Downscaling Model
NASA:	National Aeronautics and Space Administration
NMI	National Meteorological Institute
NSE	Nash and Sutcliffe Simulation Efficiency
RCP	Representative Concentration Pathways
SWAT	Soil and Water Assessment Tool
SWAT-CUP	SWAT-Calibration Uncertainty program
USGS	United States Geological Survey
AGRL	Agricultural Land-Generic
BARR	Barren
FRSD	Forest-Deciduous
FRST	Forest-Mixed
IDRISI	Integrated Development for Remote Sensing and Image Interpretation
IPCC	Intergovernmental Panel on Climate Change
Ls9	Landsat 9
RNGB	Range-Brush
RNGE	Range-Grasses
URBN	Urban
WATR	Water Body
AR5	Fifth Assessment Report

AW	Awash Watershed
BELG	Small Rainy Season (February to May)
ETM+	Enhanced Thematic Mapper Plus (Landsat Satellite Sensor)
HWSD	Harmonized World Soil Database
M-K Test	Mann Kendall Trend Test
SDSM Ver.4.2	Statistical Downscaling Model Version 4.2
TM	Thematic Mapper (Landsat Satellite Sensor)
Km^2	Square Kilometers
M a.m.s.l.	Meters Above Mean Sea Level
KIREMT	Main Rainy Season (June to September)
BEGA	Dry Season (October to January)
SPSS	Statistical Package for the Social Sciences
HWSD Viewer	Harmonized World Soil Database Viewer
CICS	Canadian Institute for Climate Studies
WMO	World Meteorological Organization
UNEP	United Nations Environment Program
PET	Potential Evapotranspiration
MODIS	Moderate Resolution Imaging Spectrum-radiometer
GHCN	Global Historical Climatology Network
GHCN	Global Historical Climatology Network Daily
LULCC	Land Use Land Cover Change
RUSLE	Revised Universal Soil Loss Equation
SRM	Snowmelt Runoff Model
MIKE-SHE	Hydrological Modeling System by DHI (Danish Hydraulic Institute)
CASC2D	Cascading Overland Flow and Infiltration Model
WATFLOOD	Watershed Flood Forecasting Model
HEC-HMS	Hydrologic Engineering Center Hydrologic Modeling System
TOPMODEL	Topography-based hydrological MODEL
MODFLOW	Modular Groundwater Flow Model
ANN	Artificial Neural Network

ABSTRACT

The rainfall-runoff model is a crucial and necessary tool for water resources management. Both climate change and land use land cover (LULC) dynamics are critical factors influencing hydrological processes by altering groundwater recharge and river flow. This study investigates the impacts of land use/land cover (LULC) changes and climate change on rainfall-runoff processes in the Mille River Watershed, Ethiopia, using the SWAT hydrological model. Historical LULC changes (2000, 2010, and 2020) were analyzed using remote sensing data, while future LULC scenarios for 2030 and 2050 were projected using the CA-Markov model. Past trends revealed significant agricultural expansion and settlement growth, which increased mean annual flow by 1.26%, wet-season flow by 2.68%, but decreased dry-season flow by 2.22%. Future LULC changes are projected to cause a 1.19% increase in mean annual flow, with wet-season flow rising by 2.9% and dry-season flow declining by 3.14%. Climate projections, derived from the CanESM5 model under SSP2-4.5 and SSP5-8.5 scenarios, indicate increases in mean annual precipitation by up to 15% and mean annual maximum temperature by 1.05°C (SSP5-8.5) by 2050. These changes are expected to increase mean annual flow by 7.63% (SSP2-4.5) and 8.13% (SSP5-8.5) in the near term (2025–2055), with slightly greater increases in the mid-term (2056–2085). The combined effects of LULC and climate change show a more pronounced increase in streamflow compared to their individual impacts. However, climate change emerges as the dominant driver due to its widespread and persistent alterations in precipitation patterns and temperature regimes, which directly influence the hydrological cycle beyond localized land cover changes. SWAT model calibration and validation yielded reliable performance metrics, with NSE = 0.78 and R^2 = 0.82 during calibration and NSE = 0.75 and R^2 = 0.79 during validation. The results highlight the need for integrated watershed management strategies to mitigate the risks of increased streamflow, flooding, and water scarcity. Sustainable land management, afforestation, soil conservation measures, and adaptive climate strategies are essential for ensuring long-term water security and resilience in the Mille River Watershed.

Keywords: Rainfall-runoff model, LULC, Climate change, SWAT, SDSM, IDRISI, SSP, ERDAS

1. INTRODUCTION

1.1. Background

Ethiopia, frequently known as the water tower of East Africa, is primarily comprised of mountainous terrains. In these landscapes, the process of precipitation-runoff plays a pivotal role in determining the availability of surface water. It is imperative to comprehend the mechanisms behind rainfall-runoff processes to effectively control erosion and improve agricultural productivity (Tesfa and Tripathi, 2016).

Rainfall-runoff models are commonly employed to evaluate the effects of climate change, climate variability, and land management on streamflow and other hydrological processes. These models are frequently calibrated using historical observations to empirically assess their performance (Tassew et al., 2019). A precise comprehension of rainfall-runoff processes is vital for estimating runoff within a watershed under evolving climate and land use/land cover conditions. This understanding plays a critical role in sustainable water resources planning and management (Tassew et al., 2019).

ARB is one of Ethiopia's most significant river systems, providing critical water resources for irrigation, domestic use, and industrial activities. The basin spans diverse climatic zones, from the highlands to arid lowlands, making it highly susceptible to both climate and LULC changes (Gebrechorkos et al., 2020). It plays a vital role in sustaining regional water availability, particularly in arid and semi-arid zones where surface water is a primary resource for local livelihoods (Haile et al., 2022). Given the region's dependence on seasonal rainfall, any changes in climate and LULC can significantly impact water availability, flooding, and ecological stability, necessitating a deeper understanding of rainfall-runoff processes.

Recent studies highlighted the increasing influence of climate change on rainfall and temperature patterns across country. These changes have intensified hydrological variability, prolonged dry seasons, and increased flood risks. Climate models project that rising temperatures and shifts in precipitation patterns under significantly increase wet-season flows while reducing groundwater recharge, exacerbating water scarcity in dry periods (Mekonnen et al., 2022). Unlike localized LULC changes, climate change disrupts the entire hydrological cycle by altering precipitation intensity, evapotranspiration rates, and seasonal water distribution, making it a dominant driver of watershed hydrology.

While climate change exerts large-scale influences, LULC changes driven primarily by agricultural expansion and urbanization also play a crucial role in modifying runoff processes (Dibaba et al., 2020). In the study Watershed, these transformations have led to a rise in mean annual flow and reduced infiltration rates. However, compared to climate change, LULC changes tend to have localized and short-term effects, whereas climate-driven shifts in temperature and precipitation have broader and longer-lasting consequences (Haile et al., 2022). Streamflow, a key component of hydrology, is believed to be primarily affected by climate and LULC changes (Wuletawu et al., 2019). Watershed management models are fundamental for assessing, developing, and managing water resources. The study focuses on understanding the trends in hydrological processes under varying LULC and climate conditions using the SWAT hydrological model. Understanding the separate and combined effects of climate change and LULC on rainfall-runoff processes is essential for sustainable water resource planning in Ethiopia's river basins. In summary, climate change and LULC changes have significant impacts on hydrological processes, including precipitation, evaporation, and runoff. Water resources are under pressure due to these changes and human interventions. This study area is vulnerable to the hydrological impacts of climate and LULC changes. Analyzing the effects of these changes on rainfall-runoff patterns is essential for sustainable water resources management. The study also aims to enhance understanding and provide insights for effective planning and management of water resources in the region.

1.2. Statement of the Problem

Climate change and land use/land cover (LULC) changes have significant impacts on the hydrological cycle, altering key variables such as precipitation, temperature, runoff, infiltration, and evapotranspiration. In semi-arid and arid regions those changes can intensify water resource challenges, affecting agricultural productivity, water availability, and ecosystem stability. A warmer climate accelerates the hydrological cycle, leading to shifts in rainfall patterns, increased variability in streamflow, and changes in the magnitude and timing of runoff. Similarly, LULC changes such as deforestation, agricultural expansion, and urbanization modify watershed hydrology by altering infiltration rates and surface runoff dynamics.

Understanding the combined influence of these factors on rainfall-runoff processes is crucial for sustainable water resource planning.

Previous studies have extensively examined either the impact of climate change or LULC changes on streamflow. Research on LULC effects (Dibaba et al., 2016; Samuel et al., 2016; Gebrie et al., 2016) has shown how land conversion affects surface runoff and groundwater recharge. Similarly, studies on climate change impacts (Emiru et al., 2021; Daba et al., 2020; Mammo et al., 2017; Azari et al., 2016; Shimelash et al., 2017; Yimer et al., 2018) have projected future streamflow variations based on temperature and precipitation changes. However, analyzing these factors in isolation does not provide a comprehensive understanding of their interactions and relative contributions to hydrological changes. This study addresses this knowledge gap by integrating climate change and LULC dynamics to evaluate their combined effect on streamflow variability in the study watershed.

Changes in streamflow patterns have direct implications for water supply, agriculture, and flood risk management in downstream areas. However, there is limited research that specifically focuses on the Study Watershed within the broader Awash Basin. By examining how climate and land use changes influence runoff processes in this watershed, the study contributes to a better understanding of hydrological responses in the region.. Additionally, assessing future climate scenarios and projected LULC trends provides valuable insights for policymakers and water resource managers to develop climate-resilient adaptation strategies.

Rainfall-runoff modeling, a hydrological approach, aims to assess the runoff generated from precipitation in a watershed under the combined impacts of both factors. Accurate estimation of the transformation of rainfall into runoff requires sufficient and properly recorded historical data from river flow and rainfall gauging stations. However, the provision of such recording instruments and stations for every river is costly and challenging, not only for developing countries like Ethiopia but also for developed ones.

This study will provide essential insights into the combined impacts of climate and LULC changes on water resources, thereby informing sustainable water management in the Mille River Watershed.

1.3. Objectives

1.3.1. General Objective

The primary objective of this study is to model the rainfall-runoff processes of the Mille River watershed under the impacts of changing climate and land use/land cover using the SWAT hydrological model.

1.3.2. Specific Objectives

To achieve the general objective of this proposed study, the following specific objectives have been set:

- To detect past and predict future land use/land cover changes in the Mille watershed.
- To assess future projections of climate changes in the Mille watershed.
- To assess the separate and combined effects of climate and land use/land cover changes on rainfall-runoff processes in the Mille Watershed.

1.4. Research Questions

- How have land use/land cover changes in the Mille Watershed evolved, both in the past and future?
- What are the projected changes in temperature and precipitation and how do they impact rainfall-runoff processes in the Mille Watershed?
- What is the separate and combined effect of land use/land cover and climate change on runoff in the study area?

1.5. Significance of the Study

The rainfall-runoff model is a crucial and necessary tool for water resources management. By understanding the relationship between rainfall and runoff under changing climate and land use/land cover conditions, this research will provide valuable insights for sustainable water resources planning and management. The findings will inform decision-making processes and guide the suggestion of appropriate mitigation and adaptation strategies to address the challenges posed by climate change and land use practices. Ethiopia's natural resources are impacted by a range of interconnected factors, including agricultural expansion, population pressure, rapid urbanization, migration and resettlement, climate change, and environmental pollution (Wassie, 2020).

Land use/land cover changes and climate change significantly impact the natural resources, socio-economics, and future potential impacts of these natural resources in the watershed (Woldesenbet et al., 2018). However, to determine the effects on rainfall-runoff, it is important to understand the patterns of climate and land use/land cover changes and the hydrological processes of the watershed. Therefore, the findings of this research will strongly assist governments and decision/policy makers in planning, formulating, and implementing effective and appropriate response strategies to minimize the undesirable impacts of land use/land cover and climate change, as well as other development activities that affect socio-economic aspects in the watershed.

The significance of conducting research in this study area is substantial, as it contributes to initiatives in watershed management by enhancing the understanding of the impacts of various environmental factors, such as land use/land cover changes and climate change scenarios. These factors have the potential to bring about measurable changes in the conditions that control water yields, including rainfall, temperature, and runoff.

In general, this study is expected to fill the gaps in incorporating the impacts of land use/land cover and climate change on rainfall-runoff processes, particularly in the Mille River watershed.

1.6. Scope and Limitation of the Study

This study focuses on modeling and assessing rainfall-runoff processes in the Mille River Watershed under the influence of changing climate and land use/land cover (LULC) using the SWAT hydrological model. By utilizing historical rainfall data, LULC change data, and hydrological modeling techniques, the study investigates the relationship between rainfall and runoff. It evaluates the impacts of climate change and LULC on hydrological processes under both past and present conditions.

The research aims to comprehensively analyze the combined effects of climate change and LULC changes on the rainfall-runoff response of the watershed. It integrates historical and projected LULC and meteorological data into the SWAT model, focusing on both historical and future periods. This analysis specifically targets the Mille River Watershed within the Awash Sub-Basin, providing insights into hydrological responses under dynamic environmental conditions.

Several limitations were acknowledged in the study. The accuracy of the hydrological modeling was influenced by the quality and resolution of input datasets for soil, climate, and LULC, introducing potential uncertainties in simulating localized processes. Climate projections were based on a single General Circulation Model (CanESM5) under SSP scenarios, which constrained the ability to capture variability across multiple models. Future LULC maps, generated using the CA-Markov model, assumed consistent land-use transitions, which may oversimplify the complexity of socio-economic and policy-driven changes.

The SWAT model's assumptions, such as uniform soil properties within sub-basins and simplified groundwater-surface water interactions, may have impacted the precision of runoff and streamflow simulations. Calibration and validation were dependent on observed data with temporal and spatial limitations, potentially affecting the robustness of the model's performance. Socio-economic factors, such as population growth and water governance, were not considered, even though they can significantly influence hydrological dynamics.

Moreover, the analysis was restricted to specific time slices (2030 and 2050), which did not capture short-term variability or transitional trends. The findings are specific to the Mille River Watershed and may not be directly applicable to other regions with different conditions. Despite these limitations, the study provides crucial insights into hydrological changes and emphasizes the need for future research to integrate higher-resolution datasets, ensemble climate models, and socio-economic factors to improve reliability and applicability.

1.7. Organization of the Thesis

The thesis is structured into five chapters. Chapter One, Introduction, provides an overview of the study, including the background, problem statement, objectives, research questions, significance, and scope. Chapter two, Literature Review, examines existing studies on climate change, land use/land cover changes, and their impacts on hydrological processes. Chapter three, Materials and Methods, describes the study area, data sources, and methodologies, including the SWAT model and scenario analysis. Chapter four, Results and Discussion, presents the findings of the study and discusses them in the context of existing literature. Finally, chapter five, Conclusion and Recommendations, summarizes the key findings, highlights their implications, and offers suggestions for future research and policy interventions.

2. LITERATURE REVIEW

2.1. An Overview of Rainfall-Runoff Processes

Rainfall-runoff processes are a key component of hydrological modeling and are essential for managing water resources, flood forecasting, and watershed management. These processes, which describe how precipitation transforms into runoff and ultimately reaches water bodies, are influenced by a variety of factors such as land cover, soil type, topography, and climate conditions (McDonnell et al., 2020). Precipitation intensity, soil infiltration, land use, topography, and evapotranspiration are the primary drivers of runoff volumes. The movement of water from precipitation through infiltration to surface runoff is a multi-phase process, which can be significantly altered by human activities like urbanization and deforestation (Belete et al., 2023). In Ethiopia, factors such as complex topography, climatic variability, and land use changes create regional differences in runoff generation, with deforestation and agricultural expansion contributing to increased surface runoff and reduced groundwater recharge (Kifle et al., 2021). Global studies, such as those by Liu et al. (2022) and Xu et al. (2021), highlight the importance of vegetation cover, soil properties, and topography in determining runoff behavior, especially in areas undergoing rapid urbanization or in mountainous regions.

Modeling rainfall-runoff processes has led to the development of various approaches, from empirical models based on observed data to physically-based models that simulate hydrological processes with high accuracy (Gao et al., 2023). However, challenges persist, particularly in addressing climate change, land use changes, and data scarcity, which complicate the accurate prediction of runoff behavior. Future research should focus on overcoming these challenges, incorporating local conditions, and improving model calibration and validation to enhance the effectiveness of rainfall-runoff simulations, ensuring better water resource management and flood prediction (Jothityangkoon et al., 2021).

2.1.1. Runoff Generation Mechanism

The generation of runoff in a watershed is influenced by various factors, such as rainfall intensity, soil characteristics, vegetation cover, soil moisture content, meteorological conditions, land slope, and soil type. Rainfall duration and intensity directly affect runoff, with longer and more intense rainfall events leading to increased runoff. Vegetation cover and soil moisture content play a significant role in determining runoff, as reduced vegetation cover and soil moisture during dry periods result in increased runoff. Meteorological conditions before a storm, such as high temperature and low humidity, can increase evaporation and reduce soil moisture content, thereby affecting runoff. The slope of the land also influences the rate of runoff, with steeper slopes leading to faster flow and higher peak flows downstream. The type of soil affects runoff through its infiltration rate, as different soils have varying capacities to absorb water. Runoff is generated through three mechanisms: Horton overland flow (infiltration excess), saturation overland flow (saturation excess), and subsurface flow. The dominant mechanism depends on factors such as rainfall characteristics, soil moisture conditions, and soil properties within the watershed. Accurately predicting watershed runoff responses to rainfall events remains a major challenge (Fowler et al., 2016).

2.1.2. Review of Rainfall-Runoff Models

Rainfall-runoff models are essential tools in hydrology, simulating the transformation of rainfall into runoff within a watershed. These models visualize the water system's responses to changes in land use and meteorological events, conceptualizing the physical processes that convert rainfall to runoff through equations and parameters that describe the watershed dynamics.

Despite the complexity arising from interconnected variables, rainfall-runoff models generally consist of inputs, governing equations, boundary conditions, model processes, and outputs. The hydrologic system model serves as an approximation of the actual system, utilizing measurable hydrologic variables as inputs and outputs. Various models, ranging from empirical to conceptual, help understand and predict the relationship between rainfall and surface runoff at different scales. Key factors such as topography, watershed characteristics, soil type, and land use significantly influence runoff determination. Therefore, selecting an appropriate model is crucial for effective watershed planning and management, while acknowledging that these models are simplified representations of real-world systems (Beven, 2012).

The structure of rainfall-runoff models involves equations linking inputs and outputs, and the choice of model depends on the specific objectives of the study. Evaluating model performance and carefully selecting models are essential for accurate predictions and informed decision-making, particularly in the Mille Watershed.

Moreover, rainfall-runoff processes play a crucial role in hydrological modeling, significantly influencing water resource management, flood forecasting, and watershed management. These processes are affected by factors such as land cover, soil type, topography, and climate conditions. Various modeling approaches, including empirical, conceptual, and physically-based models, have been developed to simulate these processes. The integration of GIS and advanced data-driven models has enhanced the accuracy and applicability of these models across diverse environments. GIS-based tools like the Soil and Water Assessment Tool (SWAT) facilitate detailed analyses of land-use changes and their impacts on runoff, as demonstrated in studies of the Mula River watershed. This approach aids in understanding urban flood dynamics and emphasizes the importance of proactive flood risk mitigation measures (Jawale & Thube, 2024). Establishing relationships between rainfall, runoff, and evapotranspiration is essential for accurate runoff estimation. Research in semi-arid regions indicates that initial soil moisture content significantly influences runoff, underscoring the need for comprehensive data collection (Adhikari et al., 2022).

2.2. Land Use Land Cover Change and Overview

The terms "land use" and "land cover" are often used interchangeably but have distinct meanings. Land use refers to the intended use or management of land by human beings, while land cover refers to the physical and biophysical cover over the Earth's surface, including vegetation, water, bare soil, and artificial structures. Population growth has been a dominant driver of land use and land cover change in many developing countries, including Ethiopia (Tesfa, 2018). In Ethiopia, land is primarily used for agricultural purposes, construction of buildings and roads, and other activities. Subsistence farming is prevalent, and population growth coupled with slow technological adoption has led to deforestation and the conversion of forests into agricultural land, as well as the expansion of urban settlements. Various studies conducted in different parts of the country have documented land use land cover changes. The term Land Use/Land Cover Change (LU/LCC) is commonly used to describe modifications in the terrestrial surface, including biological and physical cover, such as vegetation, water bodies, bare land, or manmade structures (Gomez et al., 2016).

Understanding the concept of land use land cover change and its drivers, such as population growth, is essential for studying the impacts of land use on rainfall-runoff modeling. Ethiopia, like many other countries, has experienced significant Land use land cover changes, including deforestation and urban expansion. These changes have profound implications for water resources management and require their comprehensive integration into hydrological models to develop effective strategies for sustainable land use and water resources planning in the Mille River Watershed.

2.2.1. Land Use Land Cover Change in Ethiopia

Land use land cover change (LULCC) in Ethiopia has been a significant concern due to the expansion of agriculture driven by population growth and the need for subsistence farming. Studies conducted in different parts of Ethiopia have highlighted the consequences of LULCC. For instance, small-scale farmers aiming for subsistence have led to deforestation and conversion of forested areas into agricultural land (Asmamaw et al., 2013). This has resulted in soil erosion, reduced water infiltration, increased sedimentation in rivers, and decreased water availability. Similarly, Sisay et al. (2016) concluded that in the Bale mountain eco-region, extensive land-use and land cover changes were primarily driven by farm and settlement expansion between 2000 and 2020. Furthermore, (Hiywot et al., 2014), found that in the highland regions, agricultural expansion has led to the loss of vegetated lands, including shrubland, woodland, and forests, since the 1860s with worsening trends since the 1980s.

The drivers of LULCC in Ethiopia are multifaceted. Population growth, poverty, and the need for agricultural land are key drivers in rural areas. In urban areas, population growth, economic development, and infrastructure expansion play significant roles. Additionally, policy and institutional factors, such as land tenure systems, land use planning, and governance, also influence LULCC. Several studies have focused on quantifying and mapping LULCC in Ethiopia using remote sensing and GIS techniques. These studies have provided valuable insights into the extent and patterns of LULCC, as well as its impact on ecosystems and water resources. However, limited studies have specifically examined the relationship between LULCC and rainfall-runoff processes in the Mille River Watershed.

2.2.2. Land Use Land Cover Change Impact on Water Resources in Ethiopia

Land Use and Land Cover (LULC) changes have significantly impacted water resources in Ethiopia, altering hydrological processes through human activities and environmental changes. Belay et al. (2022) demonstrated that LULC changes in Ethiopia's Central Rift Valley disrupt water balance and availability, emphasizing the need for sustainable water management. Similarly, Alemu and Woldeyes (2023) identified population growth, agricultural expansion, and industrial activities as major drivers of LULC changes in the Fetam watershed, leading to notable impacts on streamflow dynamics. In the Bilate catchment, Desta et al. (2023) highlighted the importance of understanding LULC dynamics for effective water resource management, while Mekonnen et al. (2023) showed that combined effects of LULC and climate change significantly alter hydrological processes in the Birr River watershed. Yimer and Bekele (2023) assessed surface water impacts in the Laga-Arba watershed, revealing substantial quantitative changes in water resources due to LULC dynamics. These findings underscore the necessity for integrated watershed management strategies to mitigate adverse effects and ensure sustainability.

Changes in LULC notably influence runoff and groundwater flow. Asmamaw et al. (2013) found that LULC changes affect infiltration, runoff, and evaporation rates, while Adamu (2013) highlighted significant impacts on both surface runoff and groundwater flow. Getahun (2020) observed that reductions in forest and grassland, coupled with increases in agricultural and built-up areas, elevated surface runoff during wet seasons and reduced base flow during dry periods. Similarly, Gebrie et al. (2016) concluded that LULC changes disproportionately affect streamflow during wet seasons compared to dry periods. LULC dynamics also play a critical role in shaping watershed hydrology. Mengistu et al. (2022) examined the Gilgel Gibe watershed and reported that expanding cultivated land at the expense of forested areas increased surface runoff and reduced groundwater recharge. In Addis Ababa, Tesfaye et al. (2021) found that rapid urbanization converted agricultural and forest lands into urban areas, significantly altering local ecosystems and hydrological processes. Getachew et al. (2023) demonstrated the utility of modeling approaches such as CA-Markov models in predicting future LULC changes by integrating historical trends and future projections, as shown in Basona Worena Woreda. Additionally, Yihdego et al. (2022) analyzed the Upper Awash River Basin and reported that deforestation and cropland expansion intensified surface runoff and sediment yield, disrupting hydrological systems.

2.3. Description of Key Terms in Climate Change Scenario Analysis

The concept of climate change refers to changes in the state of the climate, including alterations in average weather conditions and variability over time and location (Alemu, 2011). Climate change is influenced by various factors, such as latitude, proximity to the sea, vegetation, presence of mountains, and other geographical elements. It occurs on different time scales, from seasonal variations to longer-term phenomena like ice ages.

According to the Intergovernmental Panel on Climate Change (IPCC, 2013), climate change is a sustained modification in the climate state, characterized by changes in the mean and/or variability of climate properties over a decade or more. It can result from natural and human-induced factors. Climate change is a significant global challenge, and its occurrence is widely accepted. The IPCC projects that global average temperatures may rise by 1.1 to 6.4ºC during this century, depending on greenhouse gas emissions. Since 1750, concentrations of carbon dioxide (CO2), methane (CH4), and nitrous oxide (N2O) have increased by approximately 40%, 150%, and 20% respectively (IPCC, 2014). The IPCC's 5th Assessment Report (AR5) concluded that the observed increase in global average temperature since the mid-20th century is mainly caused by anthropogenic greenhouse gas concentrations.

2.4. General Circulation Model (GCM)

General circulation models (GCMs), also called General climate models, are the primary tools for understanding global climate and projecting its change under different forcing scenarios (Tang & Xu, 2012). These models provide valuable insights into current and future predictions of climate change scenarios on a global scale. GCMs employ a 3D-grid representation, with varying horizontal resolutions for the atmospheric and oceanic components. However, their coarse resolution limits their ability to capture the effects of local forcing factors, such as terrain effects and land-sea contrasts, which modulate climate signals at finer scales (Rummukainen, 2010). While GCMs are vital resources for conducting climate change experiments and deriving climate change scenarios at regional and global scales, they do have drawbacks due to their coarse resolution. Generally, GCMs are essential tools for understanding global climate patterns and conducting climate change experiments. However, their coarse resolution poses challenges when studying local-scale impacts and adaptation. The scale mismatches, both spatial and temporal, along with vertical level mismatches and accuracy mismatches, limit the utility of

GCMs in water resources studies. Additionally, incorporating changes in land use land cover is vital for accurate rainfall-runoff modeling in river watersheds under changing climates.

2.5. Downscaling Methods

Downscaling is the process of translating climate projections from coarse-resolution Global Climate Models (GCMs) to finer-resolution Regional Climate Models (RCMs). It establishes a relationship between predicted local-scale climate variables and large-scale atmospheric variables (Wilby and Dawson, 2013). The process can increase temporal resolution (e.g., from monthly to daily values) or spatial resolution (e.g., from GCM grid cells to weather station scale). Downscaling is crucial for identifying and analyzing extreme events (Domínguez et al., 2013).

There are two primary downscaling approaches: statistical and dynamical. Statistical downscaling techniques establish a statistical relationship between large-scale climatic data and local variations using historical data (Chen, Brissette, and Leconte, 2012). This method relies on empirical relationships between historical and/or current large-scale atmospheric and local climate variables. Statistical downscaling utilizes statistical relationships that link regional climate variables to large-scale atmospheric variables (predictors). These links are determined during an observational period, tested with independent data, and used for future climate projections. The advantages of statistical modeling include the use of ensemble Global Climate Model (GCM) results. However, the main disadvantage is the need for lengthy historical meteorological data to establish an appropriate link with large-scale variables. Statistical downscaling is a simple, resource-efficient, and computationally efficient approach. It is suitable for spatial downscaling and bias correction of multiple models, with higher resolution compared to dynamical downscaling. Statistical downscaling techniques are widely used in various sectors (S.H. Gebrechorkos et al., 2019; Kaini et al., 2020).

On the other hand, dynamical downscaling involves the use of regional climate models (RCMs) with higher spatial resolution, typically 10-50 km, to capture realistic topography and land use/vegetation (Chen, Brissette, and Leconte, 2012). However, systematic errors in RCMs may require statistical corrections for realistic output, often through bias correction. Dynamical downscaling utilizes higher-resolution RCMs that respond to GCM outputs provided as boundary conditions at the edges of the RCM's spatial domain. Dynamical downscaling techniques employ local physical factors, such as topographic features nested within GCMs, to generate fine-scale Regional Climate Models (RCMs) (Endris et al., 2013). However, it requires significant resources and is time-consuming (Trzaska and Schnarr, 2014). Drawbacks include the need for powerful computing capacities and dependency on initial and boundary conditions. For the proposed study, the Statistical Downscaling Model (SDSM Ver.4.2) was utilized to construct climate change scenarios.

2.5.1. Justification for Using SDSM over RCMs

In this study, the Statistical Downscaling Model (SDSM) was chosen over Regional Climate Models (RCMs) due to their computational efficiency, flexibility, and suitability for localized climate assessments. This decision balances practicality and scientific rigor, considering the specific focus on the Mille River Watershed and its climatic characteristics.

A key advantage of SDSM is its computational efficiency. By establishing statistical relationships between large-scale atmospheric predictors from Global Climate Models (GCMs) and local-scale climate variables such as temperature and precipitation, SDSM enables rapid and efficient climate projections. This is particularly critical for studies involving multiple climate scenarios or extensive sensitivity analyses, especially in contexts with limited computational resources. Conversely, RCMs require significantly greater computational power and time, relying on complex numerical simulations of physical processes. For resource-limited research settings like this study, the high computational demands of RCMs make them less feasible (WUCA, 2018).

The decision to use SDSM was also influenced by the availability and quality of historical observational data. SDSM leverages reliable, long-term meteorological records to generate localized projections with high accuracy. In regions such as the Mille River Watershed, where dependable data is available, SDSM proves to be particularly effective. In contrast, RCMs, while capable of simulating physical processes in regions with sparse data, face challenges in producing region-specific, high-resolution outputs for areas like Ethiopia (Copernicus Climate Change Service, 2021). However, SDSM has its limitations. It does not directly simulate physical processes, which may result in the underrepresentation of complex climatic dynamics such as topographical influences or land-sea interactions. RCMs, by contrast, explicitly model these processes, offering more detailed insights into regional climate systems, especially in areas with complex terrain or localized climatic interactions. Despite this, RCMs' detailed representations come with significantly higher computational costs (Climate Extremes, 2021).

SDSM's flexibility is another significant strength, allowing researchers to customize the model for specific variables, regions, or periods. This adaptability is particularly valuable for localized studies like this one, which focuses on the Mille River Watershed. While RCMs offer comprehensive simulations, they require substantial customization and expertise to address specific research questions, further increasing their complexity and resource demands (WUCA, 2018). Both approaches involve inherent uncertainties and biases, but they handle them differently. SDSM assumes stationarity, meaning the statistical relationships between predictors and local variables remain consistent over time. This assumption may introduce uncertainties if future climate dynamics deviate significantly from historical patterns. Nonetheless, SDSM mitigates this limitation through careful calibration and validation using observed data.

On the other hand, RCMs inherit biases from their driving GCMs and introduce additional uncertainties through parameterizations of physical processes. While both methods have trade-offs, SDSM's reliance on observed data for calibration provides a practical advantage in reducing certain uncertainties (WUCA, 2018). Given the computational constraints, availability of reliable historical data, and the need for localized climate projections at the watershed scale, SDSM emerged as the most practical and effective choice for this study. Although its limitations, such as the assumption of stationarity and inability to directly simulate physical processes, are acknowledged, these are outweighed by its efficiency, adaptability, and capacity to provide reliable localized projections. In conclusion, SDSM offers an efficient, flexible, and practical approach to assessing climate change impacts at the watershed level. These attributes make it particularly well-suited for resource-constrained studies like this one, justifying its selection over RCMs.

2.6. Evaluation of General Circulation Model Simulations

Accurately and reliably simulating the climate over the African continent using GCMs and RCMs poses a significant challenge, primarily due to the complexity and diversity of the processes that need to be represented (Laprise et al., 2013). There is a scarcity of evaluation studies focusing on GCM simulation results for the major river basins in Africa. Furthermore, the skill of GCMs in simulating hydrological variables decreases compared to climate variables, even though the importance of hydrology increases in the same direction. They identified three distinct gaps related to the use of GCMs in water resources studies: spatial and temporal scale mismatches, vertical level mismatches, and accuracy mismatches (IPCC-TGICA, 2007). Based on these identified gaps, the evaluation of GCM results was conducted for historical rainfall over the Mille watershed. The evaluation focused on annual time scales to identify the most suitable model for subsequent objectives in this study. This evaluation will also enhance our understanding of the reliability of statically downscaled simulations from two climate models participating in the Coupled Model Intercomparison Project Phase 6 (CMIP6).

2.7. Climate Change Scenarios and Models

A climate scenario provides a plausible and simplified representation of future climate conditions. Decision-makers and planners have utilized climate scenarios to analyze situations where outcomes are uncertain (Bjørnæs, 2020). In climate change research, scenarios have become crucial for understanding long-term consequences (van Vuuren et al., 2011). The goal of working with scenarios is not to predict the future but to gain a better understanding of uncertainties and alternative futures, and to assess the robustness of different decisions or options across a wide range of possible futures (Wayne et al., 2013).

The Intergovernmental Panel on Climate Change (IPCC) serves as the leading international organization for assessing climate change. Established in 1998 by the United Nations Environment Program (UNEP) and the World Meteorological Organization (WMO), the IPCC aims to provide a clear scientific overview of the current understanding of climate change, its potential environmental and socio-economic impacts, and adaptation assessments. Currently, 194 countries are members of the IPCC. The IPCC has developed a series of emissions scenarios that reflect a range of driving forces and emissions, capturing current knowledge and uncertainties. Future levels of global greenhouse gas emissions stem from complex, less understood dynamic systems influenced by factors like population growth, socio-economic development, and technological progress. Consequently, accurately predicting emissions is virtually impossible. Given the uncertainties in emissions models and our understanding of key driving forces, scenarios are a useful tool for summarizing both current knowledge and uncertainties.

Socioeconomic changes, including population growth, industrial development, agriculture, and land use changes, significantly influence streamflow and water quality in watersheds. These factors can alter hydrological cycles, requiring an understanding of the future socio-economic context to assess potential impacts on water resources. Shared Socioeconomic Pathways (SSPs) provide a framework for analyzing these future socio-economic changes. SSPs are baseline scenarios that do not account for climate change or new climate policies, but they serve as useful tools to incorporate the social and economic dimensions of future developments (Kriegler et al., 2013). These pathways consider drivers such as population growth, economic development, and urbanization, though the specific impacts of these drivers are quantified in scenarios derived from the SSPs (van Vuuren et al., 2013).

The IPCC has defined five distinct SSPs to assess various socio-economic futures. These pathways include: SSP1, representing Sustainability; SSP2, representing Business as Usual; SSP3, representing a Fragmented World; SSP4, representing Inequality Rules; and SSP5, representing Regular Progress, with a focus on energy sources (IPCC, 2014). In the context of CMIP6, the primary objective is to advance and refine the parametrization of climate change projections. Several SSP combinations have been developed for use in CMIP6, building upon the previous SSP scenarios from CMIP5 (e.g., SSP119, SSP370, SSP434, SSP245, and SSP585). These updated scenarios address socio-economic elements such as population growth, economy, urbanization, and other key drivers (O'Neill et al., 2017). One of the significant improvements in CMIP6 is the expanded temperature range for equilibrium climate sensitivity (1.5–4.5°C) (O'Neill et al., 2016).

SSP245 and SSP585, in particular, predict future radiative forcing of 4.5 and 8.5 W/m^2 by the end of the 21st century, respectively. The SSP245 scenario focuses on achieving sustainable growth through global collaboration, while SSP585 represents a worst-case scenario characterized by a fossil fuel-based economy and large-scale energy development (Riahi et al., 2017). The SSP585 scenario, which represents the upper limit of projected radiative forcing (8.5 W/m^2 by 2100), illustrates a pessimistic future trajectory for climate change, reflecting the impact of a fossil-fuel-dominated economic pathway (Kriegler et al., 2017). On the other hand, SSP245 assumes the implementation of climate mitigation measures, leading to a moderate increase in radiative forcing of 4.5 W/m^2 by 2100, serving as an update to the SSP2-4.5 scenario from CMIP5 (van Vuuren et al., 2013). For this study, the SSP245 and SSP585 scenarios have been integrated into the baseline model to assess the potential impacts of climate change on the study catchment.

Representative Concentration Pathways (RCPs) have been defined as the basis for long-term and near-term climate modeling experiments in the climate modeling community (van Vuuren et al., 2011). It's a time and space-dependent trajectory of concentration and emission of greenhouse gases and pollutants resulting from human activities, including changes in land use and land cover. Emission scenarios used in climate change studies to assess the long-term impact of atmospheric greenhouse gases and pollutants are based on assumptions of population growth, economic development levels, etc. According to the Intergovernmental Panel on Climate Change (IPCC), the new generation scenario developed and later used within CMIP5 of the Fifth Assessment Report (AR5) was published in 2013-2014. This scenario is denoted by Representative Concentration Pathways (RCPs) (Van Vuuren et al., 2011). The RCPs represent the four ranges of GHG emissions scenarios, including a severe mitigation scenario (RCP2.6), two intermediate scenarios (RCP4.5 and RCP6.0), and one scenario with very high GHG emissions (RCP8.5). Each RCP defines a specific emissions trajectory and subsequent radiative forcing (Wayne, 2013).

In all SRES the assumption is reducing income alteration between world regions technology was the main driving force for demographic and economic development. The four RCP scenarios in CMIP5 have radiative forcing values ranging from 2.6 to 8.5 W/m^2 at 2100, which is a wider range than that of the three SRES scenarios available in CMIP3 (IPCC, 2013). The SRES scenarios do not assume any policy to control climate change, unlike the RCP scenarios. SSP2-4.5 and SRES B1 have similar radiative forcing at 2100, and comparable time evolution (within 0.2W/m^2). The radiative forcing of SRES A2 is lower than SSP5-8.5 throughout the 21st century, mainly due to a faster decline in the radiative effect of aerosols in SSP5-8.5 than SRES A2, but they converge to within 0.1 W/m^2 at 2100 (IPCC, 2013).

RCPs represent pathways of radiative forcing, not linked with exclusive socio-economic assumptions contrary to the Special Report on Emission Scenarios (SRES). Maloney et al. (2014) found that the four sets of GHG emission scenarios called representative concentration pathways of RCP2.6, RCP4.5, RCP6.0, and RCP8.5 of the CMIP5 have been upgraded to shared socio-economic pathways (SSPs) SSP1-2.6, SSP2-4.5, SSP4-6.0, and SSP5-8.5, respectively. The selection of climate models capable of representing future climate from the large set of existing GCMs is vital for climate impact studies for a particular area.

2.8. Climate Change Impact on Temperature, Precipitation, and Water Resources

Climate change has significantly altered global temperature and precipitation patterns, profoundly affecting ecosystems, economies, and human livelihoods. Global average temperatures have risen by approximately 1.1°C since the late 19th century, primarily due to increased greenhouse gas emissions. The warming trend has accelerated, with 2023 recorded as the warmest year since global records began in 1850, exceeding the 20th-century average by 1.18°C (National Centers for Environmental Information, 2023). Precipitation patterns globally have also shifted, becoming more variable and extreme. The frequency and severity of floods and droughts have increased, causing substantial socio-economic impacts. Recent flooding events underscore the urgency for adaptive infrastructure and advanced predictive models (Geman & Venkatraman, 2024). Economically, a global temperature increase of 3°C could reduce GDP by 10%, with low-latitude countries facing losses of up to 17% (Burke et al., 2024). These trends highlight the disproportionate burden of climate change on vulnerable nations. The Intergovernmental Panel on Climate Change (IPCC) emphasizes that mitigating climate change requires limiting global warming to 1.5°C or 2°C above pre-industrial levels. Despite mitigation efforts, certain changes, such as sea-level rise and frequent extreme weather events, are expected to persist (IPCC, 2021). Achieving these targets demands unprecedented transformations across all sectors.

In Ethiopia, these global trends manifest in acute challenges due to the country's reliance on rainfed agriculture and diverse topography. Between 1960 and 2006, Ethiopia experienced a mean annual temperature increase of 1.3°C, averaging 0.28°C per decade. Projections indicate further warming of 0.7°C to 2.3°C by the 2020s and up to 1.4°C by the 2050s, exacerbating heatwaves and droughts (Simane et al., 2022). Precipitation patterns in Ethiopia are highly variable, with two main wet seasons: spring and summer. Climate change is expected to increase rainfall variability and the frequency of extreme events such as floods and droughts. For instance, a positive Indian Ocean Dipole (IOD) in 2019 caused rainfall over East Africa to be 300% above normal, resulting in widespread flooding and landslides (Gebrehiwot & van der

Veen, 2013; Dyer et al., 2020). Additionally, a reduction in rainfall in Ethiopia's Awash Basin could lead to a 5% GDP decline in the basin, with the agricultural sector experiencing reductions of up to 10% (IPCC, 2021). Future climate change scenarios indicate that global temperatures could rise by up to 5°C by the end of this century if significant reductions in greenhouse gas emissions are not achieved (Hartmann et al., 2013). This rise will lead to further changes in precipitation, including increased variability and intensity, affecting water availability and agricultural productivity. Understanding these trends is essential for developing effective adaptation strategies tailored to Ethiopia's specific context.

Africa is considered one of the region's most vulnerable to the effects of climate change (IPCC, 2014). Developing countries, particularly those in Africa, are expected to face heightened vulnerability due to recurrent floods and droughts, which continue to cause significant suffering for millions of people (Nawaz et al., 2010). The availability of water resources is highly influenced by climate variability, and climate change presents various challenges to the Nile basin and Africa as a whole, including alterations in the hydrological cycle that can affect both the quantity and quality of regional water resources. Consequently, understanding the impacts of global climate change on regional water supplies is essential, as water is crucial for both societal well-being and environmental sustainability. Over recent decades, climate change has had a profound impact on temperature and precipitation patterns across Africa, with significant repercussions for ecosystems, agriculture, water resources, and human livelihoods.

Between 1991 and 2022, Africa experienced an average temperature increase of approximately +0.3°C per decade, surpassing the global average and marking a rise from +0.2°C per decade observed between 1961 and 1990. This warming trend has been especially pronounced in North Africa, contributing to extreme heat events and wildfires, particularly in countries like Algeria and Tunisia (World Meteorological Organization [WMO], 2024). Precipitation patterns across the continent also exhibit significant regional variability. East Africa has witnessed periods of increased rainfall, while Southern Africa has been plagued by prolonged droughts. For instance, the 2019 positive Indian Ocean Dipole (IOD) event resulted in a 300% increase in rainfall in East Africa, leading to widespread flooding and landslides. Such regional disparities highlight the growing unpredictability and variability of rainfall patterns across the continent (United Nations Framework Convention on Climate Change [UNFCCC], 2024).

The impacts of rising temperatures and altered precipitation patterns are particularly severe for agriculture and water resources. Higher temperatures exacerbate evapotranspiration, thereby reducing soil moisture and crop yields. Concurrently, changing rainfall patterns contribute to water scarcity, particularly in regions that rely heavily on rainfed and irrigated agriculture. For example, in Ethiopia's Awash Basin, reduced rainfall could lead to a 5% decline in GDP, with agricultural losses potentially reaching 10% (Intergovernmental Panel on Climate Change [IPCC], 2021). Climate change also poses significant health risks. Warmer temperatures and increased rainfall create more favorable conditions for mosquitoes and other disease vectors, thus raising the transmission rates of diseases such as malaria, dengue fever, and yellow fever, particularly in sub-Saharan Africa. These shifts underscore the need for strengthened public health systems to manage emerging risks (UNFCCC, 2024). The impacts of climate change across Africa are not uniform. For example, while the Sahel region has seen an increase in rainfall in recent years, Southern Africa continues to struggle with severe drought conditions. These variations emphasize the importance of developing region-specific adaptation strategies that consider both local climatic conditions and socio-economic factors (IPCC, 2021).

Projections suggest that global warming will continue to intensify temperature extremes, rainfall variability, and the frequency of extreme weather events such as droughts and floods. These trends underline the urgency of implementing comprehensive adaptation and mitigation strategies to protect development and ensure environmental sustainability across the continent (WMO, 2024). In conclusion, the literature reviewed highlights the significant and increasing impacts of climate change on temperature and precipitation patterns across Africa. Addressing these challenges will require coordinated efforts, including investments in climate-resilient agricultural practices, improved water resource management, and strengthened public health systems to mitigate risks and support sustainable development.

Global climate change, with its increased temperatures and altered precipitation patterns, has significant implications for water resources in Ethiopia in the twenty-first century (Azari et al., 2016). The country heavily relies on rain-fed agriculture, making it particularly vulnerable to changes in rainfall patterns. Several studies are conducted on the variation of water resources such as changes on surface runoff, ET, timing and magnitude of stream flow, flood events, and soil erosion as well as sedimentation may result from potential climate change effects in precipitation and temperatures (Chen et al., 2020; Cousino et al., 2020; Gadissa et al., 2018; Tigabu et al., 2021; Xie et al., 2021).

Another, Numerous studies have shown that streamflow and global hydrological cycles are both predicted to be impacted by climate change (Aragaw et al., 2021; Dile et al., 2013; Emiru et al., 2021; Shrestha et al., 2021; Xie et al., 2021). Similarly, another scholars (Worku et al., 2021; Yang et al., 2021) founded that, Precipitation is the source of water, and the amount of water available are determined by subtracting water loss by ET from precipitation in a watershed. In addition, Surface runoff and streamflow depend on the amount of water that is available, and the decreased precipitation can have the opposite effects, while increased precipitation may cause increased surface runoff (Dibaba et al., 2020b; Zhou et al., 2017). To address the impacts of climate change on water resources, Ethiopia has been implementing various adaptation strategies. These include the construction of water reservoirs, promoting water conservation and efficiency measures, enhancing irrigation systems, and improving water management practices.

2.12. Trend of Climate Data Analysis

Climate change poses a threat of increased temperature, evapotranspiration, and the risks associated with heat waves and droughts (Touré et al., 2017). Regional analyses have been conducted to understand extreme climate events and trends. Trend indices have shown significant increases and decreases in seasonal and annual precipitation. For example, Asfaw et al. (2017) reported a decrease in annual, Belg, and Kiremt rainfall in the Woleka sub-basin of Ethiopia. Similarly, Mekasha et al., (2014) found increasing warm extremes in temperature and precipitation in different stations across Ethiopia. Therefore, it is important to test extreme climate indices in future studies to better understand the perception of climate change, with comprehensive coverage across the country. Analyzing recent trends in climatic variables is crucial for understanding the country's climate system and serves as a vital research area for other researchers.

2.13. Hydrologic Modeling

Hydrologic modeling is a powerful technique for investigating hydrological systems, benefiting both research hydrologists and water resources engineers involved in the planning and development of integrated approaches for water resources management (Tekalegn et al., 2018). These modeling methods are widely used to quantify the impacts of climate change and land use/land cover change (Tekalegn et al., 2018). A hydrologic model applies mathematical equations to represent the physical response of a watershed to meteorological events (Rwigi, 2014). Hydrologic models have various forms and purposes, but they generally serve one of two primary objectives. These objectives include gaining a better understanding of hydrologic processes and changes occurring in a watershed, as well as predicting hydrologic processes and providing valuable information for assessing the potential impacts of changes such as land use/land cover (LULC).

2.13.1. Types of Hydrologic Models

a. **Lumped models:** Parameters in lumped models typically do not vary spatially within the basin. Consequently, these models evaluate basin response solely at the outlet and do not explicitly account for the response of individual sub-basins. Lumped models integrate data over specific time and space scales and rely on empirical relationships. While they are conceptually simple, easy to program, and apply, they require extensive calibration data and are not applicable beyond the calibration range. Examples of lumped models include WATBAL, SRM, HYRROM, SWM4, IHACRES, and others.
b. **Distributed models:** Distributed models allow parameters to vary fully in space at a resolution determined by the user. These models explicitly simulate the physical processes occurring in the watershed and integrate them to produce the watershed's response. Distributed models such as MIKE-SHE, Wetspa, CASC2D, WATFLOOD, and others can be employed to analyze changing conditions, such as land use changes, project alternatives, and climate change.
c. **Semi-distributed models:** Parameters of semi-distributed models are partially allowed to vary in space by dividing the basin into smaller sub-basins. These models combine empirical and physically-based approaches and lie between lumped and distributed models. They offer increased spatial resolution and better process descriptions compared to simple lumped parameter models, while retaining computational advantages over fully distributed, physics-based models. Examples of semi-distributed models include SWAT, HEC HMS, HPV, TOPMODEL, and others.

When selecting a hydrologic model, several criteria should be considered, including the model's ability to predict the impact of land management practices, the availability of specific information about weather, soil properties, topography, vegetation, and land management practices, the adequacy of modeling hydrological processes, and the availability of input data. For this study on the Mille River Watershed in Ethiopia, the SWAT model, a semi-distributed model, was chosen. The SWAT model was selected due to its physically-based structure, availability, and alignment with the study's objectives.

2.13.2. Application of Hydrological Model (SWAT)

Previous studies have demonstrated that the SWAT model is capable of simulating hydrological processes in complex and data-limited watersheds, yielding reasonable model performance statistics. Several studies conducted in different parts of Ethiopia have successfully calibrated and validated the SWAT model. Yimer (2018) utilized the SWAT model to evaluate the impact of climate change on streamflow in the Mille Watershed, indicating that the model accurately simulates runoff for the study area under predicted changes in precipitation and temperature. Similarly, Getachew (2018) applied the SWAT hydrological model to simulate historical land cover changes and assess the future impact of climate change on surface runoff in the Anger sub-basin of Ethiopia. The author illustrates that the dynamics of land cover potentially affect the mean annual and seasonal surface runoff in the sub-basin. Furthermore, Kinati et al. (2019) concluded that the SWAT model can be used to investigate the effect of land use/land cover and climate change on river flow and soil loss in the Didessa River Basin, South West Blue Nile, Ethiopia. The study revealed that future climate changes, under RCP scenarios, enhanced river discharge and soil loss in the river basin. The SWAT model demonstrated its effectiveness in simulating hydrological processes with reasonable accuracy, making it a suitable choice for large and complex watersheds like the Mille River Watershed.

The Soil and Water Assessment Tool (SWAT) has been selected as the primary tool for simulating rainfall-runoff processes and assessing the impacts of land use and climate change in the Mille River Watershed, located in the Lower Awash River Basin, Ethiopia. This selection is based on several key factors, informed by both scientific literature and the specific requirements of the study area, which include the need for a physically-based model that can effectively handle complex hydrological processes at the watershed scale.

The first and most important justification for using SWAT is its proven suitability for watershed modeling, particularly in semi-arid regions similar to the Mille River Watershed. The model has demonstrated its ability to simulate hydrological processes across diverse catchment areas, providing valuable insights into the long-term effects of land use, climate change, and management practices on water quality and quantity (Arnold et al., 2012; Gassman et al., 2007). This is highly relevant for understanding how climate and land cover changes will influence water resources in the study area. Furthermore, SWAT's robust framework for simulating rainfall-runoff processes makes it an ideal choice for this research. It offers detailed representations of key hydrological components such as surface runoff, evapotranspiration, and sediment transport, all of which are critical for understanding the watershed's hydrological dynamics. SWAT's ability to process large datasets and generate outputs at multiple spatial and temporal scales is essential for studies of this scale and complexity (Neitsch et al., 2011). The ability to model and predict hydrological responses to various climate scenarios and land use changes is central to this study's objectives.

While alternative models such as SWAT+, WEAP, and HBV were considered, they were found to be less suitable for the specific needs of this research. SWAT was preferred due to its comprehensive representation of hydrological processes, its widespread application in similar studies, and its well-established calibration and validation procedures (Canton et al., 2015). Although SWAT+ is a newer version of SWAT, it was not considered due to the limited availability of reliable calibration datasets for the Mille River Watershed. Similarly, WEAP, while a valuable tool for water resources planning, does not provide the detailed hydrological modeling capabilities necessary for rainfall-runoff studies at the watershed scale. The HBV model, despite its ability to simulate hydrological processes, lacks the spatial resolution and land use flexibility offered by SWAT, making it less suitable for this study.

Finally, the potential for hybrid modeling approaches, such as combining SWAT with data-driven models like Artificial Neural Networks (ANN), was explored. However, the primary objective of this study is to employ a physically-based model to assess the impacts of land use and climate change on the hydrological cycle of the Mille River Watershed. Data-driven models like ANN are highly effective for streamflow forecasting but require large amounts of high-quality historical data, which were not sufficiently available for this study. Therefore, a hybrid approach was deemed unsuitable, and the focus remains on using SWAT as a standalone, physically-based modeling tool.

In conclusion, the SWAT model's established capabilities in watershed hydrology, its flexibility in modeling complex processes, and its ability to address the specific objectives of this study make it the optimal choice for simulating rainfall-runoff processes and evaluating the impacts of land use and climate change in the Mille River Watershed.

3. MATERIALS AND METHODS

3.1. Description of the Study Area

3.1.1. Location of the Study Area

The Awash Basin is situated between 7°53'42" to 12°07'20" North and 37°05'56" to 43°01'04" East. The basin is bordered by the Danakil, Abay, Omo-Gibe, Rift-Valley lakes, and Wabi-Shebele basins, as well as the Republic of Djibouti. The river originates from the central highlands of Ethiopia and flows northeast through the northern section of the Rift Valley, ultimately discharging into Lake Abbe near the Djibouti border, covering a distance of approximately 1200km. The Mille River is one the tributaries of the Awash River at the lower section of the lower Awash River basin and joined the Main Awash upstream of the Tendaho reservoir. Mille River originates and drains from the highlands of North Wollo to the low land of the Afar Region. Mille watershed is among the sub-watersheds of Lower Awash Sub Basin and is situated in the western part of the basin and located between 11^{o}32’31.73’’N and 39^{o}35’07.24’’E at the North high land of Wollo and 11^{o}26’38.83’’N and 40^{o}55’32.43’’E at the confluence of main Awash River (Figure 3.1). The watershed drainage area is about 4640.43 km^2 up to the outlet point. The elevation of the study area ranges from 3639m to 404m a.m.s.l.

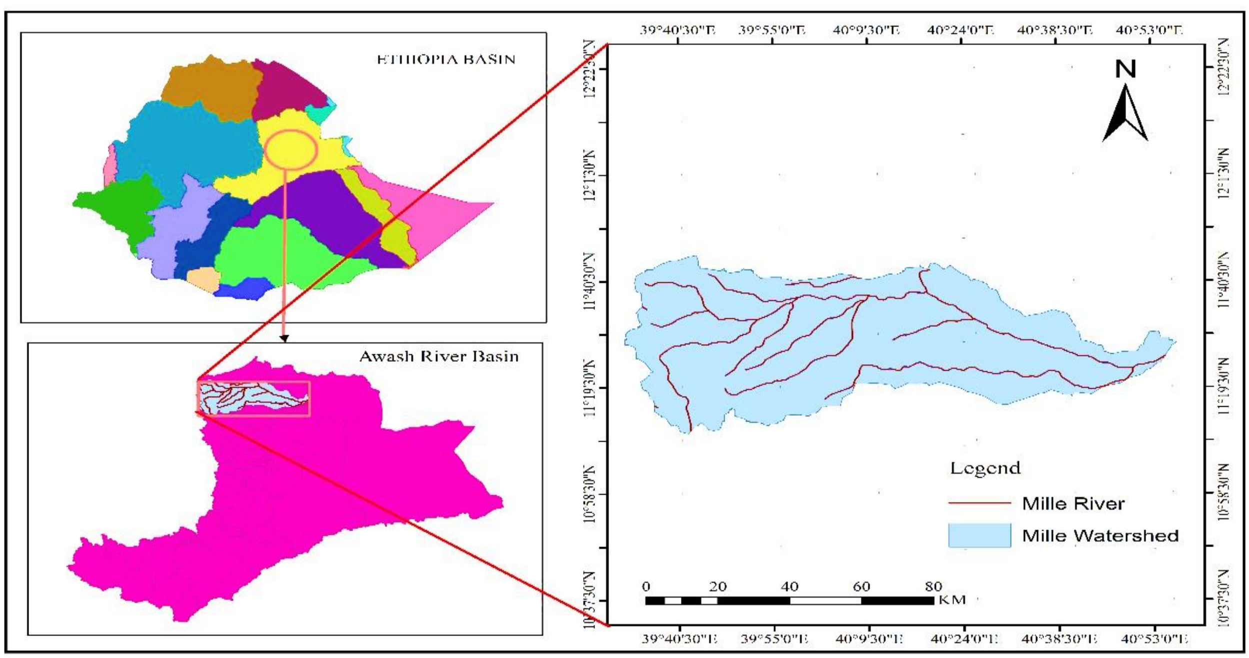

Figure 3.1: Location of the study area

3.1.2. Climate

The climate in the Awash River Basin exhibits a wide range of temperatures and precipitation, from cold high mountainous zones to semi-desert lowlands (Getahen Y. et al., 2020). The basin experiences three seasons: Kiremt, which is the main rainy season from June to September; Bega, the dry season from October to January; and Belg, the small rainy season from February to May. The precipitation follows a bi-modal pattern, with a short rainy season from March to April and the main rains occurring from July to September. The mean annual precipitation varies from 1600 mm in elevated areas to 160 mm in the lowlands. The average daily temperatures remain fairly constant throughout the year, with mean monthly minimum and maximum temperatures ranging from 7.93°C to 11.2°C and 23.91°C to 24.13°C, respectively. The annual temperature of the Awash River Basin ranges from 20.8°C in the upper part to 29°C in the lower part. The weather in the Lower Awash sub-basin is influenced by the position of the InterTropical Convergence Zone (ITCZ), with the rainy season starting in July when the ITCZ is at its northernmost position. The sub-basin has a hot arid climate according to the country's climatic classification. Precipitation and temperature distribution in the sub-basin are strongly linked to the altitude.

A. Rainfall

The Mille watershed in the Afar region of Ethiopia experiences a semi-arid climate with a bimodal rainfall pattern. The main rainy season, known as the Kiremt, occurs from June to September and brings the majority of the annual rainfall. During this period, the watershed receives an average of 300-500 mm of precipitation. The secondary rainy season called the Belg, takes place from February to May and contributes a smaller, but still significant, amount of rainfall to the region, typically 100-300 mm. The spatial distribution of rainfall across the watershed is variable, with the higher elevations in the west receiving more precipitation than the lower-lying eastern areas. The high variability and uncertainty of rainfall, both temporally and spatially, is a key characteristic of the climate in the Mille watershed.

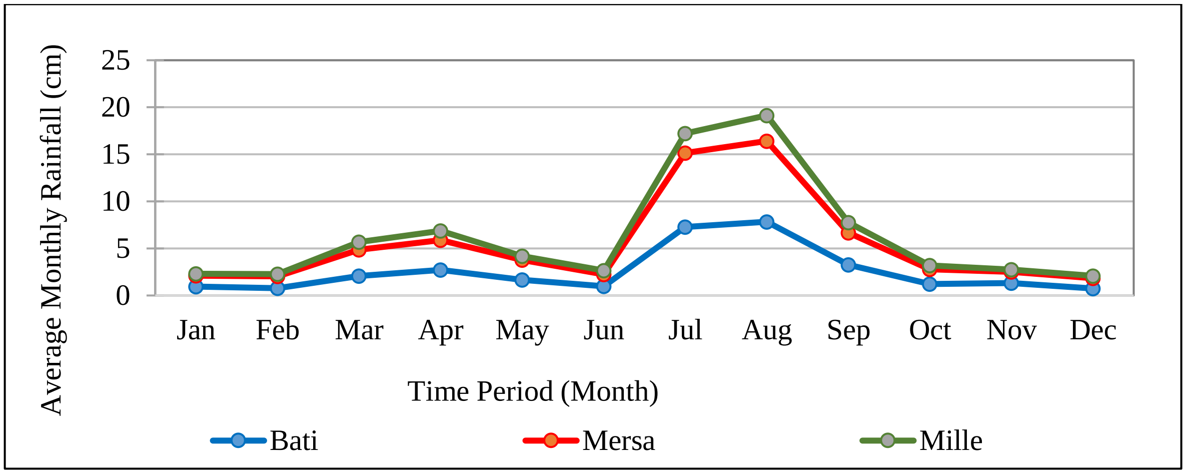

Figure 3.2: Mean Monthly Rainfall Distributions of the stations (1992-2023)

B. Temperature

The Mille watershed has a hot, semi-arid climate with high temperatures throughout the year. The mean annual temperature in the region is around 25-30°C. The warmest months are from June to August when average daily temperatures can reach 35-40°C. In contrast, the coolest months are from December to February, with average temperatures ranging from 20-25°C. The diurnal temperature variation is also substantial, with large differences between daytime and nighttime temperatures. This temperature regime, combined with the limited and erratic rainfall, creates a challenging environment for agricultural activities and natural resources management in the Mille watershed.

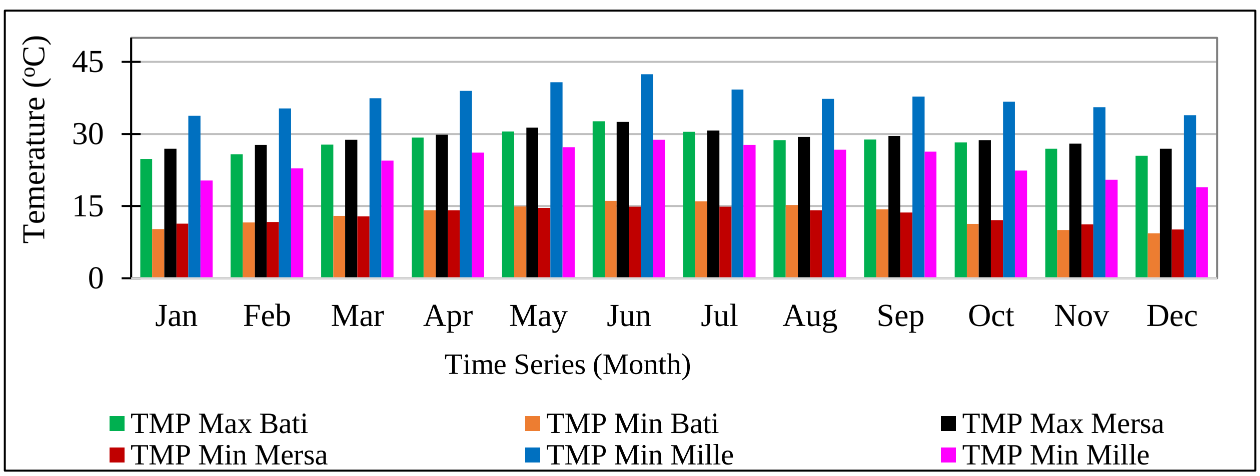

Figure 3.3: Average Monthly Max, Min, and Mean Temp in the period of (1992-2023)

There are few meteorological stations within and around the watershed with different lengths and types of records mainly concentrated in the upper part of the watershed. Some of the rainfall stations considered for the watershed area are Bati, Mille, and Mersa.

3.1.3. Hydrology

In terms of hydrology, the Mille River is one of the major contributors to the flow of the Awash River. The flow of it is highly seasonal, with peak flows typically occurring in August. The watershed experiences a highly seasonal hydrological regime, primarily influenced by rainfall patterns, land use changes, and topographic variations. The river's flow is characterized by peak discharges between July and September, coinciding with the Kiremt rainy season, while the dry season from October to February is marked by reduced or minimal flow. This seasonal variability is typical of semi-arid regions, where precipitation intensity and duration significantly affect runoff generation and water availability.

Hydrological monitoring in the watershed is supported by a streamflow gauging station installed by the Ministry of Water and Energy (MoWE) near the town of Mille. However, challenges such as data gaps and inconsistencies in historical records impact the accuracy of hydrological assessments. Strengthening monitoring systems and integrating reliable data into hydrological models are essential for improving water resource management. A deeper understanding of the watershed's hydrology will aid in developing strategies to enhance groundwater recharge, control flooding, and ensure sustainable water availability in the face of ongoing environmental changes.

3.1.4. Topography

Regarding topography, the Lower Awash River is characterized by an extensive floodplain that stretches from Logia town in the northwest to Asayita town and Buri Plain in the southeast, encompassing a wide meander belt as wide as 12-15 km around the Dubti area and Det-Bahari – Galifage areas. The floodplain consists mainly of silty clay/clayey silt, and the Awash River meanders across it, forming a meandering channel pattern.

3.2. Data Collection Methods and Procedures

3.2.1. Data Collection

3.2.1.1. Digital Elevation Model (DEM) Data

A Digital Elevation Model (DEM) with a resolution of 12.5m x 12.5m was utilized in this study to derive essential hydrological parameters, including flow direction, flow accumulation, stream network generation, and the delineation of the watershed and sub-basins. Additionally, key topographic characteristics of the watershed, such as terrain slope, channel slope, and reach length, were extracted from the DEM. The DEM data used in this study, specifically the ALOS PALSAR RTC (Radiometrically Terrain Corrected) DEM, was obtained from the Alaska Satellite Facility (ASF) Vertex Data Portal (https://search.asf.alaska.edu/). Accessing this data required creating a free account on the portal. The area of interest (AOI) was defined using the search interface, and the DEM was downloaded in GeoTIFF format, ensuring compatibility with GIS software for further analysis.

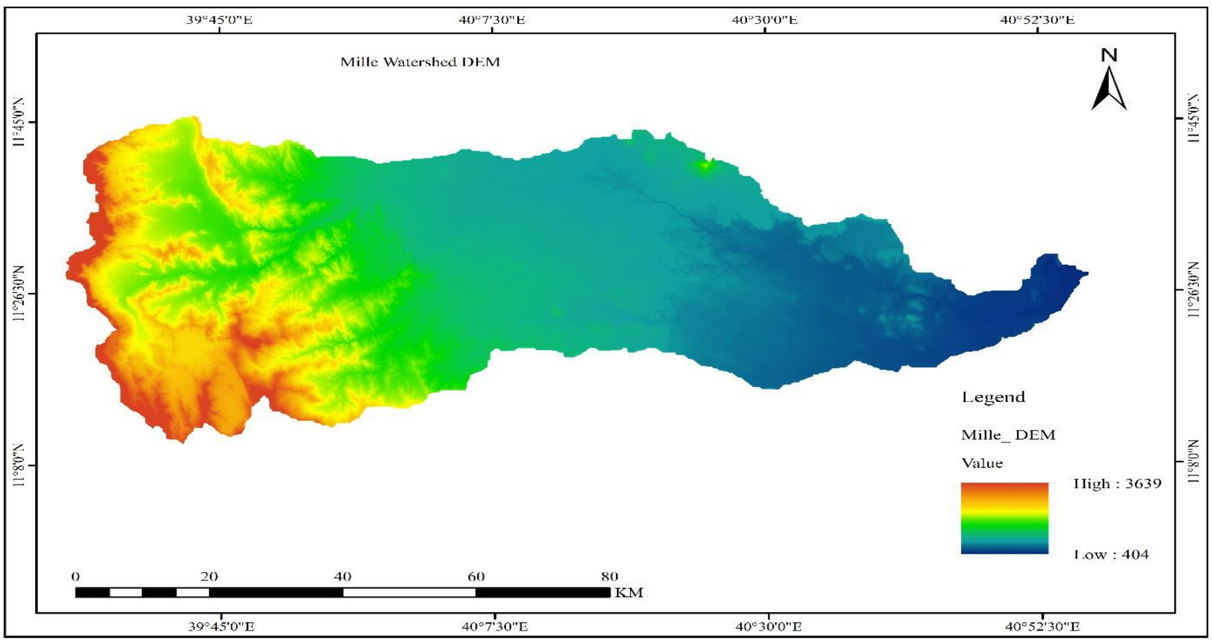

Figure 3.4: DEM of Mille Watershed

3.2.1.2. Land use land cover data

The Land Use/Land Cover (LULC) data was obtained from the National Aeronautics and Space Administration (NASA) via the website https://earthexplorer.usgs.gov/. This dataset is essential for the SWAT model, particularly in evaluating its impact on streamflow within a watershed and characterizing the Hydrological Response Units (HRUs) of the watershed. The historical LULC data was sourced from Landsat imagery, which was processed using supervised classification in the Earth Resources Data Analysis System (ERDAS Imagine). The land cover classification for the years 2000, 2010, and 2020, along with projections for 2030 and 2050, was based on these classified satellite images, using the IDRISI Selva v.17 model within the study area.

The SWAT model assigns specific four-letter codes to each land use classification, enabling seamless integration of the study area's land cover map with the SWAT land use database. Consequently, adjustments were made during the creation of the lookup table to ensure compatibility between the land use categories and the model's input requirements.

The primary land use and land cover types within the watershed include agricultural land, grasslands, forests, scrub/bushlands, woodlands, barren land, water bodies, and settlements. According to the 2020 LULC map (Table 4.4 and Figure 4.1), the total area of the watershed is 5,823.33 km². Of this, approximately 37.46% is dominated by agricultural land, while 24.33% is covered by barren land.

Table 3.1 Land Use/Land Cover of the Study Area

Land use/ land cover	Land use according to SWAT Database	SWAT Code
Agriculture	Agricultural Land-Generic	AGRL
Forest	Forest-Mixed	FRST
Settlement	Residential	URBN
Grassland	Range-Grasses	RNGE
Shrub/bush	Range-Brush	RNGB
Water Body	Water Body	WATR
Barrenland	Barren	BARR
Woodland	Forest-Deciduous	FRSD

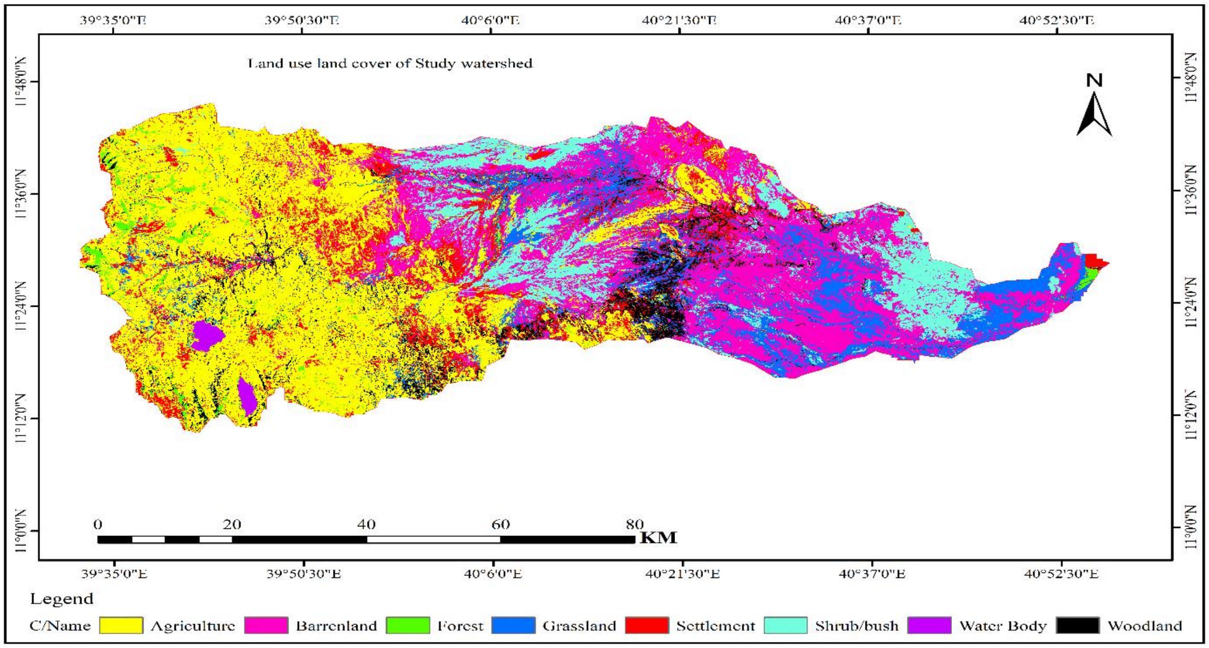

Figure 3.5: Land use land cover of the Study watershed

3.2.1.3. Soil Map Data

Soil characteristics play a vital role in providing input data for the SWAT2012 model used in watershed analysis. The soil data for the study area were sourced from the Food and Agricultural Organization – Harmonized World Soil Database (FAO-HWSD) and validated with the HWSD Viewer soil map. Within the watershed, five distinct soil classifications were identified. To integrate this soil information into the SWAT model, a customized database was created, incorporating both textural and chemical properties of the soils across different layers. This database was then uploaded to the SWAT user soil database using the data management append tool in ArcSWAT10.4.1.

Table 3.2: Major Soil Types in the Mille Watershed

No	Soil Types	Area in (ha)	Area in (KM^2)	Area in (%)
1	Eutric Cambisols	240562.7	2405.63	41.41
2	Lithosols	40409.7	404.10	6.96
3	Calcic Xerosols	218093.9	2180.94	37.55
4	Eutric Gleysols	81755.9	817.56	14.07
5	Calcic Xerosols	49.4	0.49	0.01

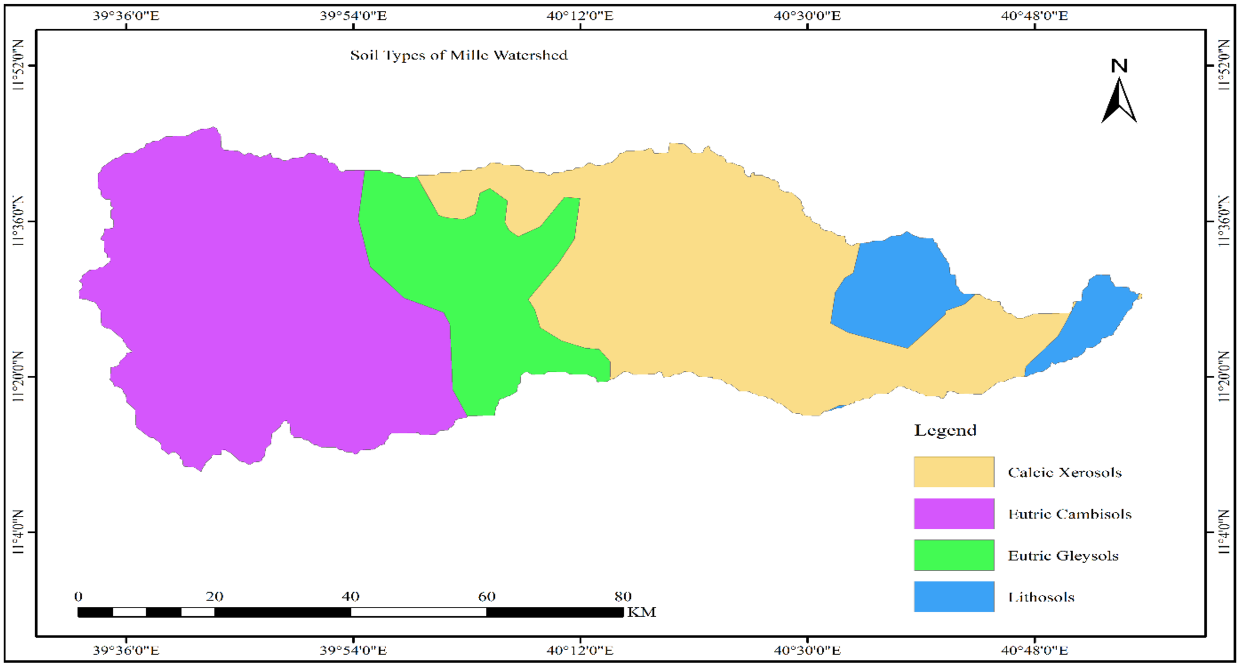

Figure 3.6: Soil map of the Study watershed

3.2.1.4. Slope Class Map

The slope gradients in the sub-basin range from flat to very steep. Based on these gradients, the slopes were categorized into five classes: 0–5%, 5–12%, 12–20%, 20–30%, and 30–67%. Using DEM data in the ArcGIS environment, the slope gradients were calculated and subsequently reclassified into four categories as follows: gentle slopes (0–5%), moderate slopes (5–15%), steep slopes (15–30%), and very steep slopes (>30%) (FAO, 1990). Table 3.3 presents the percentage distribution of each slope class across the Mille watershed as shown in Appendix Figure 6.

Table 3.3: Slope Classes of the Mille Watershed

No	Slope Class	Area Coverage (%)
1	0 – 5	10.32
2	5 – 12	37.87
3	12 – 20	16.26
4	20 – 30	19.17
5	30 – 9999	16.39

3.2.1.5. Hydro-Meteorological Data

Meteorological data, including precipitation, temperature, wind speed, solar radiation, and relative humidity, were collected from the Ethiopian National Meteorological Institute (NMI). Weather data required for SWAT input comprises daily precipitation, maximum and minimum temperatures, relative humidity, wind speed, and solar radiation. In this study, three stations within and around the Mille watershed Mille, Bati, and Mersa stations were considered, as other stations lacked recorded data. The climate data used in this research spans 32 years, from January 1992 to December 2023. While rainfall and temperature data were available at all stations, sunshine hours, wind speed, and relative humidity data were unavailable for Mersa station. Mille station served as the weather generator station to produce weather variables for missing records, which were marked with a no-data code value (-99) in the SWAT database. The climate data for the study period was formatted into a text file and imported into the SWAT model database.

Streamflow data from the Mille watershed is essential for calibrating and validating the model. Daily discharge data (1995–2018) for the Mille River near the Mille Village gauging station was obtained from the Ministry of Water and Energy (MoWE). Missing flow data were filled using the Stata software. The missing flow data were filled using Stata/SE 17.0 software. Linear interpolation was employed to estimate the missing values, a widely used technique for handling missing time-series data. This approach involves fitting a straight line between two known data points to interpolate the missing values. The observed streamflow data were imported into Stata, gaps in the dataset were identified, and the ipolate command was applied to fill in the missing values. This ensured the completeness and consistency of the data for subsequent analysis.

3.2.1.6. Checking Hydro-Meteorological Data Quality

A. Filling Missing Precipitation Data

Missing hydro-meteorological data is a common challenge in performing hydrological analysis and modeling using long-term data, making the process of filling missing data critical. Failures of rain gauges or the absence of observers at a station often cause short breaks in rainfall records. Various methods are employed to address this issue under different conditions. Two widely used methods for filling in missing climate data are the Arithmetic Mean Method and the Normal Ratio Method. The Arithmetic Mean Method is applied when the normal annual precipitation at a station differs by less than 10% from the gauge/station being reconstructed. In contrast, the Normal Ratio Method is used when the difference exceeds 10%. In this study, missing data were filled using both the Arithmetic Mean Method and the Normal Ratio Method. Ensuring data quality in this research study involved selecting a method based on the computation of missing percentages for the two approaches. The specific formula for the Arithmetic Mean Method is provided as Equation 1:

$$Px = \frac{\sum_{i=1}^{n} Pi}{n} \quad (1)$$

Where: P_X is the missing precipitation value for station i (i=1, 2, 3...n), and P_1, P_2… P_n are Precipitation values at the adjacent stations for the same period and N is the number of nearby. Stations.

The formula for the Normal Ratio Method is given as Equation 2:

$$Px = \frac{1}{n} \sum_{i=1}^{n} \frac{P_i}{N_i} N_x. \quad (2)$$

Where: P_X is the missing precipitation value for station x for a certain period, P_i is the precipitation values at adjacent stations for the same period, N_x is the long-term, annual average precipitation values at station x, N_i is the long-term precipitation for neighboring stations and n is the number of adjacent stations.

Table 3.4: The rainfall stations located in and around the study area

No.	Stations	Elev.(m)	Lat.(°)	Lon.(°)	Period	% missing	Mean
1	Bati	1637	11.20	40.02	1992-2023	7%	930.65
2	Mersa	1578	11.66	39.67	1992-2023	14.7%	1043.81
3	Mille	487	11.43	40.77	1992-2023	16.2%	301.50

B. Checking the Consistency of Data

To check for data consistency, the double-mass curve technique was employed, as recommended by Subramanya (2013). A double mass curve is a graphical method for identifying and adjusting inconsistency in a station record by comparing its time trend with those of adjacent stations. The reasons for the selection of the double-mass curve technique for checking the consistency of rainfall data in this study were based on its applicability to identifying inconsistencies, its potential for adjustments to ensure data consistency, and its relevance to the research focus. Limitations of the Double-Mass Curve Technique include Assumption of consistency, Sensitivity to outliers, Reliance on cumulative data, and Limited to historical data, etc. To mitigate these limitations, it is advisable to complement the double-mass curve technique with other quality control measures, expert knowledge, and additional data sources to ensure a comprehensive assessment of data consistency. To verify data consistency, the double-mass curve technique was employed, as recommended by Subramanya (2013). This graphical method identifies and corrects inconsistencies in station records by comparing their time trends with those of adjacent stations. The double-mass curve technique was selected for this study due to its effectiveness in detecting inconsistencies, its ability to make adjustments to ensure consistency, and its relevance to the research. However, the technique has certain limitations, including assumptions of consistency, sensitivity to outliers, reliance on cumulative data, and constraints to historical data. To address these limitations, additional quality control measures, expert knowledge, and supplementary data sources were recommended to ensure comprehensive data consistency assessments as shown in Appendix Figure 2.

When inconsistencies in rainfall data were identified, corrections were made using the following equation (Equation 3):

$$P_{cx} = \frac{P_x * M_c}{M_a} \tag{3}$$

Where: P_{cx} – is corrected precipitation at any period, P_x – is the original recorded precipitation at the period, $M_C -$ is the corrected slope of the double mass curve and $M_a -$ is original of the slope of the double mass curve.

C. Climate Data Homogeneity Test

The analysis confirmed that the total annual rainfall data from all the selected stations in and around the sub-basin was consistent and homogeneous (as shown in Appendix Figure 3). The annual streamflow data (m³/year) from the Mille River near the Mille gauging station was also checked for homogeneity over the 1995–2018 period, as illustrated in as shown in Appendix Figure 4.

3.2.2. Land Use Land Cover Change Detection

Land use and land cover (LULC) data play a crucial role as foundational input datasets in SWAT modeling to analyze watershed runoff impacts and define Hydrological Response Units (HRUs) within watersheds. Historical LULC maps were derived from Landsat satellite imagery through supervised classification conducted using the Earth Resources Data Analysis System (ERDAS) Imagine v.15. The study utilized classified LULC maps from 2000, 2010, and 2020, while future projections for 2030 and 2050 were generated using IDRISI Selva v.17, based on historical satellite images. The SWAT model requires predefined four-letter codes for each LULC category, which were assigned to link the study area's LULC map with SWAT's database. Accordingly, the land use categories were adjusted during the preparation of the lookup table to meet the input specifications of the SWAT model.

3.2.2.1. Image Pre-Processing and Data Acquisition

Landsat images were used to generate the land use maps. Specifically, Landsat 5 TM, Landsat 7 ETM+, and Landsat 9 OLI/TIRS were selected to represent the years 2000, 2010, and 2020, respectively. These datasets were obtained in compressed formats from the United States Geological Survey (USGS) website (https://www.usgs.gov) and then extracted into TIFF files. Layer stacking was performed to combine the different spectral bands of the downloaded imagery using ERDAS Imagine. Additionally, mosaic operations, which combine multiple images into a single dataset, were carried out.

Remote sensing imagery is essential for studying the effects of LULC and climate change on rainfall-runoff dynamics within watersheds. It requires computational processing to create accurate LULC maps. However, satellite data may contain errors that must be addressed before use. A variety of pre-processing techniques were applied, including image enhancement, as well as geometric and radiometric corrections, to improve the quality of the LULC maps.

The Landsat datasets from 2000, 2010, and 2020 were utilized, as detailed in Table 3.5. Each image was georeferenced to the WGS_84 datum and Universal Transverse Mercator (UTM) Zone 37N. To minimize seasonal variability in vegetation patterns, efforts were made to acquire images from the same season each year. Both true-color and false-color compositions were employed to enhance surface feature differentiation and ensure comprehensive coverage of the Mille sub-basin.

Table 3.5: Landsat Images Used for LULC Analysis and Their Characteristics

Satellite	Sensor	Path/Row	Date of Acquisition	Resolution	Season	Source
Landsat 5	TM	167/053	1/5/2000	30x30m	Dry	USGS
	TM	167/053	1/12/2000	30x30m	Dry	USGS
Landsat 7	ETM+	167/053	1/15/2010	30x30m	Dry	USGS
	ETM+	167/053	3/13/2010	30x30m	Dry	USGS
Landsat 9	OLI/TIRS	167/053	1/15/2023	30x30m	Dry	USGS
	OLI/TIRS	167/053	2/23/2023	30x30m	Dry	USGS

3.2.2.2. Image Classification

Image classification involves categorizing image pixels into predefined LULC classes by matching their spectral signatures with those of various LULC types. The objective is to classify all image pixels into specific LULC categories to derive meaningful thematic information. Different methods are available for image classification, with the choice depending on the intended purpose and the analyst's proficiency with the algorithms. These methods are generally divided into supervised, unsupervised, and hybrid approaches. In this study, supervised classification was selected to ensure high accuracy, requiring a clear understanding of the land cover types under examination. Supervised classification uses user expertise to identify clusters of pixels corresponding to particular LULC categories. ERDAS Imagine software was employed for image classification and enhancement, facilitating the creation of LULC maps required for SWAT modeling. Landsat images for 2000, 2010, and 2020 were processed in ERDAS Imagine for image enhancement, classification, and reclassification using the Maximum Likelihood Algorithm. This process involved defining areas of interest (AOI), referred to as training samples. Training sites were identified using the Landsat images and validated using Google Earth. The samples for each LULC class were consolidated by referencing historical images, topographic maps, and the original mosaic image. In this study, the Maximum Likelihood classifier was used to perform supervised classification. Signature extraction, training site identification, and classification were conducted within this framework. Subsequently, ArcGIS software was used to generate LULC maps for 2000, 2010, and 2020. Eight distinct LULC categories were identified: agriculture, grassland/range, forest, scrub/bush, water bodies, settlement, barren land, and woodlands. This classification aligns with studies by Desalegn et al. (2014) and Adane & Getachew (2017) in the Bale eco-region.

Table 3.6: Description of LULC types in Mille River Watershed

Class Name	Description
Agriculture	Denotes land areas designated for cultivation of both annual and perennial crops.
Forest	Pertains to land areas characterized by a dense population of trees or closed canopies, encompassing evergreen forests and plantation forests.
Settlement	Designates areas featuring permanent urban settlements, densely populated rural settlements, and various facilities.
Grassland	Comprises either communal or privately owned grazing lands utilized for livestock grazing. These lands are predominantly covered by small grasses, grass-like plants, and herbaceous species, encompassing areas used for grazing as well as patches of grass with some bare land or other small plant species.
Shrub/bush	Includes areas covered by Asta scrubland, Erica bushes, alpine vegetation, and small white-leaved plants found atop the Sanette Plateau, serving as habitats for the Ethiopian Wolf.
Water Body	Refers to areas covered with permanent open water, mainly including lakes, reservoirs, streams, canals, and other shallow water bodies.
Barren land	Constitute locales with limited capability to sustain life where less than one-third of the area has vegetation or other cover. It describes the terrain of thin soil, sand, or rocks where the coverage of available vegetation is much less than range land.
Woodland	refers to land that is not classified as forest but spans more than 0.5 hectares, including deciduous and mixed forest areas.

3.2.2.3. Accuracy Assessment

Accuracy assessment entails comparing a generated classification to the actual features present on a mapped image of the same area to evaluate the classification's reliability. This process involves comparing a map derived from remote sensing analysis with a reference map created using various data sources, such as Google Earth and original mosaic images. The classification accuracy is determined through sampling from the image, refining images, and calculating the probability that a given pixel corresponds to a specific class. For validation, a total of 195, 224, and 300 test samples were randomly selected from the original mosaic images for the years 2000, 2010, and 2020, respectively. These were validated against images from 2000 and 2010, along with Google Earth images for 2020, using ERDAS IMAGINE V.15. The accuracy evaluation process employs an error matrix (also known as a confusion matrix) to establish the relationship between the classified data and reference data. Typically, the matrix columns represent reference data, while the rows denote classifications from the image. Errors of omission occur when pixels from the reference map are misclassified relative to their true value, while errors of commission arise when pixels are inaccurately assigned to a specific class. Metrics such as overall accuracy, user accuracy, and producer's accuracy are computed to measure classification performance. Overall accuracy assesses the general reliability of the classification, calculated as the proportion of correctly classified pixels to the total pixel count in the error matrix. Many of the metrics used derive from this matrix, where the user's accuracy reflects the likelihood that a pixel corresponds to its classification in the field, and the producer's accuracy represents the proportion of a class correctly identified on the map (Sahalu, 2014).

3.2.3. LULC Change Detection Analysis

Land use and land cover (LULC) change detection involves analyzing classified satellite images from different periods to identify the nature, extent, and spatial distribution of changes. This study investigated LULC changes over five specific timeframes: 2000, 2010, and 2020 for historical analysis, and 2030 and 2050 for future projections. The selection of these periods was influenced by factors such as resettlement initiatives and the availability of high-quality satellite imagery for the study area. The post-classification cross-tabulation method in ArcGIS was employed to assess LULC changes by comparing classified images across the selected periods. Statistics for LULC changes were computed by comparing the area values of one dataset with the corresponding values of the subsequent dataset for each time frame using Equation 4. The annual rate of change for each LULC category was calculated with Equation 5. By examining the statistics related to land use land cover change, insights were gained into the percentage variations, trends, and annual rates of change between 2000 and 2020. A critical step in this process was the creation of a detailed table displaying the area in hectares and the percentage change for each of the past periods (2000, 2010, and 2020) and future periods (2030 and 2050) in comparison to each land use land cover type.

$$\text{Percentage Change} = \frac{\text{Final Year Area} - \text{Initial Year Area}}{\text{Initial Year Area}} \tag{4}$$

$$\text{Annual Rate of Change} = \frac{\text{Final Year Area} - \text{Initial Year Area}}{\text{Number of Year Between two image}} \tag{5}$$

3.2.4. Land Use Land Cover Change Prediction and Model Validation

3.2.4.1. Land Use Land Cover Change Prediction

Future predictions of Land Use Land Cover (LULC) changes for 2030 and 2050 were performed using the CA-Markov model within IDRISI Selva, a geospatial software designed for Earth system analysis (version 17.0). The Cellular Automata (CA) and Markov Chain models are widely recognized for their efficacy in simulating land use changes (Mishra and Rai, 2016; Parsa et al., 2016). These models are particularly useful in predicting both trends and spatial patterns of LULC classes based on input data, including observed LULC images, transition probability matrices, and suitability maps (Wang et al., 2012; Li et al., 2020). Gambo et al. (2018) noted that CA-Markov provides a distinct advantage over other dynamic models by enabling spatial evaluation and accurate predictions of future land use. For the accuracy of LULC classification in remote sensing data, it is essential for classification accuracy to exceed 85%, as highlighted by Mishra and Rai (2016).

The process began by gathering and preparing the historical LULC maps for the baseline years of 2000, 2010, and 2020. The 2020 classified map was used as the foundational LULC image for the future predictions of 2030 and 2050. The 2000 and 2010 maps were used to construct the transition probability matrix for the prediction. A uniform error proportion of 0.15 was applied for these transitions. It was crucial that all maps were carefully checked for proper georeferencing to ensure they were spatially aligned. Additionally, all maps were standardized to the same projection and spatial resolution, and any discrepancies were addressed by resampling the maps to a uniform standard. After preprocessing, the maps were imported into IDRISI Selva as raster layers representing the land cover classifications for each year. To create the transition matrices required for the CA-Markov model, the LULC maps from 2000 to 2010 and 2010 to 2020 were used to quantify the changes in land cover over time. The Markov Chain Analysis tool within IDRISI Selva was employed to generate the transition matrices, which represent the probabilities of land cover classes transitioning from one to another between these periods. These matrices are essential for simulating future land use/land cover changes based on historical trends. After preparing the transition matrices, the next step was to configure the Cellular Automata (CA) model. In IDRISI, spatial rules governing these interactions were defined, and the transition probabilities for each class were set. A neighborhood size of 3x3 or 5x5 was specified to determine which neighboring cells influence the state of each cell during the simulation. The transition probability matrices, CA rules, and neighborhood size were all configured before running the simulation. Once the parameters were defined, the CA-Markov simulation was executed to predict future LULC maps for 2030 and 2050. The model used historical trends captured in the transition matrices to simulate land cover changes over the desired time periods. The output was a series of predicted LULC maps reflecting potential future changes in land cover, assuming that current trends would continue. These maps were generated for the years 2030 and 2050 based on the 2020 baseline.

To validate the predicted Land Use and Land Cover (LULC) maps, a comparison was made between the simulated LULC maps for 2030 and 2050 and the observed LULC map for 2020. The goal of this comparison was to evaluate how closely the predicted changes matched the actual land cover data. To quantitatively assess the agreement between the simulated and observed maps, the Kappa index was calculated. The Kappa index is a statistical measure that evaluates the accuracy of the predicted land cover classes by quantifying the level of agreement between the simulated and observed LULC maps. Higher Kappa index values indicate stronger agreement, which in turn validates the performance of the CA-Markov model in predicting future LULC changes. This process ensures that the simulated LULC maps accurately reflect the observed trends and can be relied upon for further analysis and decision-making. Once the validation was completed, the predicted LULC maps for 2030 and 2050 were analyzed. These maps provide insights into potential future land cover scenarios, which are crucial for land management and environmental planning in the study area. The predicted maps were exported into suitable formats for further analysis and presentation, supporting future land use decision-making processes. This procedure provided accurate predictions of LULC changes for 2030 and 2050, offering a clear understanding of potential future land use changes in the study area.

3.2.4.2. Validating LULC Change Prediction Model

The validation of the LULC prediction model is crucial in ensuring its reliability and accuracy. The CA-Markov chain serves as a stochastic procedures model that articulates the likelihood of transitioning from one land use land cover class to another using a transition probability matrix. In the current study, IDRISI Selva v.17 was utilized to forecast the future LULC within the study area using the CA-Markov model, with a simulation based on the 2000 and 2010 maps to generate a projected 2020 map. Subsequently, it is imperative to validate this simulated 2020 map against the actual 2020 LULC map through the Kappa Agreement of Index (KIA) approach, as highlighted by Mishra and Rai (2016) and Parsa et al. (2016). It is widely acknowledged that any model prediction necessitates thorough calibration and validation procedures to ensure its accuracy and reliability. Thus, the simulated LULC map of 2020 is meticulously compared with the observed 2020 LULC map utilizing the Kappa index.

$$\textbf{K}\text{appa} = \frac{\text{Po}-\text{Pc}}{1-\text{Pc}} \tag{6}$$

In the aforementioned equation, Po represents the proportion denoting accurately simulated cells; Pc denotes the anticipated proportion correction resulting from chance alignment between the observed and simulated map. Should Kappa be less than or equal to 0.5, it indicates a scarce level of agreement, while values between 0.5 and 0.75 suggest a moderate degree of concordance. Furthermore, Kappa values ranging from 0.75 to 1 signify a high degree of agreement, with Kappa equaling 1 signifying a state of perfect concurrence as delineated by Pontius and Malanson in 2005.

3.2.5. GCMs Used In This Study

This study employs the Canadian Earth System Model, Version 5 (CanESM5), to project future climate changes and assess their impacts on the Mille River Watershed. Developed by the

Canadian Centre for Climate Modelling and Analysis (CCCma), CanESM5 is part of the CMIP6 framework and represents a significant advancement in global climate modeling. It integrates atmospheric, oceanic, sea-ice, and land surface components, along with explicit carbon cycle schemes, enabling robust centennial-scale climate simulations. The inclusion of CanESM5 in this research highlights its ability to provide detailed projections across spatial and temporal scales, critical for understanding regional climate dynamics and their impacts on water resources (Sigmond et al., 2023).

CanESM5 was selected for this study based on several factors. Widely utilized in climate research, it provides detailed projections for various greenhouse gas emission scenarios and is freely accessible via the Canadian Climate Data and Scenarios platform. Validated for Africa, including Ethiopia, CanESM5 demonstrates robust performance in simulating regional climate patterns such as precipitation variability and extreme weather events. These capabilities make it particularly suitable for hydrological studies in the Mille River Watershed (Sigmond et al., 2023).

The model incorporates advanced features to simulate critical climatic phenomena, such as rainfall variability and its effects on hydrological processes. As part of CMIP6, CanESM5 integrates the latest advancements in model physics, parameterizations, and feedback mechanisms, ensuring high-resolution and accurate climate projections under SSP2-4.5 (medium emissions) and SSP5-8.5 (high emissions).

This study utilizes historical climate data for the baseline period (1979–2014) obtained from CMIP6 archives and observed data (1992–2023) sourced from the Ethiopian Meteorological Institute. Future climate projections spanning 2015–2100 under SSP2-4.5 and SSP5-8.5 scenarios were downloaded from the Canadian Climate Data and Scenarios platform. These datasets include daily time series for precipitation, maximum temperature, and minimum temperature, extracted for grid boxes corresponding to the study area's latitude and longitude. Predictor variables span multiple atmospheric pressure levels (500, 850, and 1000 hPa) to ensure a detailed representation of climate dynamics. Historical reanalysis data (NCEP-DOE Reanalysis 2, 1979–2014) were used for baseline comparison, enhancing the robustness of the dataset. To refine the coarse-resolution GCM outputs into high-resolution data suitable for watershed-level analysis, this study employs a regression-based Statistical Downscaling Model

(SDSM). SDSM is a widely used tool for developing localized climate change scenarios. It establishes empirical relationships between large-scale atmospheric predictors (e.g., atmospheric circulation variables) and local predictands (e.g., observed station-based precipitation and temperature) using linear transfer functions. The downscaled outputs were validated against baseline observations and local climatic records to assess the model's ability to reproduce historical climate variability and trends. Predictor variables from CanESM5 were selected to cover the historical period (1979–2014) and extend to future projections (2015–2100) under SSP2-4.5 and SSP5-8.5 scenarios. These variables maintain consistent horizontal resolutions on a 64x128 latitude-longitude Gaussian grid with spectral truncation at T42. The ensemble includes 26 predictor variables (as shown on Appendix Table 1), encompassing raw and derived atmospheric data across three pressure levels (500, 850, and 1000 hPa). These variables were interpolated to align with the CanESM5 grid. Historical reanalysis data from the NCEP-DOE Reanalysis 2 dataset were also used, obtained on their native grid (0.25° x 0.25°) without modifications or interpolation, to calibrate and validate the SDSM model.

Table 3.7: All Predictor Ensemble Datasets Used for the Study.

Model	ECS (0K)	Pressure Levels (hPa)	SSP	Variant	Leap Years
CanESM5	5.6	500, 850, 1000	SSP2-4.5, SSP5-8.5	r1i1p1f1	No
NCEP-DOE Reanalysis 2	n/a	500, 850, 1000	n/a	-	Yes

The CanESM5 datasets operate on a 365-day calendar, excluding leap years, while the reanalysis data from NCEP-DOE provide full-year datasets for comprehensive comparisons. The datasets also differentiate between standardized data files ("sd") and original data files ("og") using a type category in their naming conventions. CanESM5 data, available under the 'gn' grid label, were paired with reanalysis predictors (denoted as 'gr' grid) for consistency.

By integrating CanESM5 datasets with statistical downscaling techniques, this study develops high-resolution localized climate scenarios for the Mille River Watershed. The inclusion of SSP2-4.5 and SSP5-8.5 scenarios provides critical insights into potential climate-induced changes in precipitation, temperature patterns, runoff generation, and water resource availability. These scenarios form the foundation for assessing future hydrological impacts and support sustainable water resource planning and climate adaptation strategies in the Mille River Watershed.

3.2.5.1. Statistical Downscaling Model (SDSM)

The Statistical Downscaling Model (SDSM), developed by Robert L. Wilby and Christian W. Dawson (Wilby & Dawson, 2007), is a recognized tool designed for statistical downscaling. It facilitates the efficient and cost-effective generation of site-specific projections of daily surface climate variables for both present and future climatic conditions.

SDSM integrates two statistical downscaling techniques: linear regression and a stochastic weather generator. Predictors are statistically linked to local predictands using linear equations that minimize the root mean square error, while the stochastic component adjusts daily data variance to better match observed time series (Wilby & Dawson, 2007).

Through multiple linear regression techniques, SDSM enables spatial downscaling by relating daily predictor variables, which describe large-scale atmospheric states, to predictands that represent localized conditions valuable for hydrological modeling applications.

The SDSM process is structured into seven key steps (Wilby & Dawson, 2007):

1. Quality Control and Data Transformation: Meteorological datasets often contain errors or missing values. Quality control helps identify and address data gaps, outliers, and errors to ensure reliability before calibration.
2. Screening of Predictor Variables: Empirical links between large-scale predictors (e.g., mean sea level pressure) and local predictands (e.g., precipitation) are analyzed to choose appropriate predictors for downscaling.
3. Model Calibration: Predictands and predictors are used to configure the parameters of a multiple regression equation.
4. Weather Generator: Synthetic daily weather series are created using observed or reanalysis data to validate models and generate artificial series for the current climate.
5. Data Analysis: Tools for summary statistics and frequency analyses support the evaluation of downscaled and observed climate scenarios.
6. Graphical Analysis: SDSM version 4.2 offers graphical options like frequency analysis, result comparison, and time series evaluation.

7. Scenario Generation: Synthetic daily weather series ensembles are produced using atmospheric variables from climate models.

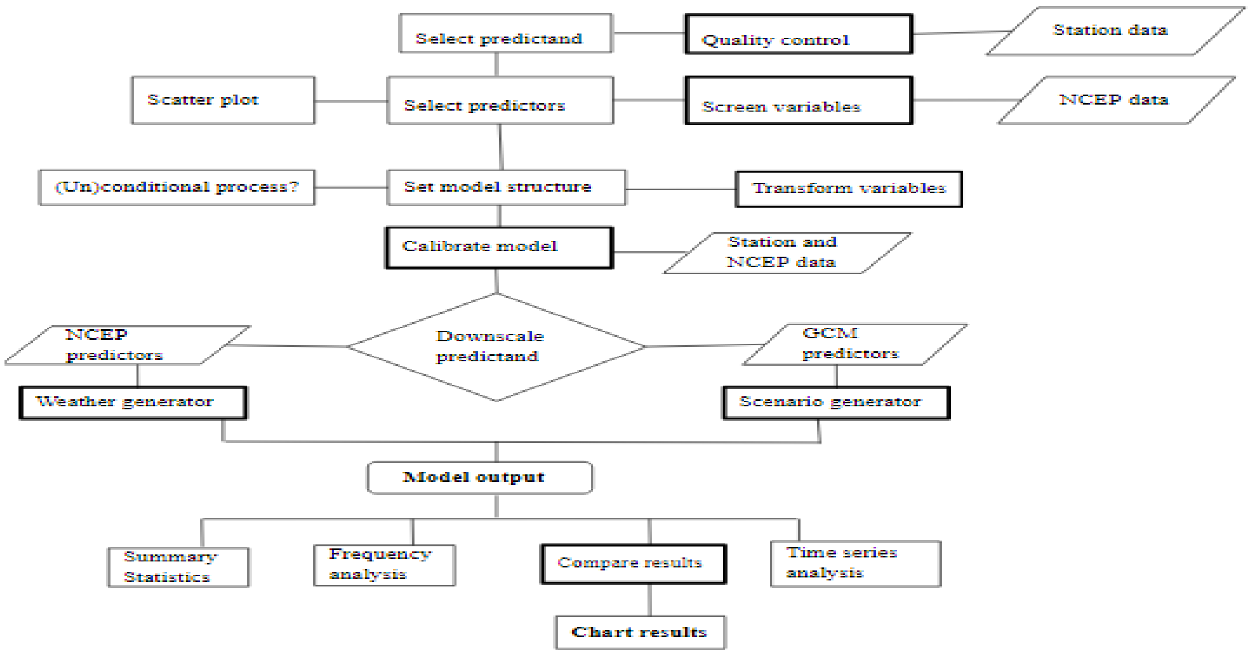

Figure 3.7: SDSM Version 4.2 Climate Scenario Generation (Wilby & Dawson, 2007)

3.2.5.2. Performance Evaluation of GCM Outputs

Evaluating the performance of General Circulation Models (GCMs) is essential for accurately simulating climate variables that influence hydrological processes in the Mille River watershed. In this study, the performance of the Canadian Earth System Model version 5 (CanESM5) was assessed to ensure the reliability of climate projections for hydrological modeling. Numerous studies have evaluated the performance of CanESM5 and other CMIP6 models, providing valuable insights for this research. For instance, Bhasin et al. (2023) evaluated the performance of CMIP6 models, including CanESM5, using various statistical indicators such as Root Mean Square Error (RMSE), Spatial Correlation (SC), Percentage Bias (Pbias), Normalized Root Mean Square Error (NRMSE), and Nash-Sutcliffe Efficiency (NSE). These metrics were used to rank the models based on their ability to simulate climate variables affecting rainfall-runoff processes. Nguyen et al. (2023) explored the combined effects of climate and land-use changes on river runoff in a specific basin using the SWAT model. Their findings emphasized the significant impact of climate change on river runoff, highlighting the importance of incorporating both climate and land-use change scenarios in hydrological models. Similarly, Gao et al. (2020) assessed the potential impact of climate and land use on hydrologic processes in an agriculturally dominated watershed, also using the SWAT model. Their research underscored the importance of considering both climate and land-use factors to predict future hydrological conditions accurately.

In a comparative study, Smith et al. (2020) assessed the performance of CMIP5 and CMIP6 models, including CanESM5, and found that CanESM5 provided better results than its predecessor, CanESM2. This improvement suggests that CanESM5 may offer more accurate climate projections for the Mille River watershed, thus enhancing the reliability of hydrological modeling. Zhang et al. (2019) provided a comprehensive description of CanESM5, detailing its components and evaluating its performance, which is crucial for interpreting its simulations in the context of this research.

The performance evaluation of GCM outputs involved comparing simulated climate variables from the CanESM5 model with observed climate data for the Mille River watershed. The analysis used historical daily climate data from 1992 to 2023. The evaluation was carried out using several statistical measures, including the Mean Relative Error (MRE), correlation coefficient (CORR), and Nash-Sutcliffe Efficiency (NSE).

- Mean Relative Error (MRE): This metric quantifies the deviation between observed and simulated data, with lower values indicating better simulation accuracy.
- Correlation Coefficient (CORR): This statistic measures the strength and direction of the relationship between observed and simulated data, with values closer to 1 indicating a better correlation.
- Nash-Sutcliffe Efficiency (NSE): This coefficient evaluates the goodness-of-fit between observed and simulated data, with values closer to 1 indicating better model performance.

The equations for these statistical measures are as follows:

Mean Relative Error (MRE):

$$\mathrm{MRE} = \frac{(\bar{\mathrm{P}} - \bar{\mathrm{O}})}{\bar{\mathrm{O}}} * 100. \tag{7}$$

Correlation Coefficient (CORR):

$$\mathrm{CORR} = \frac{\Sigma \mathrm{N}\ (\mathrm{Pi} - \bar{\mathrm{P}})(\mathrm{Oi} - \bar{\mathrm{O}})}{(\Sigma \mathrm{N}\ (\mathrm{Pi} - \bar{\mathrm{P}})^2)^{0.2} * (\Sigma \mathrm{N}\ (\mathrm{Oi} - \bar{\mathrm{O}})^2)^{0.5}}\ . \tag{8}$$

Nash-Sutcliffe Efficiency (NSE):

$$\mathrm{NSE} = \frac{1-(\Sigma \mathrm{N}\ (\mathrm{Pi}-\mathrm{Oi})^2}{\Sigma \mathrm{N}\ (\mathrm{Oi}-\bar{\mathrm{O}})^2} \qquad (9)$$

Where: P_i and O_i represent the values at the i^{th} time step (daily) in the downscaled driving-GCM simulation and observational time series, respectively. P and O are the mean values of the downscaled driving-GCM simulation and observational sequence, respectively. N is the total sample number.

These statistical measures were employed to assess the model's ability to replicate observed climate conditions. A smaller MRE indicates higher accuracy in simulating the climate data, while a higher NSE value (closer to 1) indicates better model performance. The results of this evaluation are critical for ensuring the reliability of the climate projections used in hydrological modeling for the Mille River watershed.

3.2.5.3. Trend Analysis

A variety of statistical tests are available to detect and estimate trends in time series data. One of the most widely used methods is the Mann-Kendall (MK) test, which is a non-parametric approach that does not require the data to be normally distributed (Tabari et al., 2011). The MK test is highly recommended by the World Meteorological Organization (WMO) for detecting significant trends in climate change data.

The MK test statistic is calculated as follows:

$$S = \sum_{i=1}^{n} \sum_{j=i+1}^{n-1} \mathrm{sgn}(x_j - x_i) \qquad (10)$$

Where: x_j and x_i are the sequential data values in the time series in the years j and i (i>j) and n is the length of the time series.

A positive value of S indicates an increasing trend, while a negative value indicates a decreasing trend in the data series.

The sign function sgn $(x_j - x_i)$ is defined as:

$$\mathrm{sign}(x_j - x_i)\left\{\begin{array}{ll} 1, & x_j > x_i \\ 0 & x_j = x_i \\ -1, & x_i < x_j \end{array}\right\}. \qquad (11)$$

When the sample size n > 10, the MK test statistic S is approximately normally distributed with a mean of zero and a variance calculated as:

$$\mathrm{Var}(s) = \frac{n(n-1)(2n+s)}{18} \tag{12}$$

The standardized test statistic Z is then calculated using the following equation:

$$Z = \begin{Bmatrix} \frac{(1-s)}{\sqrt{\mathrm{Var}(s)}}, & S > 0, \\ o, & S = 0 \\ \frac{(1+s)}{\sqrt{\mathrm{Var}(s)}}, & S < 0 \end{Bmatrix}. \tag{13}$$

The presence of a statistically significant monotonic increasing or decreasing trend is determined by comparing the calculated Z-score with the critical value at the desired significance level, typically 5%.

3.2.6. Impact of Climate and LULC Change on Rainfall-Runoff Processes

This study investigates the combined effects of climate and Land Use/Land Cover (LULC) changes on the rainfall-runoff processes within the Mille River Watershed. The research focuses on using the Soil and Water Assessment Tool (SWAT) model to simulate how these changes impact streamflow and runoff dynamics. Projected data for precipitation and temperature, along with current and future LULC maps derived from the CA-Markov model, are incorporated to assess both individual and combined impacts of climate and LULC changes.

The study spans from 1992 to 2023 as the baseline period, with future projections focusing on two distinct periods: near-term (2025–2055) and mid-term (2056–2085). The SWAT model is calibrated and validated using historical climate data and LULC maps. Climate variables such as wind speed, solar radiation, and relative humidity are held constant throughout future simulation periods to isolate the effects of changes in precipitation and temperature on rainfall-runoff processes.

To evaluate the impacts, three distinct simulation scenarios are developed:

- **Scenario 1 (S1):** This scenario isolates the effects of LULC changes on rainfall-runoff processes, using land use maps from various years combined with baseline climate data.
- **Scenario 2 (S2):** This scenario focuses solely on the impacts of climate change, using a baseline LULC map and future climate projections.

- **Scenario 3 (S3):** This scenario examines the combined effects of both LULC and climate changes on rainfall-runoff processes, using future LULC maps and both baseline and future climate data.

3.2.7. Climate Change Impact Modelling Using SWAT Model

The impact of climate change on hydrological processes in the Mille River Watershed is assessed using the SWAT model, incorporating downscaled climate projections from the CanESM5 model under the SSP2-4.5 and SSP5-8.5 scenarios. These projections provide daily data on precipitation and temperature for the near-term (2025–2055) and mid-term (2056–2085) periods. The SWAT model simulates the resulting changes in streamflow, runoff, and other hydrological processes due to these projected climate conditions. The results indicate significant increases in streamflow driven by higher precipitation levels under both climate scenarios. Seasonal analysis shows an intensified wet-season runoff and a potential decline in dry-season base flows, primarily due to increased evaporation rates under rising temperatures. These trends are consistent with findings from similar studies conducted in other Ethiopian basins, such as the Upper Blue Nile and the Awash Rivers, where future climate projections suggest increased runoff and altered streamflow patterns.

Model calibration and validation were performed to ensure the accuracy of the simulations, achieving high Nash-Sutcliffe Efficiency (NSE) and R^2 values. Despite the uncertainties inherent in climate projections, the SWAT model provided valuable insights into the impact of climate change on hydrological processes. These results are crucial for understanding the future water resource challenges in the Mille River Watershed and for developing effective management strategies to mitigate the effects of these changes.

3.2.8. Hydrological Modeling of Mille Watershed

3.2.8.1. Description of the SWAT Model

Hydrological models have been developed in various forms and for different purposes, providing mathematical descriptions of the components of the hydrologic cycle.

The reasons for selecting the SWAT model for this proposed study are as follows:

- The SWAT model has been successfully applied in studies related to land use land cover and climate change in different parts of the world, including Ethiopia.

- The model can simulate the required hydrological processes in the study watershed.
- It requires less demanding input data, which is advantageous.
- The SWAT model is readily and freely available.

The Soil and Water Assessment Tool (SWAT) is an open-source, semi-distributed model with a large and growing number of model applications in various studies ranging from watershed to continental scales (Arnold et al., 2012). The SWAT model can simulate and predict long-term changes in various hydrological elements under different land use types, soil types, and management practices at a large-scale complex basin. Previous studies have demonstrated the high accuracy of the SWAT model in short-term and long-term simulations of yearly and monthly mean streamflow (Zuo et al., 2016; Anand et al., 2018).

In SWAT, the watershed is divided into multiple sub-basins, which are further subdivided into hydrological response units (HRUs) consisting of homogeneous land use management, slope, and soil characteristics (Arnold et al., 2012). HRUs represent the smallest units of the watershed in which relevant hydrologic components such as evapotranspiration, surface runoff and peak rate of runoff, groundwater flow, and sediment yield can be estimated. The water balance is the driving force behind all the processes in SWAT, calculated using equation 14.

$$SW_t = SW_0 + \Sigma_{n=1}^{t}(R_{day} - Q_{surf} - E_a - W_{seep} - Q_{gw}) \quad (14)$$

Where: SW_t - is the final soil water content in (mmH_2O), SW_0 is the initial soil water content on day I (mm), t is the time [days], R_{day} is the amount of precipitation on specific day I (mmH_2O), Q_{surf} is the amount of surface runoff on a specific day I (mmH_2O), E_a is the amount of evapotranspiration on the day I (mmH_2O), W_{seep} is the amount of water entering the vadose zone from the soil profile on day i [mmH_2O], and Q_{gw} is the amount of return flow on day I (mmH_2O).

3.2.8.2. Data Input for SWAT Model

The SWAT model requires various types of data, including both spatial data and hydro-meteorological data. For this study, a Digital Elevation Model (DEM) with a resolution of 12.5m by 12.5m was downloaded from NASA's Alaska Satellite Facility (ASF) website.

(https://vertex.daac.asf.alaska.edu/) for watershed delineation within the study area. This DEM was incorporated into the SWAT model along with soil composition data and land use information to define watershed boundaries and subsequently divide the area into sub-watersheds and hydrological response units (HRUs). The DEM data was processed using ArcGIS 10.4.1. Additionally, the soil map for the study was obtained from the FAO Soil Classification portals. To integrate this soil map into the SWAT model, a user-defined soil database was created containing textual and chemical properties of the soils for each layer. These soil databases were incorporated into the SWAT model using the data management append tool in ArcGIS 10.4.1. Similarly, Land Use/Land Cover (LULC) data is a critical input for the SWAT model. It helps define the HRUs of the watershed, which in turn influences runoff, evapotranspiration, and surface erosion. Remote sensing data from Landsat 5 TM, Landsat 7 ETM+, and Landsat 9 OLI images, from 2000, 2010, and 2020, were utilized. These images were accessed in GeoTIFF format from the USGS Earth Resources Observation and Science (EROS) data center. The LULC change analysis was performed using the Earth Resource Data Analysis System (ERDAS) Imagine version 15 and ArcGIS 10.4.1 software. A lookup table was created to assign appropriate SWAT land use codes to the various LULC categories.

Climate data for the study was obtained from high-resolution global climate models within the CMIP6 framework, which were statistically downscaled. The specific climate model used was CANESM5, sourced from the CMIP6 outputs available at the Canadian Institute for Climate Studies website (https: //climate-modeling.canada.ca/). Meteorological data, including daily precipitation (mm), maximum and minimum temperatures (ºC), solar radiation (MJ/m2/day), wind speed (m/s), and relative humidity (-), were acquired from the National Meteorological Institute of Ethiopia (NMI). Additionally, observed daily streamflow data for the Mille River at the Mille gauging station was provided by the Ministry of Water and Energy (MoWE).

3.2.9. SWAT Model Setup

Writing Input Tables: During the SWAT model setup, input tables must be created to include data such as the Digital Elevation Model (DEM), soil data, land use data, weather data, and river discharge for simulating rainfall-runoff processes and calibration. The DEM, with a resolution of 12.5m by 12.5m, was downloaded from the NASA Alaska Satellite Facility (ASF) website (https://vertex.daac.asf.alaska.edu/). The DEM was preprocessed using GIS software, particularly ArcGIS, to delineate the watershed boundaries and extract relevant topographical data. Soil data, sourced from the FAO Soil Classification database, was processed and integrated with the SWAT model. This involved developing a user-specific soil database that includes textual and chemical properties of the soils, which was then linked to SWAT soil classes via a lookup table. Land use and land cover data were derived from remote sensing satellite imagery, including Landsat 5 TM, Landsat 7 ETM+, and Landsat 9 OLI. These images, spanning the years 2000, 2010, and 2020, were classified using ERDAS Imagine and ArcGIS. A lookup table was created to map LULC categories to SWAT land use codes. Weather data, including precipitation and temperature, was collected from meteorological stations near or within the study watershed. Additional weather parameters, such as solar radiation and wind speed, were either estimated using available data or derived from empirical relationships.

SWAT input data were adjusted to modify parameters like soil properties, land use types, and slopes. This adjustment is essential for obtaining accurate rainfall-runoff simulations after fixing sensitive parameters. The SWAT model simulation includes running the model, conducting sensitivity analysis, and performing calibration and validation processes.

3.2.9.1. Watershed Delineation

Watershed delineation is the first step in creating SWAT model input. It involves delineating the watershed from a DEM. Before proceeding with the spatial input data, such as the soil map, LULC map, and slope, they were projected into the same projection called UTM Zone 37N, which is the projection parameter for Ethiopia. The delineation of watersheds and sub-watersheds was conducted through the utilization of 12.5m resolution DEM data, employing the watershed delineator tools within the Arc SWAT model software. The initial stages of this process involved the establishment of the SWAT project setup, which entailed creating essential folders and databases to accommodate all pertinent data. The watershed delineation proceeded through five key stages, encompassing DEM setup, stream identification, outlet and inlet specification, watershed outlet selection and definition, and the computation of sub-basin parameters. Following the completion of the DEM setup and indication of the outlet location on the DEM, the model automatically determined flow direction and accumulation, subsequently deriving stream networks, sub-watersheds, and topographic parameters using the designated tools. The process of stream definition and determination of sub-basin sizes involved setting the threshold area, or minimum drainage area necessary to initiate stream formation, at 11065.78

hectares to reduce the number of sub-basins. In this instance, the Mille watershed was subdivided into 25 sub-basins, collectively covering an estimated total area of 5532.89 km².

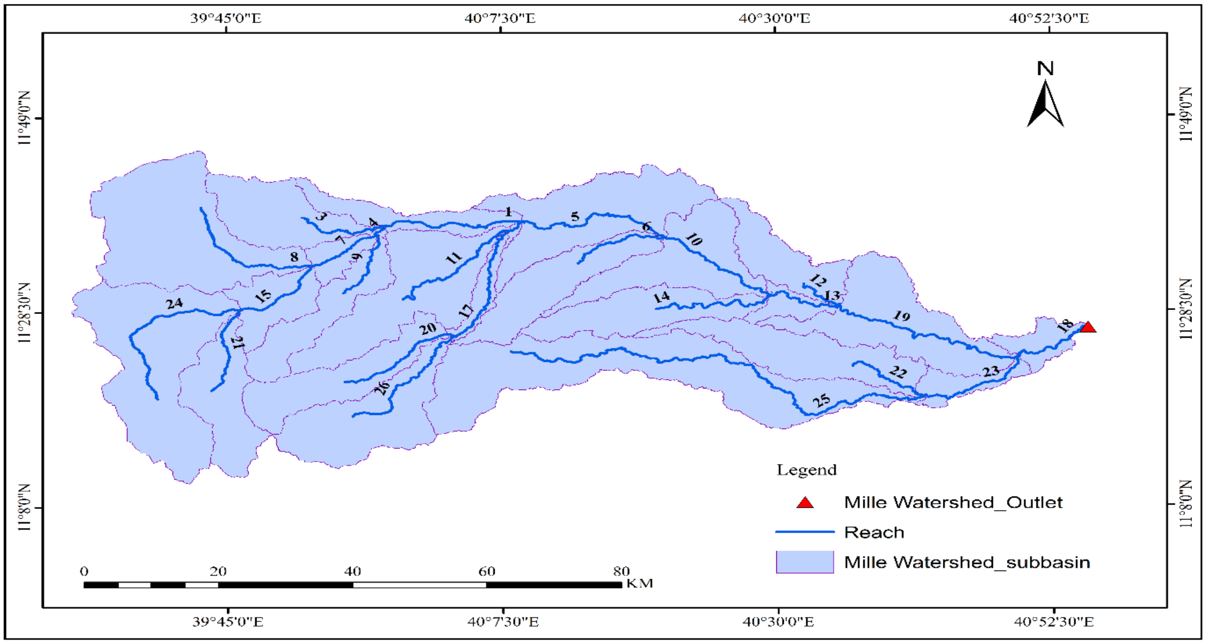

Figure 3.8: Mille watershed and sub-basin

3.2.9.2. Hydrological Response Units (HRUs)

After watershed delineation, an analysis of land use, soil composition, and slope characteristics within the watershed was conducted utilizing functionalities present in the HRU analysis menu on the Arc SWAT Toolbar. The HRU analysis tool within Arc SWAT facilitated the incorporation of land use, soil layers, and slope maps into the project, serving to define HRUs as regions characterized by homogeneous land use/cover, management practices, and soil attributes. It’s created by dividing the watershed into homogeneous sub-basins, each characterized by unique soil, slope, and land use properties. Upon the prompt creation of Hydrologic Response Units (HRUs), the model offered two common alternatives for defining them. One involved assigning a single HRU, while the other allowed for multiple HRUs to be designated.

In this investigation, the multiple HRUs alternative was utilized to enhance the accuracy of simulation outcomes. According to the SWAT user’s manual, specific thresholds such as a 20% land use threshold, 10% soil threshold, and 20% slope threshold are generally suitable for various modeling scenarios. Nevertheless, Setegn et al. (2008) proposed that defining HRUs with multiple thresholds - 10% land use, 20% soil, and 10% slope - provides a more precise estimation of runoff and sediment components. Consequently, in this study, the HRU definition incorporating these multiple thresholds was adopted to exclude minor variations in land use, soil, and slope within the watershed. Consequently, the Mille Watershed was subdivided into 82 HRUs, each characterized by unique combinations of land use and soil types.

3.2.9.3. Weather Generator

The Swat Model contains a weather generator model called WGEN. It's used to generate climatic data or to fill in missing data using monthly statistics which are calculated from existing daily data. From the values of weather generator parameters, the weather generator first separately generates precipitation for the days. Maximum temperature, minimum temperature, solar radiation, and relative humidity are then generated. Finally, the wind speed is generated independently. To generate the data, the SWAT Weather Database is designed to be a friendly tool to store and process daily weather data to be used with SWAT projects. It is capable of storing relevant daily weather information; easily creating .txt files to be used as input information during an Arcswat project setup; and efficiently calculating the WGEN statistics of several weather stations in one step run. As for any SWAT project, missing values must be entered as -999.0

3.2.9.4. SWAT Model Sensitivity Analysis

The sensitivity analysis was conducted using the built-in SWAT sensitivity analysis tool and SWAT-CUP. This analysis tool helps model users identify parameters that have the most influence on rainfall-runoff response. Sensitivity analysis involves assessing how changes in model parameters impact the model output. This process enhances comprehension of the system dynamics, parameter behavior, and model applicability, thereby boosting confidence in the model's predictions. Before calibration and validation, a sensitivity analysis was conducted to streamline parameter optimization. In this study, the semi-automated Sequential Uncertainty Fitting (SUFI 2) method was employed to identify significant parameters. Although global sensitivity analysis demands numerous simulations, this research utilized 20 simulations for calibration, ensuring accurate results. Sensitivity analysis was based on 26 years of average monthly streamflow data (1995-2018) from the watershed gauging station. The primary objective of sensitivity analysis is to gauge how changes in watersheds impact model output. This process, conducted using SWAT-CUP, involves creating new folders, transferring SWAT simulation results, and determining sensitive parameters based on observed versus simulated data in specific sub-basins. Calibration is necessary to optimize the values of the model parameters, which helps to reduce the uncertainty in model outputs. However, in such type of model with multiple parameters, the difficult task is to determine which parameters are to be calibrated. In this case, sensitivity analysis is important to identify and rank parameters that have a significant impact on the specific model output interest (Van Griensven, 2006).

3.2.9.5. SWAT Model Calibration

Model calibration involves adjusting or fine-tuning the model parameters to closely match the observed data. Calibration is a crucial component of hydrological modeling aimed at aligning model outputs with recorded streamflow data by adjusting parameters to minimize prediction uncertainty. Parameters targeted for adjustment are identified through sensitivity analysis. Additional parameters beyond those identified in sensitivity analysis are primarily utilized for calibration due to the inherent hydrological processes in the watershed. Therefore, a combination of manual and automatic, or numerical parameter optimization methods, was employed in this specific research endeavor. Initially, manual calibration of the parameters spanned twenty years (1995–2009) with a two-year warm-up phase (1993-1994) until the model's simulation results aligned with the defined model performance criteria. Subsequently, the ultimate parameter values that underwent manual calibration were utilized as the initial values for the automatic calibration process. The assessment of the SWAT model's performance involved both graphical and statistical methodologies, repeated several times until satisfactory values for surface runoff were achieved independently.

3.2.9.6. SWAT Model Validation

Model validation involves comparing the model outputs with an independent dataset without making any adjustments. The main objective of model validation is to ascertain the model's ability to forecast flow for a different time frame. For a predictive watershed model to be applicable in estimating the efficacy of potential future management strategies, it first needs to be calibrated against measured data and then tested (without further parameter adjustments) against an independent set of measured data. The model's validation was conducted using streamflow data from (2010 – 2016) over seven years in the study area. Statistical measures of model performance, such as the Nash-Sutcliffe efficiency (NSE) and coefficient of determination (R^2), were employed to evaluate the accuracy of the watershed modeling.

3.2.9.7. SWAT Model Performance Evaluation

The assessment of model fit was carried out using Nash-Sutcliffe efficiency (NSE), and coefficient of determination (R^2), to quantify the accuracy of watershed modeling.

A. Nash-Sutcliffe Efficiency

The Nash-Sutcliffe efficiency coefficient was used to assess the predictive power of the hydrological models. It quantifies the fit between observed and simulated values. The Nash-Sutcliffe efficiency coefficient (Nash and Sutcliffe, 1970) is a metric employed to evaluate the predictive capability of hydrological models. This efficiency coefficient indicates how well the observed and simulated values align. An NSE value of 1 signifies a perfect match between the simulated and observed values, while a value between 0 and 1 indicates discrepancies between the two datasets. An NSE value below zero suggests that the mean of the observed time series would have been a better predictor than the model (Krause et al., 2005). The Nash-Sutcliffe efficiency (NS) is computed using equation 15:

$$\mathrm{ENS} = 1 - \frac{\sum(\mathrm{Xi}-\mathrm{Yi})2}{\sum(\mathrm{Xi}-\mathrm{Xav})2}. \tag{15}$$

Where: X_i is the measured value; Y_i is the simulated value and X_{av} is the average observed value.

B. Coefficient of Determination

The evaluation of the model considered the coefficient of determination (R^2), which measures the consistency between simulated and observed data. A value of R^2 approaching one indicates a perfect match between the simulated and observed flow (Singh et al., 2005). The coefficient of determination (R^2) is computed using equation 16:

$$\mathrm{R}^2 = \frac{\sum(\mathrm{Xi}-\mathrm{Xav})*\sum(\mathrm{Yi}-\mathrm{Yav})}{\sum\sqrt{(\mathrm{Xi}-\mathrm{Yav})2}\sum\sqrt{(\mathrm{Yi}-\mathrm{Yav})2}}. \tag{16}$$

Where: X_i = measured value (m^3/s); X_{av} = average measured value (m^3/s); Y_i = simulated value (m^3/s) and Y_{av} is average simulated value (m^3/s).

Table 3.8: Performance ratings of recommended statistics for monthly streamflow

Performance Rating	R^2	NSE

Very Good	$0.86 < R^2 \leq 1$	$0.75 < NSE \leq 1$
Good	$0.75 < R^2 \leq 0.86$	$0.65 < NSE \leq 0.75$
Satisfactory	$0.65 < R^2 \leq 0.75$	$0.5 < NSE \leq 0.65$
Un Satisfactory	$R^2 \leq 0.65$	$NSE \leq 0.5$

To evaluate precipitation and temperature changes in meteorological events, future climate data from the ensemble average of model outputs was utilized. In this study, three different scenarios (climate change only, LULC change only, and combined climate and LULC change) were assessed to examine the separate and combined impacts of climate change and/or LULC change.

3.3. Quantifying the Impact of Future LULC Change on Rainfall-Runoff Processes

The impact of future Land Use and Land Cover (LULC) changes on rainfall-runoff processes was quantified through several systematic procedures. Initially, data collection and preparation involved acquiring satellite imagery for the years 2000, 2010, and 2020 to analyze historical LULC trends. The imagery was processed using ERDAS IMAGINE V.2015 for classification and other relevant analyses. These datasets were then incorporated into IDRISI Selva's CA-Markov model to project future LULC maps for 2030 and 2050, based on historical trends and transition probabilities. Following the generation of future LULC projections, the results were validated by comparing the projected 2020 LULC with the observed data for that year. This comparison ensured the accuracy of the model and the reliability of the future projections. Next, the SWAT model was set up using baseline LULC data from 2020. Hydrological Response Units (HRUs) were defined by combining LULC, soil, and slope data, enabling the model to capture spatial variability in hydrological responses effectively.

Once the baseline setup was complete, projected LULC maps for 2030 and 2050 were integrated into the SWAT model. These projections allowed the simulation of future scenarios to evaluate potential changes in hydrological behavior, including runoff, streamflow, and sediment transport, under varying LULC conditions.

The SWAT model was then run under these future LULC scenarios, simulating the impacts of LULC changes on hydrological processes. This simulation provided valuable insights into how changes in land cover, vegetation type, and vegetation density would affect rainfall-runoff dynamics in the watershed.

To assess the significance of different LULC changes, a sensitivity analysis was performed. This analysis identified which specific LULC changes, such as urbanization or deforestation, had the most substantial impact on hydrological responses, providing a clearer understanding of the key drivers behind changes in runoff processes.

Finally, the simulated hydrological outputs for future LULC scenarios were compared with baseline conditions. This comparison allowed for an evaluation of the effects of LULC changes on runoff, streamflow, and sediment transport, offering a comprehensive view of how future land use transformations would influence rainfall-runoff processes in the watershed.

3.4. Quantifying the Impact of Future Climate Change on Rainfall-Runoff Processes

This research assessed the impact of future climate change on rainfall-runoff processes in the Mille River Watershed using simulations based on SSP2-4.5 and SSP5-8.5 scenarios. Baseline hydrological conditions were established using historical river flow data from gauging stations (e.g., Mille, Bati, and Mersa) covering the period 1992–2023. Climate projections, including daily maximum and minimum air temperatures and precipitation, were derived from the CanESM5 model and downscaled using the Statistical Downscaling Model (SDSM). The downscaled data were validated against observed records to ensure accuracy and reliability.

The SWAT model was employed to simulate hydrological responses under projected climate conditions for near-term (2025–2055) and mid-term (2056–2085) periods. Hydro-climatic parameters, including daily precipitation and temperature changes, were incorporated to evaluate their effects on runoff, streamflow, and baseflow.

Simulations analyzed key hydrological variables under future climate scenarios, identifying precipitation intensity and temperature trends as critical factors influencing runoff dynamics.

3.5. Analyze both Climate and LULC Change Impacts on Future R-R Processes

To analyze the impacts of both land use/land cover and climate change on the rainfall-runoff processes, three scenarios were considered. The first two scenarios adopted a single-factor approach, where one driving factor was changed while keeping the other constant. The first scenario varied the land use over time while considering the climate as invariant, and the second scenario maintained the land use invariant while varying the climate. These scenarios aimed to understand the response of rainfall-runoff processes when only one driving force is changed, helping to quantify the influence of individual factors. In reality, both land use and climate change occur simultaneously over time, and the integrated effect of these factors generates the hydrologic response, which is addressed by the third scenario. From the integrated response, the contributions of land use and climate to the variability of rainfall-runoff processes are segregated using results from the other two scenarios. An in-depth analysis of the first two scenarios is conducted due to a lack of detailed studies examining the effects of land use and climate change on rainfall-runoff processes in the Mille Watershed.

3.6. General Methodology of the Study

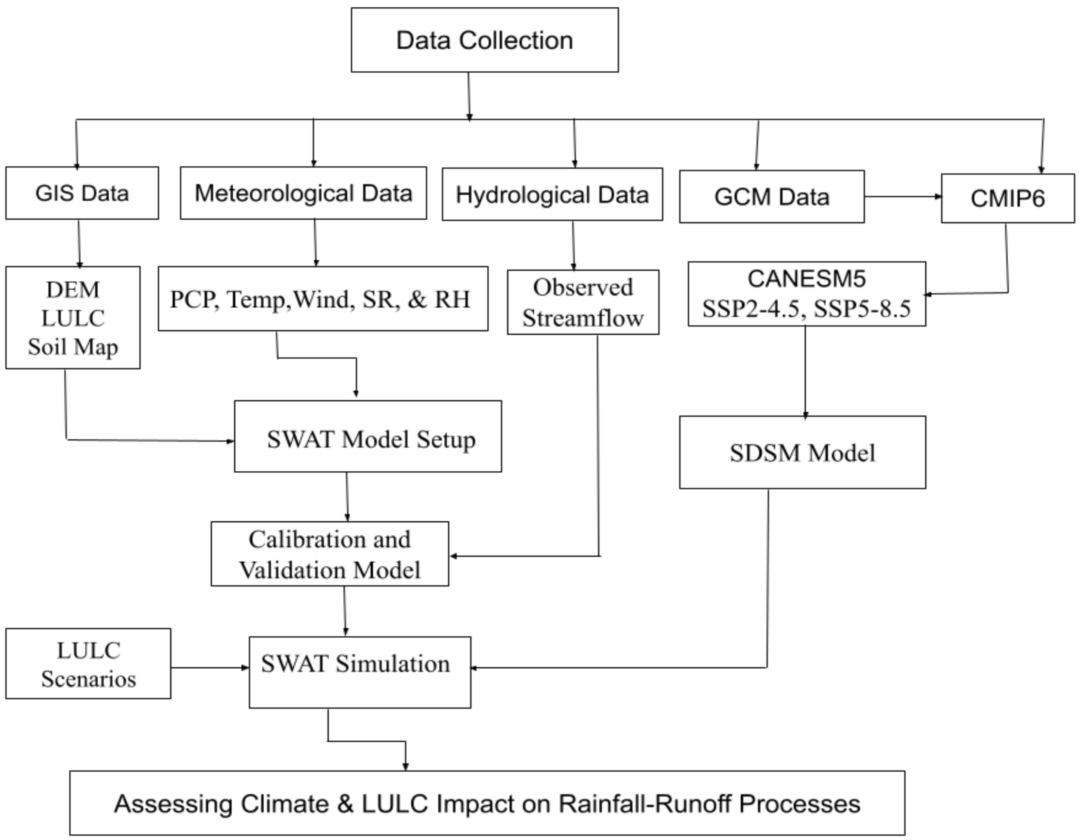

Figure 3.9: General Methodology of Study flow chart

4. RESULTS AND DISCUSSION

4.1. Land Use Land Cover Classification Accuracy Assessment

The accuracy assessment is used to determine the reliability of the classified image. The results from the accuracy assessment, obtained through random sampling, showed overall accuracy values for the images of the years 2000, 2010, and 2020 as 86.15%, 88.84%, and 90.7%, respectively. The 2020 LULC map demonstrated a higher overall accuracy compared to 2000 and 2010, which may be attributed to the higher spatial resolution of the satellite images and clearer visibility on Google Earth. Therefore, the validation dataset indicates a strong agreement between the classified image and the ground truth, as shown in Tables 4.1, 4.2, and 4.3.

Table 4.1: Confusion Matrix for LULC Classification 2000

LULC	AL	FR	ST	GL	SB	WB	BL	WL	Total	UA
AL	22	2	0	1	0	0	0	0	25	88.00%
FR	0	21	3	0	0	0	0	2	26	80.77%
ST	1	0	22	2	1	0	1	0	27	81.48%
GL	0	1	1	23	0	0	1	0	26	88.46%
SB	0	0	0	0	25	0	2	1	28	89.29%
WB	0	0	0	1	1	13	0	0	15	86.67%
BL	0	1	2	0	1	0	26	0	30	86.67%
WL	0	1	0	0	1	0	0	16	18	88.89%
Total	23	26	28	27	29	13	30	19	195	K=0.84
PA	95.65%	80.77%	78.57%	85.19%	86.21%	100.00%	86.67%	84.21%		

Overall Classification Accuracy = 86.15%

Note: AL=Agriculture Land, FR=Forest, GL=Grass/Range Land, SB=Shrub/Bush Land, ST=Settlement, WB=Water Body, BL=Barren Land, WL= Woodland UA=User Accuracy, PA=Producer Accuracy

The error matrix for 2000 reveals that Shrub/Bushland was most frequently classified accurately in that year's imagery, followed by Woodland, grass/rangeland, agricultural land, water bodies, barren land, settlements, and forest (Table 4.1). Some areas covered by grass/rangeland, scrub/bush, and forest land were occasionally misclassified as agricultural land in 2000. User accuracy for each class ranged from 80.77% for forest to 89.3% for shrub/bushland.

Table 4.2: Confusion Matrix for LULC Classification 2010

LULC	AL	FR	ST	GL	SB	WB	BL	WL	Total	UA
AL	30	1	1	0	0	0	1	0	33	90.91%
FR	1	28	2	1	0	0	0	2	34	82.35%
ST	2	0	27	1	0	0	1	0	31	87.10%
GL	0	0	1	24	0	0	1	0	26	92.31%
SB	0	1	0	1	28	0	0	1	31	90.32%
WB	0	0	0	0	1	10	0	0	11	90.91%
BL	0	1	1	0	1	0	32	0	35	91.43%
WL	0	2	0	1	0	0	0	20	23	86.96%
Total	33	33	32	28	30	10	35	23	224	K=0.87
PA	90.91%	84.85%	84.38%	85.71%	93.33%	100.00%	91.43%	86.96%		

Overall Classification Accuracy = 88.84%

Note: AL=Agriculture Land, FR=Forest, GL=Grass/Range Land, SB=Shrub/Bush Land, ST=Settlement, WB=Water Body, BL=Barren Land, WL= Woodland UA=User Accuracy, PA=Producer Accuracy

Table 4.3: Confusion Matrix for LULC Classification 2020

LULC	AL	FR	ST	GL	SB	WB	BL	WL	Total	UA
AL	41	2	0	0	1	0	0	0	44	93.18%
FR	1	35	0	1	0	0	0	1	38	92.11%
ST	1	0	36	0	1	0	2	0	40	90.00%
GL	2	0	1	34	0	0	1	0	38	89.47%
SB	0	2	0	0	40	0	0	1	43	93.02%
WB	0	0	1	0	0	15	1	0	17	88.24%
BL	2	0	1	1	2	0	48	1	55	87.27%
WL	0	1	0	0	1	0	0	23	25	92.00%
Total	47	40	39	36	45	15	52	26	300	k= 0.90
PA	87.23%	87.50%	92.31%	94.44%	88.89%	100.00%	92.31%	88.46%		

Overall Classification Accuracy = 90.7%

Note: AL=Agriculture Land, FR=Forest, GL=Grass/Range Land, SB=Shrub/Bush Land, ST=Settlement, WB=Water Body, BL=Barren Land, WL= Woodland UA=User Accuracy, PA=Producer Accuracy

The LULC map 2010 classification error matrix indicates that grass/rangeland was correctly classified, followed by barren land, agricultural land, water bodies, shrub/bush land, settlements, woodland, and forest, as shown in Table 4.2. In the 2010 classification, shrub/bush, and agricultural land were commonly misclassified as grass/rangeland, while forest and grass/rangeland were misclassified as shrub/bushland. User accuracy for each class ranged from 82.35% for barren land to 92.31% for agricultural land. The 2020 classification error matrix reveals that agricultural land was accurately classified, followed by scrub/bushland, forest, woodland, settlements, grass/rangeland, water bodies, and barren land, as shown in Table 4.3.

In the 2020 classification, agricultural, grass/rangeland, and scrub/bushland were frequently misclassified as forest, while agricultural, scrub/bush, and forest land were mistaken for grass/rangeland. The reason for the accurate classification of barren land is likely due to its well-known characteristics, which made it easy to classify. User accuracy for each class ranged from 87.27% for barren land to 93.18% for agricultural land. The user's accuracy reflects the reliability of the classification and is a more relevant measure of the classification's utility in the field.

4.2. Historical Land Use Land Cover Changes Analysis

The major land use and land cover types shown on the maps of 2000, 2010, and 2020 include agricultural land, forest, settlements, grass/rangeland, scrub/bushland, water bodies, barren land, and woodland, as presented in Table 4.4. Table 4.4 provides the area coverage, percentage change, and rate of change for each LULC category in the Mille watershed between 2000, 2010, and 2020. Agricultural land comprised the largest share of the total area at about 28.21%, followed by barren land at 27.47%, based on the 2000 LULC map, indicating that much of the area was covered by agricultural vegetation. The 2000 historical reference LULC map shows that 14.83%, 10.60%, 9.13%, 4.57%, 4.13%, and 0.71% of scrub/bushland, grass/rangeland, woodland, settlements, forest, and water body land areas, respectively, were present. The analysis showed that agricultural land increased from 28.21% to 37.46%, while settlement land increased from 4.57% to 9.60% between 2000 and 2020. The annual rate of agricultural land change showed increments of 4,252.42 ha/year from 2000 to 2010, 1,153.93 ha/year from 2010 to 2020, and 2,703.18 ha/year over the entire 2000 to 2020 period. Settlement areas showed an annual rate of increase of 2,318.09 ha/year from 2000 to 2010, 621.31 ha/year from 2010 to 2020, and 1,469.70 ha/year for the 2000 to 2020 period. Grass/rangeland area increased from 10.60% to 11.80% between 2000 and 2020, but declined to 9.93% from 2010 to 2020. In the first scenario, the area of grass/rangeland increased by 1.20%, while in the second scenario, it decreased by 1.87%. In the third scenario, grass/rangeland declined by 0.67%, respectively.

The analysis indicates that agricultural land increased from 164,841.14 ha (28.21%) in 2000 to 218,904.70 ha (37.46%) in 2020, with an annual rate of change of 2,703.18 ha/year over the 20 years. This increase reflects the expansion of agriculture to meet growing food demands due to population growth. Similarly, settlement areas expanded from 26,707.54 ha (4.57%) in 2000 to 56,101.53 ha (9.60%) in 2020, with an annual rate of change of 1,469.70 ha/year, driven by urbanization and infrastructure development.

In contrast, forest land decreased significantly from 24,160.58 ha (4.13%) in 2000 to 8,727.34 ha (1.49%) in 2020, with an annual rate of decline of -771.66 ha/year, largely due to deforestation for agricultural expansion. Shrub/bush land also saw a decline from 86,650.11 ha (14.83%) in 2000 to 64,242.08 ha (10.99%) in 2020, with an annual decline of 1,120.40 ha/year. Barren land fluctuated over the period, declining from 160,507.87 ha (27.47%) in 2000 to 142,174.94 ha (24.33%) in 2020, with an annual rate of decline of 916.65 ha/year. The decline in barren land suggests land recovery or conversion to other land uses, particularly agriculture. The overall trend indicates a decrease in natural vegetation cover, including forest and shrubland, while agricultural and settlement areas have expanded significantly due to population growth and the need for more arable land.

Table 4.4: The area coverage of LULC, percent, and rate of changes b/n 2000, 2010 and 2020

	Area(ha)			Percentage Change (%)			Rate of Change(ha/Year)		
LULC	2000	2010	2020	2000-2010	2010-2020	2000-2020	2000-2010	2010-2020	2000-2020
Agriculture	164841.14 (28.21*)	207365.38 (35.48*)	218904.70 (37.46*)	25.80	5.56	32.80	4252.42	1153.93	2703.18
Forest	24160.58 (4.13*)	7987.39 (1.37*)	8727.34 (1.49*)	-66.94	9.26	-63.88	-1617.32	73.99	-771.66
Settlement	26707.54 (4.57*)	49888.45 (8.54*)	56101.53 (9.60*)	86.80	12.45	110.06	2318.09	621.31	1469.70
Grass/Range	61958.61 (10.60*)	68970.24 (11.80*)	58014.90 (9.93*)	11.32	-15.88	-6.37	701.16	-1095.53	-197.19
Shrub/Bush	86650.11 (14.83*)	57569.46 (9.85*)	64242.08 (10.99*)	-33.56	11.59	-25.86	-2908.07	667.26	-1120.40
Water Body	4163.48 (0.71*)	3395.45 (0.58*)	3365.98 (0.58*)	-18.45	-0.87	-19.15	-76.80	-2.95	-39.88
Barren land	160507.87 (27.47*)	158664.73 (27.15*)	142174.94 (24.33*)	-1.15	-10.39	-11.42	-184.31	-1648.98	-916.65
Woodland	53366.92 (9.13*)	28526.52 (4.88*)	30801.85 (5.27*)	-46.55	7.98	-42.28	-2484.04	227.53	-1128.25

*The number in parenthesis/bracket indicates the percentage LULC

Key: - First Scenarios (S1) (2000 to 2010), Second Scenarios (S2) (2010 to 2020), and Third Scenarios (S3) (2000 to 2020).

The annual rate of grass/range land change showed increments of 701.16ha/year from 2000 to 2010, while it declined by 1095.53ha/year and 197.19ha/year between 2010 to 2020 and 2000 to 2020, respectively. Forest, barren land, woodland, and scrub/bushland showed a declining trend for the entire study period from 2000 to 2020, with the following magnitudes: 63.88%, 11.42%, 42.28%, and 25.86%. In the first scenario, the land under forest decreased by 66.94%, barren land by 1.15%, woodland by 46.55%, and scrub/bushland by 33.56%, respectively. The results for the second scenario indicate that land under forest, woodland, and scrub/bushland continued to increase by 9.26%, 7.98%, and 11.59%, respectively, while barren land decreased by 10.39%. The annual rate of decline of forest, barren land, woodland, and scrub/bushland was 1617.32ha/year, 184.31ha/year, 2484.04ha/year, and 2908.07ha/year in the first scenario. In contrast, for the second scenario, forest, woodland, and scrub/bushland increased by 73.99ha/year, 227.53ha/year, and 667.26ha/year, respectively, while barren land declined by 1648.98ha/year, as shown in (Table 4.4). The classified images were obtained after pre-processing and supervised classifications as shown in the figures below (Figure 4.1).

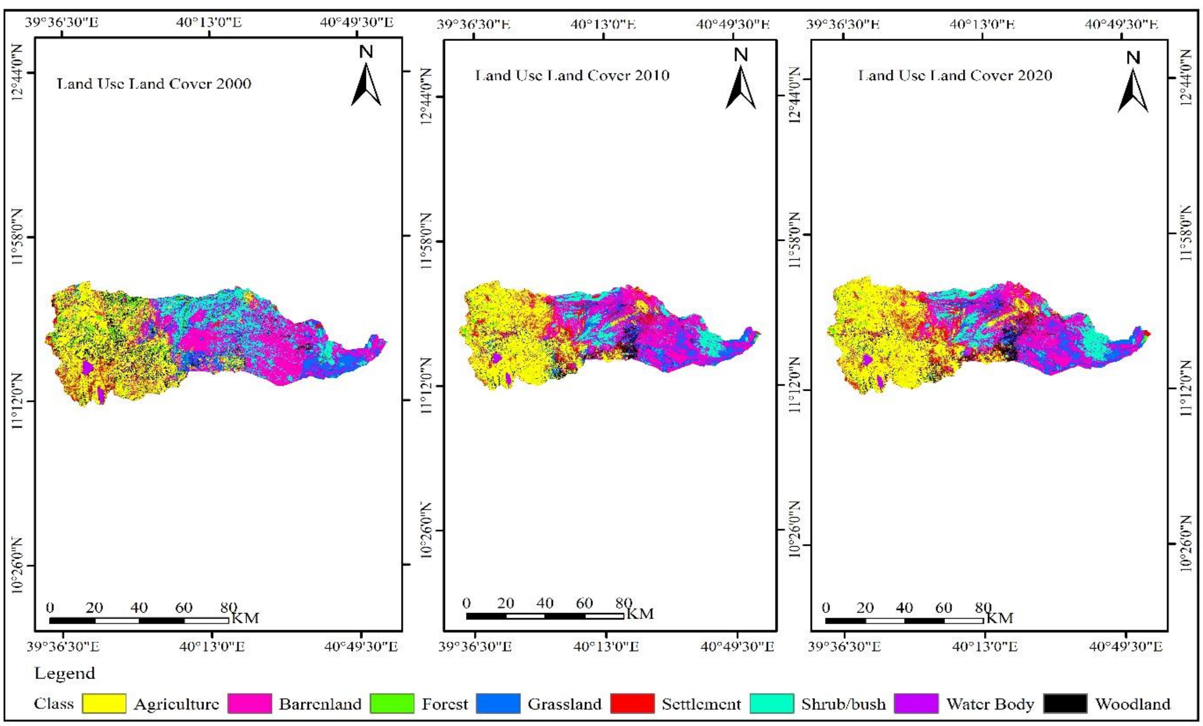

Figure 4.1: LULC Map of Mille Watershed in the periods 2000, 2010, and 2020

The increasing trend of agriculture and settlement is attributed to the expansion of human needs and population growth. Generally, the results indicate that forest land, woodland, scrub/bushland, barren land, and grass/range land decreased, while agricultural land and cultivated settlement increased. This may be due to the increasing population growth rate and the demand for more farmland. The findings of this study are consistent with other studies conducted in Ethiopia. For example, Dires and Temesgen (2020) reported that agricultural land and settlement areas increased from 1984 to 2018 in the Lake Tana Basin. Similarly, Tatek and Daniel (2019) revealed a significant increase in agriculture and settlement areas by 12% and 270%, respectively. In contrast, grasslands, forest lands, and shrublands showed a declining trend of about 40%, 21%, and 12%, respectively, in the Muga Watershed. Likewise, Mesfin (2018) reported the increasing expansion of settlement and agriculture in the Shaya watershed between 1987 and 2020. A study by Woldeamlak and Solomon (2013) also reported the expansion of open grassland, agriculture, and settlements in a tropical highland watershed in Ethiopia due to human activities such as the reduction of natural vegetation cover.

4.3. LULC Change Transition Probability Matrix between 2000 and 2020

4.3.1. Conversion between 2000 and 2010

The amount of LULC in hectares converted to or gained from other types is an important aspect of change detection. Agriculture gained about 30,044.6ha, 16,540.4ha, 16,227.7ha, 15,985.3ha, 12,577.4ha, and 4,145.0ha of land from woodland, forest, barren land, settlement, grass/range land, and scrub/bushland, respectively. Conversely, about 3,935.2ha, 16,336.4ha, 9,886.6ha, 2,344.3ha, 10,959.9ha, and 10,187.3ha of agricultural land were lost to forest, settlement, grass/range land, scrub/bush, barren land, and woodland, respectively. The change detection indicated that 9,886.6ha of agricultural land, 869.7ha of forest land, 893.6ha of settlement, 13,588.2ha of scrub/bushland, 26,436.0ha of barren land, and 4,546.1ha of woodland had significantly changed to grass/range land. Moreover, the areas of 16,336.4ha of agriculture, 2,530.9ha of forest, 6,987.2ha of scrub/bushland, 9,925.5ha of barren land, 5,776.3ha of woodland, and 4,969.9ha of grazing land had changed slightly into settlement. Gains and losses in agriculture, forest, scrub/bushland, barren land, and woodland also occurred during these periods (Table 4.5).

Table 4.5: Transition Area Matrix (ha) b/n 2000-2010 and 2010-2020 in the Mille Watershed

LULC 2000	Land Use Land Cover 2010								
LU Class	AL	FR	ST	GL	SB	WB	BL	WL	Total
AL	110949.5	3935.2	16336.4	9886.6	2344.3	241.2	10959.9	10187.3	164840.4
FR	16540.4	1076.1	2530.9	869.7	445.2	27	1406.4	1265	24160.6
ST	15985.3	808.7	3040.3	893.6	1262.5	92.1	2840.4	1583	26506
GL	12577.4	323.7	4969.9	12626.1	8253.7	0.4	20910.8	2296.6	61958.6
SB	4145	229.8	6987.2	13588.2	18877.2	5.5	39477.9	3339.3	86650.1
WB	895.2	19.3	42.7	121.7	2	2885	21.8	175.8	4163.5
BL	16227.7	651.4	9925.5	26436	24619.2	0.5	77142.5	5504.9	160507.7
WL	30044.6	943	5776.3	4546.1	1765.4	143.8	5905	4174.6	53298.9
Total	207365.2	7987.4	49609.1	68968	57569.4	3395.5	158664.7	28526.5	

LULC 2010	Land Use Land Cover 2020								
LU Class	AL	FR	ST	GL	SB	WB	BL	WL	Total
AL	160146	4659	20032.7	3729.4	1431.2	167.9	7715	9484.6	207365
FR	4556.8	2424.4	300.3	198.7	22.4	3.2	133.6	348	7987.4
ST	17645.6	469	14538	3254	2332.1	12.9	8262.2	3144.3	49658
GL	11988.4	398.5	4844.1	21681.4	4781.4	7.6	21051.5	4216.2	68969.1
SB	2851.5	18.2	2114.2	2889.8	32190.5	17083.6	421.7	3339.3	60908.8
WB	187.9	7.9	0.1	3.5	3169.3	0.6	26.1	175.8	3571.2
BL	10936.7	125.7	11146.2	23671.7	22897.1	1.4	84879.9	5006	158665
WL	10590.3	624.6	2931.2	2586.1	587.3	3.6	3048.4	8155	28526.5
Total	218903	8727.3	55906.7	58014.5	67411.4	17280.8	125538	33869.2	

4.3.2. Conversion between 2010 and 2020

The conversions of LU/LC from one class to another were revealed in all study periods. Between the 2010 and 2020 period, 17,645.6ha, 11,988.4ha, 10,936.7ha, 10,590.3ha, 4,556.8ha, and 2,851.5ha of settlement, grass/range land, barren land, woodland, forest, and shrub/bush land were converted to agricultural land, respectively. Similarly, 20,032.7ha, 9,484.6ha, 7,715ha, 4,659ha, 3,729.4ha, and 1,431.2ha of agricultural land were lost to other LULC categories. During these periods, a significant area of woodland was converted from agriculture (9,484.6ha), barren land (5,006ha), grassland (4,216.2ha), scrub/bushland (3,339.3ha), settlement (3,144.3ha), and forest (348ha). In reverse, there was also considerable conversion of woodland to other categories. During this period, some areas of settlement were also converted from farmland (20,032.7ha), forestland (300.3ha), barren land (11,146.2ha), grassland (4,844.1ha), woodland (2,931.2ha), and scrub/bushland (2,114.2ha). Although, about 17,645.6ha, 469.0ha, 3,254.0ha, 2,332.1ha, 8,262.2ha, and 3,144.3ha of the settlement were also converted to agriculture, forest, grass/range land, scrub/bushland, barren land, and woodland, respectively. Gains and losses in agriculture, forest, barren land, woodland, scrub/bushland, and grass/range land took place during this study period. A significant amount of gains and losses in the grass/range land occurred during these periods. The gain of LULC for each class was determined from the result of persistence and the total column value, while the loss is from the total row and the persistence (Figure 4.2).

4.3.3. Conversion between 2000 and 2020

The conversions of LU/LC from one class to another were revealed in all study periods. Between 2010 and 2020, 18,611.5ha, 17,167.2ha, 13,924.1ha, 15,559.4ha, 6,177.1ha, and 31,662.5ha of barren land, forest, grassland, settlement, shrub/bush, and woodland were converted to agricultural land, respectively. Similarly, 9,554.3ha, 4,087.5ha, 4,875ha, 18,645.2ha, 2,494ha, and 10,121.6ha of agricultural land were lost to other LULC categories. During these periods, a significant area of woodland was converted from agriculture (10,121.6ha), barren land (6,558.3ha), grassland (2,524.6ha), scrub/bushland (4,211.3ha), settlement (1,671.2ha), and forest (1,140.1ha). In reverse, there was also considerable conversion of woodland to other categories. During this period, some areas of settlement were also converted from farmland (18,645.2ha), forestland (2,801.9ha), barren land (11,712.4ha), grassland (5,556.8ha), woodland (6,189.6ha), and scrub/bushland (7,299.9ha). Although, about 15,559.4ha, 2,092.1ha, 1,098.8ha, 631.2ha, 1,764.1ha, and 1,671.2ha of settlement were also converted to agriculture, barren land, forest, grassland, shrub/bush, and woodland, respectively.

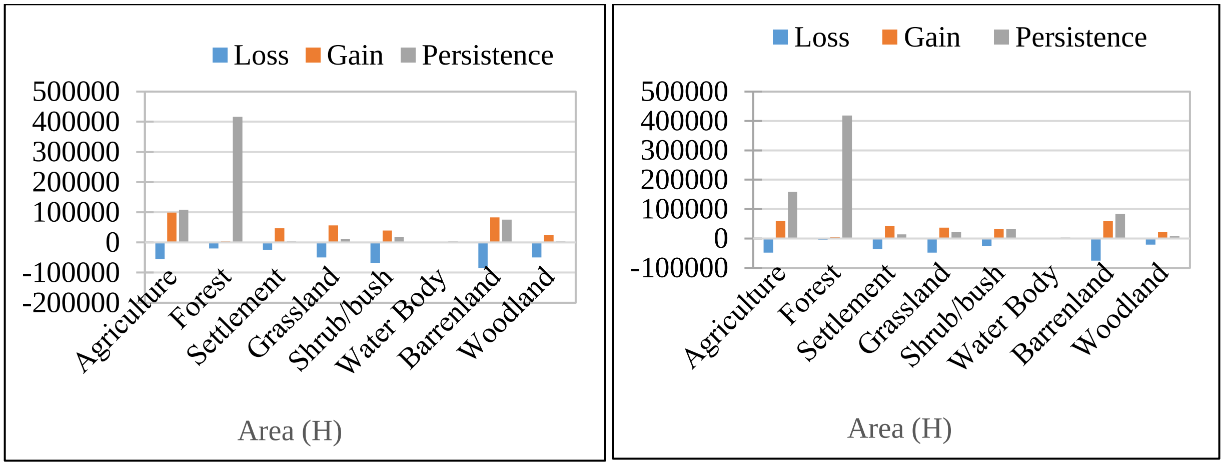

Figure 4.2: Gain and Loss area of LULC class in (2000-2010) and (2010-2020).

The gains and losses of the LULC during the study period were derived from the cross-tabulation of 2000, 2010, and 2020.

4.4. Future Land Use Land Cover (LULC) Change Prediction

4.4.1. Validation of CA-Markov Model

To validate the predicted LULC changes, the areas simulated by the model were compared to the actual land use areas. Additionally, the observed 2020 LULC was cross-compared with the simulated 2020 LULC to evaluate the model performance using kappa indexing. The results in Table 4.6 indicate that forest, shrub/bushlands, settlement, and woodland had the best agreement between observed and simulated values, as shown in Figure 4.4.

Table 4.6: Comparison of actual and projected LULC 2020

	Simulated		Classified	
LULC Types	Area(ha)	Percent (%)	Area(ha)	Percent (%)
Agriculture	202288.36	34.75	218904.70	37.59
Forest	16325.50	2.80	8727.34	1.50
Settlement	48090.32	8.26	56101.53	9.63
Grassland	68592.47	11.78	58014.90	9.96
Shrub/bush	57414.93	9.86	64242.08	11.03
Water Body	3379.17	0.58	3365.98	0.58
Barren land	158011.87	27.14	142174.94	24.41

Woodland	28008.13	4.81	30801.85	5.29
Total	582110.76	100.00	582333.32	100.00

The simulated land use land cover (LULC) map generated by the model shows that shrub/bushland coverage areas were underestimated compared to actual values, while grassland and barren land coverage areas were overestimated. The kappa index values greater than 80% indicate good agreement between the projected and actual LULC maps.

Table 4.7: The K-index values of the simulated LULC map of 2020

Index	Value
K no	0.873
K locations	0.9024
K locations Strata	0.9024
K standard	0.83

All indices are greater than 80%, showing a good overall agreement and projection ability of the model. Therefore, the CA-Markov model is robust for simulating and accurately predicting future LULCs.

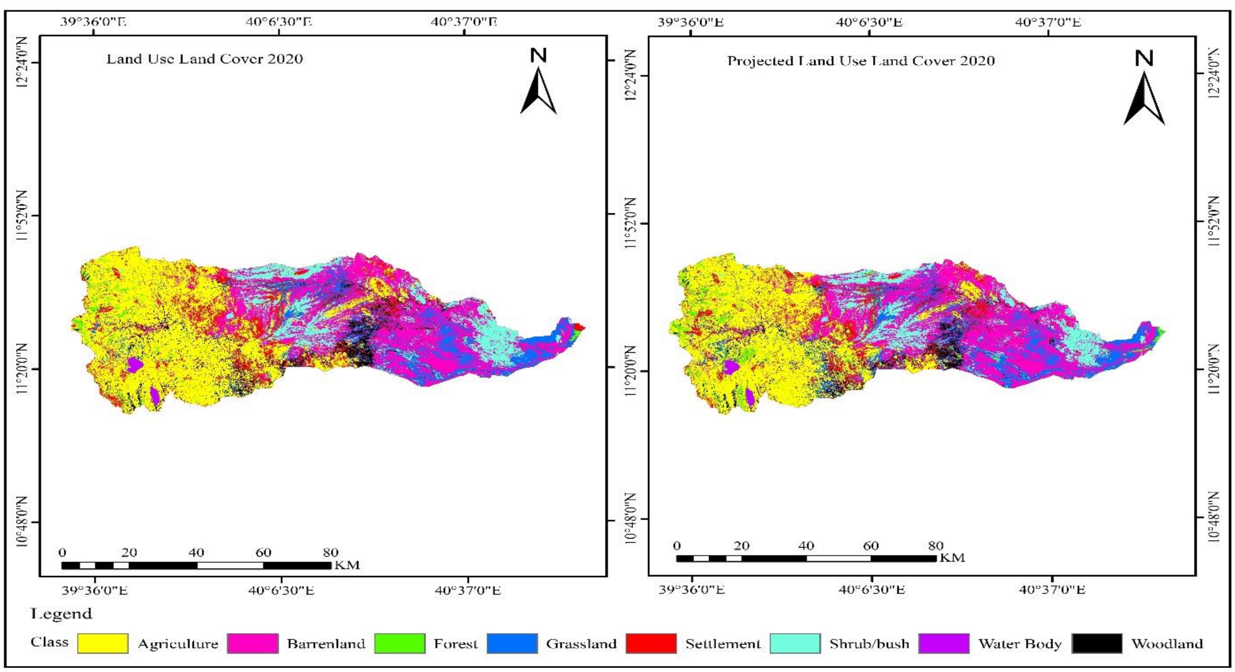

Figure 4.3: Simulated and Observed LULC Map of 2020

4.4.2. Predicted Future Land Use Land Cover Changes

The future prediction of LULC for 2030 and 2050 was executed using the 2020 land use map as a base map. The future prediction utilized the 2020 land use map as a baseline. The results indicate that in 2030, agriculture, forest, settlement, grass/range land, shrub/bush, and barren land are predicted to increase, while waterbody is predicted to remain unchanged. When comparing the predicted LULC between 2030 and 2050, agriculture, forest, grassland, and settlements showed an identical increasing trend, while barren lands, scrub/bushlands, and woodlands showed a decreasing trend as depicted in Figure 4.4. Specifically, the results predict that agriculture and settlements will increase by 4.79% and 15.19%, respectively, from 2020 to 2050. The predicted annual increases in agriculture and settlements were 839.41 hectares/year and 72.74 hectares/year from 2020 to 2030, and 1242.91 hectares/year and 97.98 hectares/year from 2030 to 2050, respectively. Overall, the results anticipate agriculture and settlements will increase by 1108.41 hectares/year and 89.57 hectares/year from 2020 to 2050, respectively.

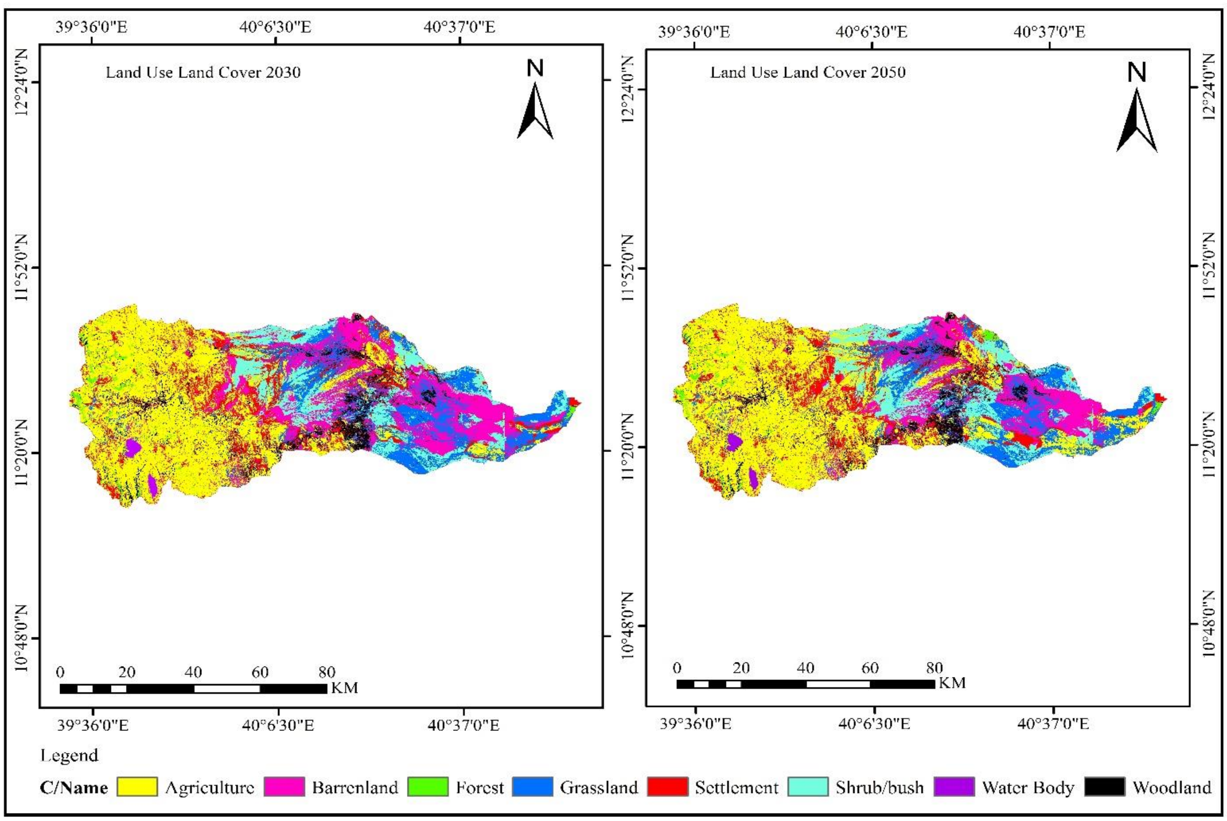

Figure 4.4: Predicted LULC Map of the years 2030 and 2050

Based on the LULC prediction results, forest lands were predicted to increase by 11.04% between 2020 and 2030 at the expense of other LU/LC categories, mainly woodlands, scrub/bush, grass/range lands, and agricultural lands, as shown in Table 4.8. Shifting cultivation practices contributed to the conversion of woodlands to rangelands in the lowland parts of the watershed, creating large openings in woodlands after cultivation is abandoned or due to the continuous increase in future conservation works. The predicted grass/range land cover slightly declined by 31.07% from 2020 to 2030 but increased by 3.44% from 2030 to 2050, and again greatly decreased by 28.70% from 2020 to 2050 overall. The LULC prediction results from this study agree with previous studies conducted in Ethiopia. For example, Bireda (2020) reported the expansion of grasslands between 1973 and 2020, with almost 80% obtained from cultivated lands in Fagita Lekoma Worked, Awi Zone, and Northwestern Ethiopia.

Table 4.8: The area coverage of LULC, percent, and rate of changes b/n 2020, 2030, and 2050

	Area(ha)			Percentage Change (%)			Rate of Change(ha/Year)		
LULC	2020	2030	2050	2020-2030	2030-2050	2020-2050	2020-2030	2030-2050	2020-2050
Agriculture	218904.70 (37.6*)	227298.82 (39.05*)	252157.06 (43.01*)	3.83	10.94	15.19	839.41	1242.91	1108.41
Forest	8727.34 (1.5*)	9690.56 (1.66*)	11122.06 (1.69*)	11.04	14.77	27.44	96.32	71.58	79.82
Settlement	56101.53 (9.6*)	56828.96 (9.76*)	58788.63 (11.70*)	1.30	3.45	4.79	72.74	97.98	89.57
Grassland	58014.90 (10.0*)	39987.02 (6.87*)	41363.45 (12.93*)	-31.07	3.44	-28.70	-1802.79	68.82	-555.05
Shrub/bush	64242.08 (11.0*)	64212.05 (11.03*)	63869.40 (15.07*)	-0.05	-0.53	-0.58	-3.00	-17.13	-12.42
Water Body	3365.98 (0.6*)	3365.98 (0.58*)	3365.98 (0.58*)	0.00	0.00	0.00	0.00	0.00	0.00
Barrenland	142174.94 (10.0*)	149991.65 (25.77*)	124727.05 (7.92*)	5.50	-16.84	-12.27	781.67	-1263.23	-581.60
Woodland	30801.85 (11.0*)	30759.54 (5.28*)	30745.05 (6.42*)	-0.14	-0.05	-0.18	-4.23	-0.72	-1.89

*The number in parenthesis/bracket indicates the percentage of LULC

Key: - First scenarios (S1) (2020 to 2030), Second Scenarios (S2) (2030 to 2050), and Third Scenarios (S3) (2020 to 2050).

Similarly, Afera (2018) also reported the expansion of grasslands replacing built-up areas and water bodies in the Woreta Zuria watershed in Ethiopia between 1997 and 2017. The predicted scrub/bushland and barren land coverage showed a continuous declining trend from 2020 to 2050 by 0.58% and 12.27%, respectively, with annual decline rates of 12.42 hectares/year and 581.60 hectares/year. Woodland showed a slightly decreasing trend from 2020 to 2030 by 0.14% and also slightly declined by 0.18% from 2030 to 2050. The annual woodland decline rate was 4.23 hectares/year and 1.89 hectares/year from 2020 to 2030 and 2020 to 2050, respectively. The predicted decreases in woodland from 2020 to 2030 may be due to unplanned afforestation and green legacy strategies by the government. Semegnew et al. (2021) summarized that forest land declined to 77.8% in 2017, while farmland, settlement, and grassland increased by 17.4%, 3.4%, and 1.4%, respectively, from 2002 to 2017. Similarly, Adane and Getachew (2017) reported an overall increase in grass/range land from 2006 to 2026 in the Bale eco-region. Therefore, predicting LULC changes using time series data is important for developing future LULC management plans. A rational land use plan should be proposed to sustain the livelihoods of local communities.

4.5. LULC Transition Probability Matrix between 2020 to 2050

4.5.1. Conversion between 2020 and 2030

In these periods, 5179.12 ha, 20192.47 ha, 1306.31 ha, 449.74 ha, 10587.19 ha, and 1999.34 ha of agricultural land will be converted from forest land, settlement, grass/range land, scrub/bushland, barren land, and woodland, respectively. About 22363.91 ha, 79.74 ha, 558.30 ha, 190.11 ha, 999.69 ha, and 607.61 ha of settlement will also revert from agriculture, forest, grass/range land, scrub/bushland, barren land, and woodland, respectively. Although agricultural and settlement land will be converted from other land uses, there will also be a significant loss of agricultural and settlement land to other land uses (Table 4.9). Between these periods, there will be a huge loss of forest, grass/range land, scrub/bushland, barren land, and woodland to other land uses. For example, about 5179.12 ha, 79.74 ha, 17.99 ha, 15.93 ha, and 108.30 ha of forest land will be converted to agriculture, settlement, grass/range land, barren land, and woodland, respectively. About 1999.34 ha, 105.34 ha, 607.61 ha, 330.71 ha, 17.50 ha, and 520.61 ha of woodland will also be converted to agriculture, forest, settlement, grass/range land, scrub/bushland, and barren land, respectively. The grass/range land converted to agricultural land, forest, settlement, scrub/bushland, barren land, and woodland, will be 1306.31 ha, 358.37 ha, 558.30 ha, 290.04 ha, 18164.34 ha, and 513.58 ha, respectively.

4.5.2. Conversion between 2030 and 2050

The significant increase of agricultural land, forest land, and settlement with the sharp decline of grass/range and scrub/bushland in the watershed were the major transformations observed. However barren land and woodland increased in one period and declined in another period of the study as shown in Table 4.8. For example, 416.37 ha, 6148.6 ha, 111.81 ha, 146.21 ha, 23415 ha, and 103.58 ha of agricultural land will be reverted from forest, settlement, grass/range, scrub/bush, barren, and woodland, respectively. Conversely, about 1140.81 ha of forest, 4114.17 ha of settlement, 53.53 ha of grass/range land, 38.78 ha of scrub/bush, 77.45 ha of barren, and 63.00 ha of woodland were lost from agricultural land, respectively. The conversions of agricultural land (4114.17 ha), barren land (80.94 ha), woodland (12.59 ha), grass/range land (16.81 ha), scrub/bush land (7.46 ha), and forest (0.01 ha) were the major contributing land uses for settlement. Conversely, about 6148.60 ha of agriculture, 0.49 ha of forest, 26.26 ha of grass/range, 10.63 ha of scrub/bush, 69.84 ha of barren land, and 13.41 ha of woodland were lost from settlement, respectively. An estimated 103.58 ha, 4.29 ha, 12.59 ha, 11.86 ha, and 10.93 ha of woodland were also converted to agriculture, forest, settlement, grass/range land, and barren land, respectively. The agricultural land, which is the highest class, has 221804.25 ha with the probability of remaining as agricultural land in 2030-2050. In reverse, there was also a considerable gain and loss of barren land to other categories. The major reason for the reduction of grassland was the high productivity of agricultural lands and the mitigation of people in search of food for their cattle in the forest and woodland (Table 4.9). In 2030-2050, the two highest class losses were the change of barren land to agricultural land by 23415.00 ha and settlement land to agriculture by 6148.60 ha. The minimum loss of LULC category was observed from settlement to forest (0.49 ha) and forest to barren land (0.22 ha).

Table 4.9: Transition Area Matrix (ha) b/n 2020–2030 and 2030–2050 period in Study Area

Land Use Land Cover 2020	Land Use Land Cover 2030									
	LU	AL	FR	ST	GL	SB	WB	BL	WL	Total
	AL	187542.15	5288.98	22363.91	722.72	290.92	20.17	859.15	1814.73	218902.71
	FR	5179.12	3326.22	79.74	17.99	0	0	15.93	108.3	8727.31
	ST	20192.47	577.53	31952.92	466	208	0	1686.61	718.35	55801.88
	GL	1306.31	358.37	558.3	36823.29	290.04	0	18164.34	513.58	58014.24
	SB	449.74	20.96	190.11	229.46	61319.06	0	2014.4	18.37	64242.08
	WB	20.17	0.05	0	0	0.01	3345.72	0	0.04	3365.99
	BL	10587.19	10.41	999.69	1395.89	2086.52	0	126729.57	365.48	142174.75
	WL	1999.34	105.34	607.61	330.71	17.5	0.09	520.61	27220.49	30801.69
	Total	227276.49	9687.85	56752.27	39986.05	64212.05	3365.98	149990.6	30759.34	

Land Use Land Cover 2030	Land Use Land Cover 2050									
	LU	AL	FR	ST	GL	SB	WB	BL	WL	Total
	AL	221804.25	1140.81	4114.17	53.53	38.78	0	77.45	63	227291.99
	FR	416.37	9268.36	0.01	1.07	0	0	0.22	4.26	9690.28
	ST	6148.6	0.49	50555.48	26.26	10.63	0	69.84	13.41	56824.69
	GL	111.81	3.17	16.81	39489.52	1.57	0	359.77	4.37	39987.02
	SB	146.21	323.23	7.46	2.58	63707.17	0	25.4	0	64212.05
	WB	0	0	0	0	0	3365.98	0	0	3365.98
	BL	23415	378.66	80.94	1778.63	111.25	0	124183.43	43.73	149991.65
	WL	103.58	4.29	12.59	11.86	0	0	10.93	30616.29	30759.54
	Total	252145.81	11119.01	54787.46	41363.45	63869.4	3365.98	124727.05	30745.05	

Note: The shade numbers indicate the unchanged LULC proportions

Generally, the patterns of LULC change showed that the agricultural land gained the most area compared to the other LULC types.

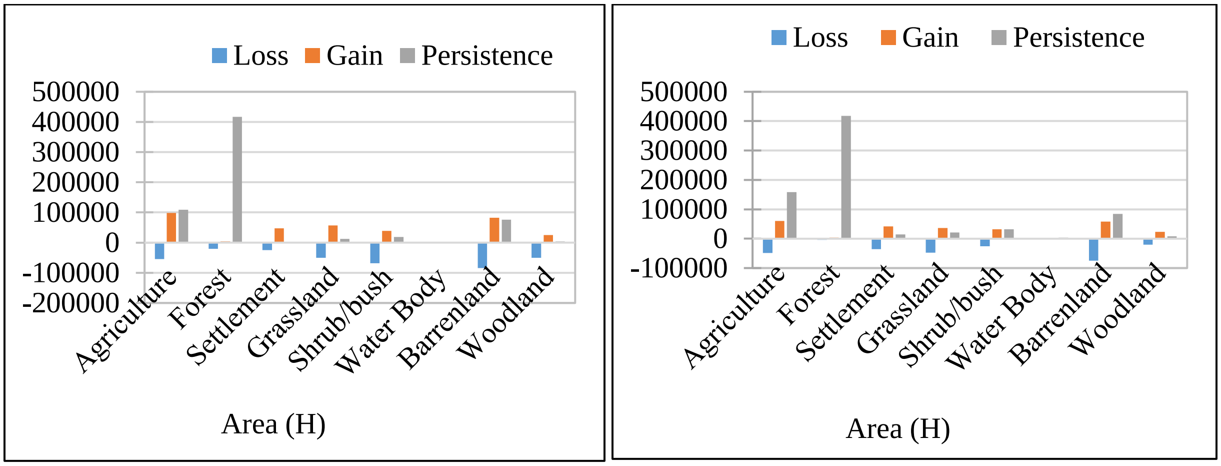

Figure 4.5: Gain, Loss, and Persistence area of LULC class in (2020-2030) and (2030-2050).

The significant increase of agricultural land, forest land, settlement, and grass/range land, with the sharp decline of scrub/bushland, barren land, and woodland, experienced a reduction in coverage throughout the study periods. The greatest reduction rate was observed in barren land. In general, the study shows that the agriculture and settlement area increase was consistent with (Megersa et al., 2021) who reported the future projection of agricultural land increased from 61.19% in 2019 to 72.98% in 2030 and 73.24% in 2050, whereas forest cover will further degrade from 16.94% in 2019 to 8.07% in 2050. Similarly, the predicted result for the years 2019 to 2050 showed an increase in urban land from 1.2% in 2019 to 3.8% in 2050. (Birhan et al., 2021) prediction of the LULC change using the CA-Markov chain model indicates that cropland, tree cover, and built-up areas are likely to increase by the 2020s, 2050s, and 2080s in the Lake Tana Basin, upper Blue Nile River Basin. (Wakjira et al., 2020) Reported that agricultural land, urban, and built-up areas continuously increased while forest land decreased throughout the study period from 1987 to 2055, respectively. Therefore, to mitigate the rapid rates of LULC conversions at the watershed, the application of integrated watershed management strategies, managing rapid population growth, afforestation of degraded or deforested areas, and reducing the dependency of locals on forest products is critically important.

4.6. Future Climate Projection

4.6.1. Precipitation Projection under SSP2-4.5 and SSP5-8.5

4.6.1.1. Projected Rainfall under SSP2-4.5

The seasonal rainfall distribution under SSP2-4.5 and SSP5-8.5 scenarios were similar to the baseline period. However, the mean annual rainfalls under SSP2-4.5 and SSP5-8.5 scenarios slightly increased than the baseline period except in the near-term under SSP2-4.5 of the study watershed. The mean annual rainfall is projected to increase by 7.17mm and 14.1mm for the near and midterm period compared to baseline under SSP2-4.5 scenarios, respectively. The projections of mean annual rainfall showed a slight increasing trend for near and midterm according to scenarios SSP2-4.5. For scenario SSP5-8.5 the projected mean annual rainfall is higher compared to scenario SSP2-4.5. This increase is mainly due to the projected increases in wet season rainfall, partially offset by projected decreases in dry season rainfall (Figure 4.6)

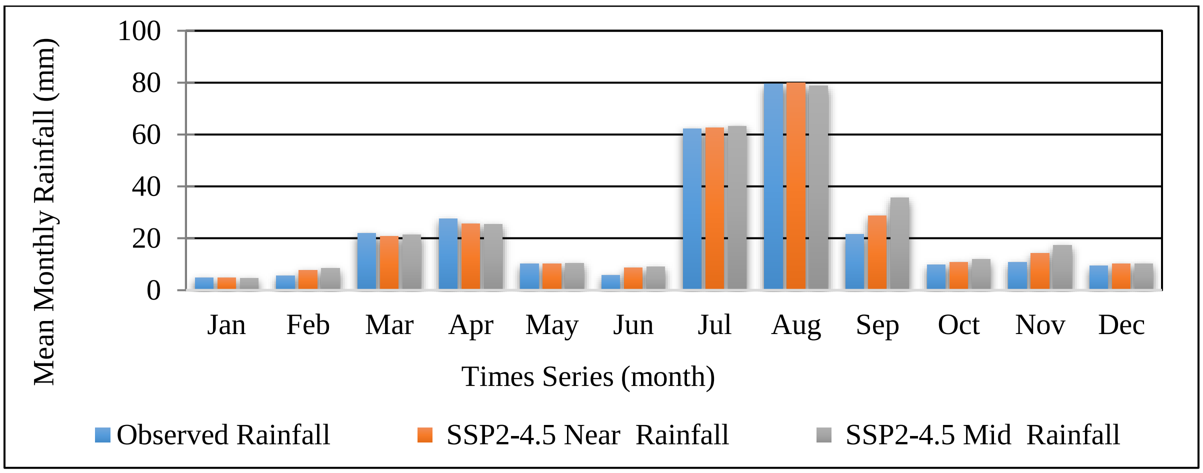

Figure 4.6: Mean monthly precipitation under SSP2-4.5 scenarios for near and mid-future periods Compared to the baseline period.

The seasonal classifications were made based on rainfall patterns of the study area, defining the Dry season (January, February, May, June, October and December) and Wet season (March, April, July, August, September, and November). Therefore, this classification system is only applicable to the northeastern region of Ethiopia, which experiences a bimodal rainfall type. The maximum increase in wet season rainfall was 80.02 mm in the near-term under the SSP2-4.5 scenarios. The projected mean monthly rainfall exhibits inconsistent patterns and magnitudes of change under the SSP2-4.5 and SSP5-8.5 scenarios. In the near-term, mean monthly rainfall may increase during the dry season (February, May, June, October, and December), with the highest increase in June (48.6%), while decreases are observed in January, with the most significant decrease in June (0.5%). Similarly, in the midterm, mean monthly rainfall is projected to increase across the dry season (February, May, June, October and December), with the maximum increase in June (54.1%), while decreases are expected in January showing the decrease (-4.9%) under the SSP2-4.5 scenario, compared to the baseline period.

In the wet season, mean monthly rainfall in the study watershed is projected to increase during July, August, September, and November, with the highest increase in September (33.4%), while decreases are anticipated in March, and April, with the largest decrease in April (-7.0%) in the near-term under the SSP2-4.5 scenario. In the midterm, mean monthly rainfall is expected to rise during the wet season (July, September, and November), with the maximum increase occurring in September (65.6%), while decreases are projected in March, April, and August, with April showing the most significant decrease (-8.0%) under the SSP2-4.5 scenario, as illustrated in (Figure 4.7).

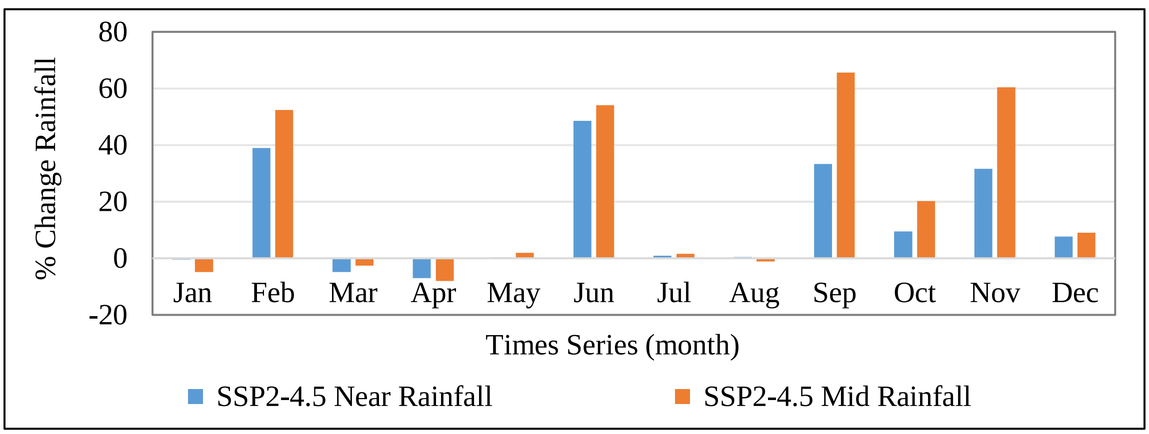

Figure 4.7: Percentage Changes of monthly rainfall for near and midterm under SSP2-4.5 scenarios from baseline period

The average monthly precipitation projected under SSP2-4.5 is expected to increase from 1.93 mm to 14.1 mm, with the largest rise occurring in September. However, some months, such as April, might see a slight decline in precipitation compared to the baseline period. This variability in precipitation patterns suggests a complex response to changing climate conditions in the SSP2-4.5 scenarios.

4.6.1.2. Projected Precipitation under SSP5-8.5

The projected changes in precipitation vary with mean annual and seasonal patterns under the SSP5-8.5 scenarios. The mean annual rainfall projection shows a slight decrease of 4.85 mm in the near term, while an increase of 17.56 mm is anticipated in the midterm compared to the baseline period. Similar to temperature trends, rainfall simulations under SSP5-8.5 are significantly higher than those under SSP2-4.5 in the watershed, despite rainfall being projected to decrease in the near term.

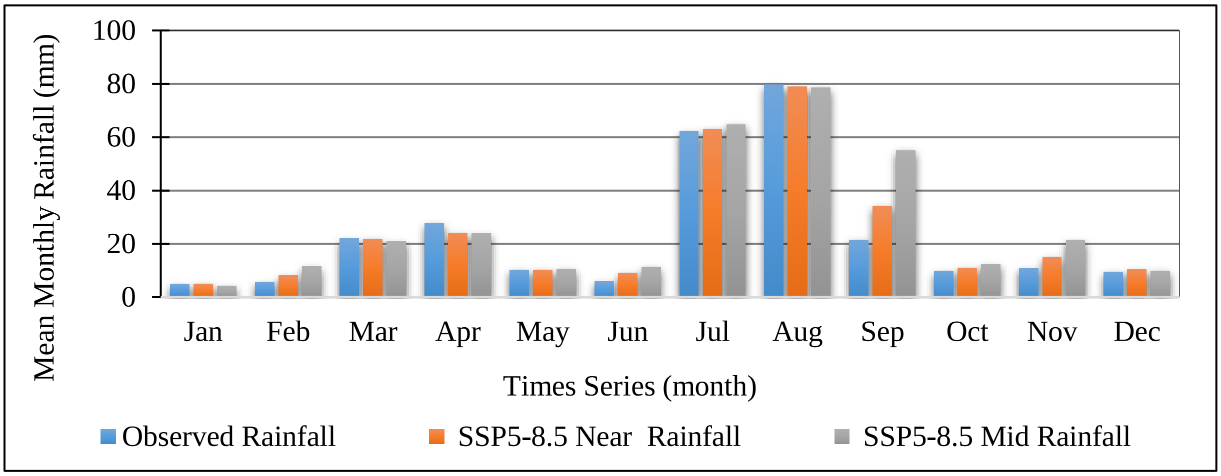

Figure 4.8: Mean monthly precipitation under SSP5-8.5 scenarios for near and mid-future periods Compared to the baseline period.

Under SSP5-8.5, the mean seasonal rainfall is projected to increase during both dry and wet seasons. For the midterm, rainfall is expected to increase, with a maximum rise of 33.54 mm in the wet season, while it is projected to decrease by 3.6 mm in the near-term dry season compared to the baseline (Figure 4.8). The changes in mean monthly rainfall are not uniform; some months will see increases while others will experience decreases. Seasonal rainfall is projected to increase during the dry season in January, February, May, June, October, and December, with the highest increase in June at 54.8% and 94.9% for the near and midterms under SSP5-8.5 scenarios, respectively. A decrease in projected rainfall of 11.7% is expected in January during the midterm under SSP5-8.5 compared to the baseline. Similarly, during the wet season, the mean monthly rainfall is projected to increase in July, September, and November, with September showing a maximum increase of 59.1%. Conversely, decreases are expected in March, April, and August, with the most significant drop of 13.0% in April during the near term under SSP5-8.5 compared to the baseline.

The projected mean seasonal precipitation under SSP5-8.5 indicates an increasing trend in the wet season from 59.1% to 156.1%, while dry season precipitation increases from 54.8% to 106.0% in the near and midterms, respectively. The increase in precipitation is more pronounced in the midterm, reflecting the higher emission scenario of SSP5-8.5.

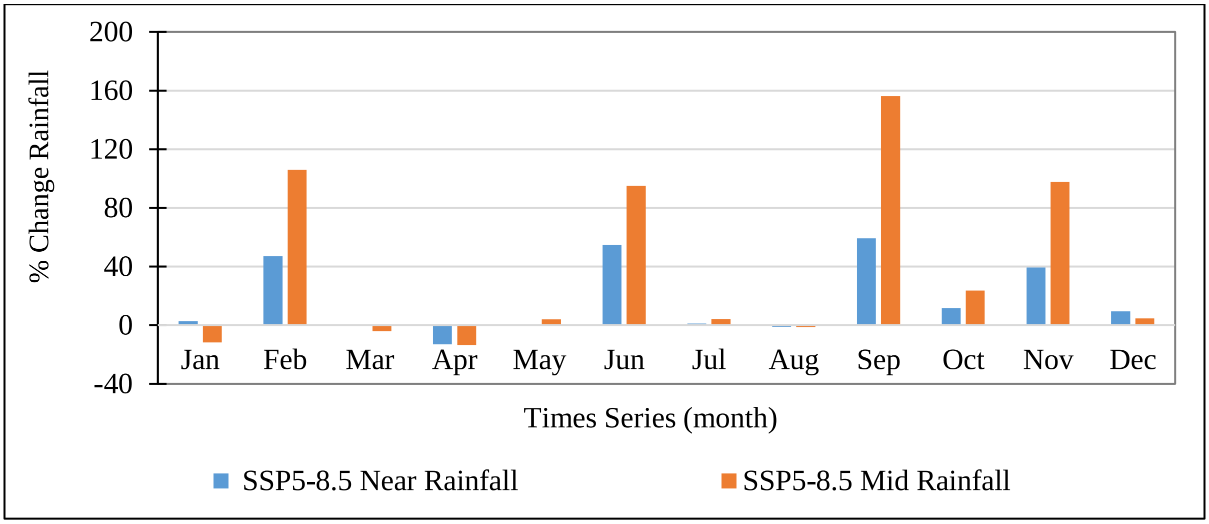

Figure 4.9: Percentage Changes of monthly rainfall for near-term and mid-term under SSP5-8.5 scenarios from the baseline period

In the midterm, mean monthly rainfall is expected to increase in the wet season (July, September, and November), with the maximum increase in September at 156.1%. A decrease is anticipated in March, April, and August, with the greatest decline in April of 13.6% under SSP5-8.5 compared to the baseline period. Overall, future precipitation projections indicate an increasing trend annually when compared to the baseline under both SSP2-4.5 and SSP5-8.5 scenarios. Figure 4.9 illustrates these changes, with upward arrows indicating increases and downward arrows indicating decreases from the baseline period.

Multiple research studies indicate a significant increase in future rainfall across various Ethiopian river basins, driven by climate change scenarios. Studies show that mean annual precipitation is projected to rise, with varying percentages depending on the region and scenario. For instance, research (Shawul & Chakma, 2020) in the Blue Nile basin indicates that the variability in projected rainfall changes with potential increases ranging from -14% to +16% in the dry season and -13%

to +12% in the wet season. Similarly, Mellander et al. (2017) predict a 6% increase in annual mean rainfall for the upper Blue Nile Basin between 2050 and 2100, maintaining historical spatial patterns. Furthermore, Tsegaye et al. (2023) projected an 8% increase in the 2050s and 10% in the 2080s for major river basins, including the awash basin. In addition, Setegn et al. (2014) suggested a potential rise of 20% in the Lake Tana Basin, part of the upper Blue Nile River Basin.

4.6.2. Temperature Projection under SSP2-4.5 and SSP5-8.5 Scenarios

4.6.2.1. Projected Maximum and Minimum Temperature under SSP2-4.5

The statistically downscaled mean annual maximum and minimum temperatures are projected to show an upward trend in both the near and midterms under the SSP2-4.5 and SSP5-8.5 scenarios. Compared to the baseline period, seasonal changes in maximum and minimum temperatures are expected to increase in the watershed under these scenarios. As a result, both baseline and projected minimum and maximum temperatures exhibit a similar seasonal trend under both scenarios. The mean annual maximum temperature is anticipated to rise by 0.22°C to 0.38°C under SSP2-4.5 scenarios in the near and midterms, respectively. Likewise, the mean annual minimum temperature is expected to rise by 0.04°C to 0.12°C compared to the baseline under SSP2-4.5 scenarios.

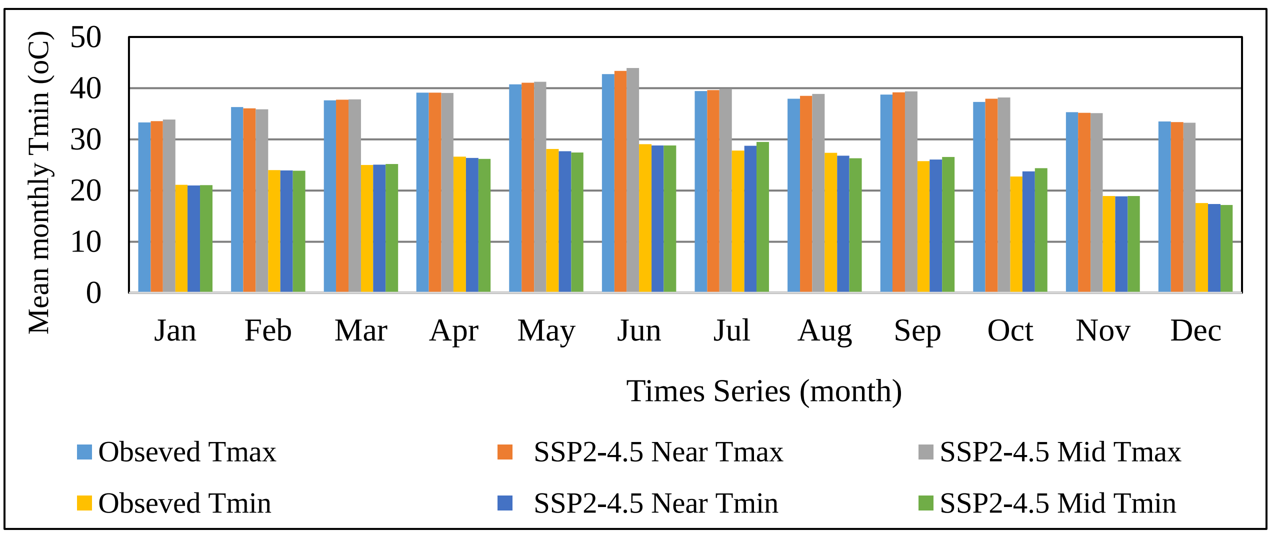

Figure 4.10: Mean monthly maximum and minimum temperatures for near and mid-future periods with respect to baseline period under SSP2-4.5 scenarios

Simulation results consistently indicate an increasing trend in mean annual temperatures for both maximum and minimum values in the near and midterms, with a faster rate of increase projected toward the century's end. It is also observed that the rate of change for maximum temperature exceeds that of minimum temperature, as depicted in Figure 4.10. The mean increase in maximum temperature during the wet season varies between 0.21°C and 0.33°C, whereas the increase during the dry season ranges from 0.24°C to 0.42°C in the near and midterms under SSP2-4.5 scenarios. Conversely, the mean increase in minimum temperature during the wet season shows slight variation, ranging from 0.08°C to 0.21°C, while the mean decrease in minimum temperature during the dry season ranges from 0.06°C to 0.03°C in the near and midterms under SSP2-4.5 scenarios. The simulated maximum temperature is higher in the dry season during the midterm, and the highest increase in minimum temperature is projected for the wet season of the midterm in the watershed. Although the mean annual maximum and minimum temperatures indicate increasing trends in all future periods under SSP2-4.5 scenarios, the mean monthly simulated maximum and minimum temperatures show inconsistent changes across all months from the near to midterm future periods under SSP2-4.5 scenarios, as illustrated in Figure 4.11.

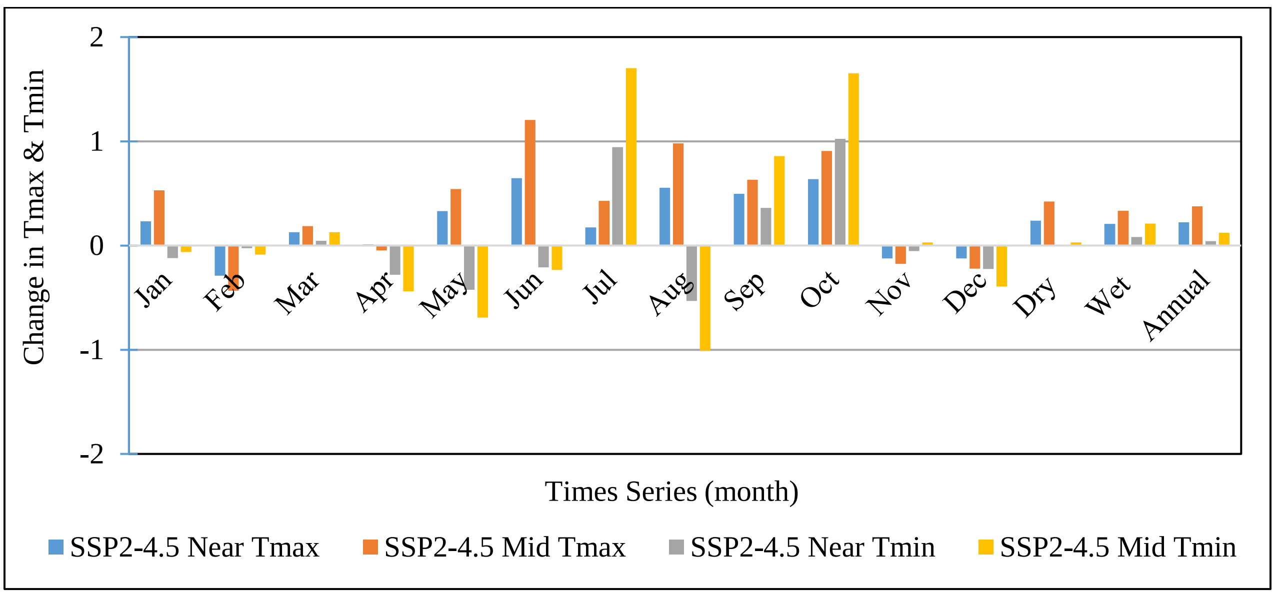

Figure 4.11: Mean monthly and seasonal changes in maximum and minimum temperatures (°C) for near and mid-term from the baseline period under SSP2-4.5 scenarios.

The mean monthly maximum temperature under the SSP2-4.5 scenario is projected to increase by 0.01°C to 0.65°C, with the largest increase occurring in June. In contrast, a decrease in maximum temperature ranging from 0.12°C to 0.29°C is expected in November and October during the near term relative to the baseline. The minimum temperature under SSP2-4.5 is projected to increase by 0.04°C to 1.02°C, with the highest increase in October, while a decrease from 0.12°C to 0.53°C is anticipated in August during the near term compared to the baseline.

In the midterm, the mean monthly maximum temperature could rise by 0.19°C to 1.20°C, with the most significant increase in June, while a decrease of 0.05°C to 0.43°C may occur, with the maximum decrease in February compared to the baseline. Minimum temperatures in the midterm under SSP2-4.5 are expected to increase by 0.03°C to 1.70°C, with the maximum increase in July, while a decrease ranging from 0.06°C to -1.01°C is projected for August compared to the baseline period.

4.6.2.2. Projected Maximum and Minimum Temperature under SSP5-8.5

Under the SSP5-8.5 scenario, the mean annual maximum temperature is projected to increase by 0.21°C to 0.45°C, while the minimum temperature is expected to rise by 0.05°C to 0.22°C in both the near and midterms compared to the baseline. During the dry season, the mean seasonal maximum temperature is projected to increase by 0.20°C to 0.50°C, while the minimum temperature may increase by 0.01°C to 0.05°C under SSP5-8.5 for the near and midterms, respectively (Figure 4.12).

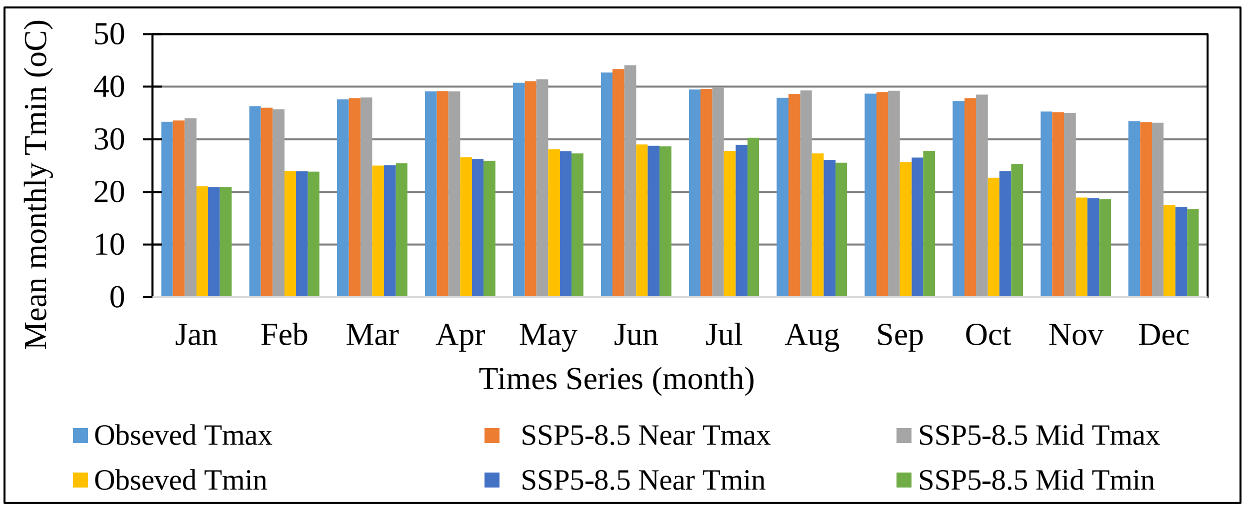

Figure 4.12: Mean monthly Maximum and minimum temperatures for near and mid-future periods with respect to baseline period under SSP5-8.5 scenarios

Similarly, the projected mean seasonal maximum temperature during wet seasons shows an increasing trend, with increases ranging from 0.21°C to 0.41°C. The minimum temperature is projected to rise by 0.08°C to 0.40°C under SSP5-8.5 in both the near-term and mid-term compared to the baseline period. The increase in maximum temperature is more significant during the dry season in the midterm, whereas the increase in minimum temperature is more notable during the wet season under SSP5-8.5.

The projected mean monthly maximum temperature under SSP5-8.5 indicates a larger increase, ranging from 0.02°C to 0.72°C, with the highest increase occurring in August. In contrast, the maximum temperature is expected to decrease by 0.17°C to 0.31°C, with the largest decrease observed in February during the near term. At the same time, the minimum temperature is projected to increase by 0.08°C to 1.23°C under SSP5-8.5, with the highest rise in October, while a decrease of 0.06°C to 1.22°C is expected in August during the near-term relative to the baseline period. In the midterm, the mean monthly maximum temperature may rise by 0.35°C to 1.38°C, with the greatest increase in August, while a decrease of 0.04°C to 0.61°C is projected for February compared to the baseline period (Figure 4.13).

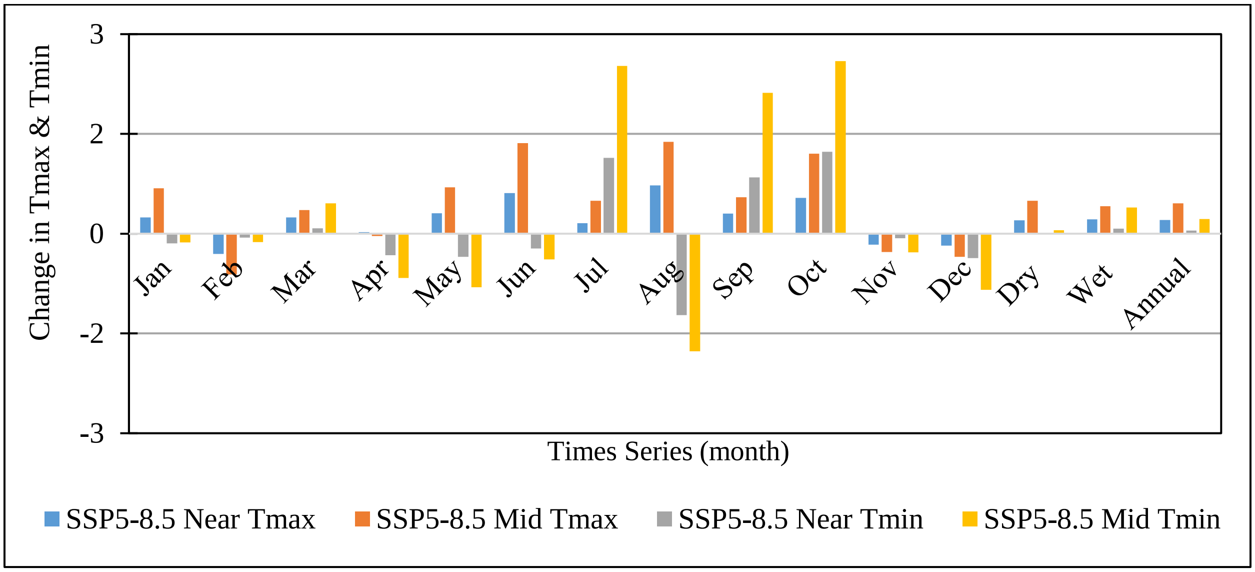

Figure 4.13: Mean monthly and seasonal changes in maximum and minimum temperatures (°C) for near and mid-term from the baseline period under SSP5-8.5 scenarios.

In the midterm under SSP5-8.5, the minimum temperature may increase by 0.46°C to 2.59°C, with the largest rise occurring in October, whereas a decrease of 0.13°C to 1.77°C is expected in August compared to the baseline period.

The projected increase in mean annual maximum and minimum temperatures under the SSP5-8.5 scenario is significantly greater than under SSP2-4.5, reflecting the impact of high CO2 emissions. This trend is corroborated by various studies across Ethiopia, indicating a consistent rise in temperatures, particularly towards the century's end. The SSP5-8.5 scenario predicts higher temperature increases due to elevated greenhouse gas emissions, while SSP2-4.5 represents a medium emission scenario (Almazroui et al., 2021). Similarly, the projected temperature increases under SSP5-8.5 are significantly higher than those under SSP2-4.5, with maximum temperatures expected to rise by 3.39 °C compared to 2.01 °C by 2080 (Asnake et al., 2021). This trend poses severe implications for climate adaptation strategies in regions like the Upper Awash Basin, where rising temperatures and declining precipitation could exacerbate water scarcity and agricultural stress (Birhanu et al., 2021). The findings from the Omo River Basin corroborate these projections, indicating a consistent upward trend in temperatures, which reinforces the urgency for adaptive measures (Ayalew et al., 2021). The high-emission scenario of SSP5-8.5 necessitates more aggressive climate policies compared to SSP2-4.5, as the latter may still allow for some mitigation of adverse effects (Kassaye et al., 2021). Regional studies highlight the critical need for immediate action to address these projected increases, particularly in food security and water resources management (Mohamed & El-Mahdy, 2021). Conversely, some studies suggest that adaptation strategies could still be effective if implemented promptly, potentially mitigating the worst impacts of climate change. Furthermore, the increase in maximum and minimum temperatures may lead to higher evapotranspiration and water stress in the sub-basin. This finding suggests that the rising temperatures under future scenarios may adversely impact the streamflow in the study area. A similar result was reported by Tadese et al. (2020), indicating that the combined effect of rising temperatures and decreasing precipitation will negatively affect runoff and available water resources.

4.7. Climate Trend Analysis for the Historical and Future Periods

The precipitation and temperature trends for the Mille watershed were analyzed using 32 years of data from three stations (Mille, Bati, and Mersa). The Mann-Kendall (MK) test and Sen’s Slope estimator were employed to determine temperature and precipitation trends. The MK trend test identifies statistically significant increasing or decreasing trends in long-term temporal data.

4.7.1. Precipitation trend analysis for the historical and future periods

Historical Precipitation trend analysis

A trend is considered decreasing if the Z value is negative and the computed probability is greater than the significance level, and increasing if the Z value is positive and the probability is greater than the significance level. If the computed probability is less than the significance level, it indicates no trend. The annual precipitation trends for different stations over the last 32 years are shown in Table 4.10. The negative Z and S statistics indicate a declining trend in annual precipitation. Sen's slope summarizes the magnitude of change per unit of time for the detected trend. Two of the three stations, Mille and Mersa stations showed a statistically non-significant decreasing and increasing trend, respectively, there is no trend at the 5% significant level. From the three stations, the annual precipitation showed increasing trends for Bati stations with test statistic (Z=0.89) and respective Sen's slope of (S=0.063), the positive value indicates an increasing trend but is not statistically significant at a 5% level of significance, since the p-value (0.796) is greater than the significant level 0.05.

On a seasonal basis, for Mille station from those three stations, the precipitation trends for the spring and summer seasons were not statistically significant, showing minor increases, with Z and S values of (0.34 and 0.008) for spring and (0.68 and 0.022) for summer. However, the trends for the autumn and winter seasons were not statistically significant, showing minor decreases, with Z and S values of (-0.58 and -0.009) for autumn and (-1.80 and -0.018) for winter. Even though these trends were positive and negative, they were not significant at the 5% level, as the calculated Z values were below 1.96.

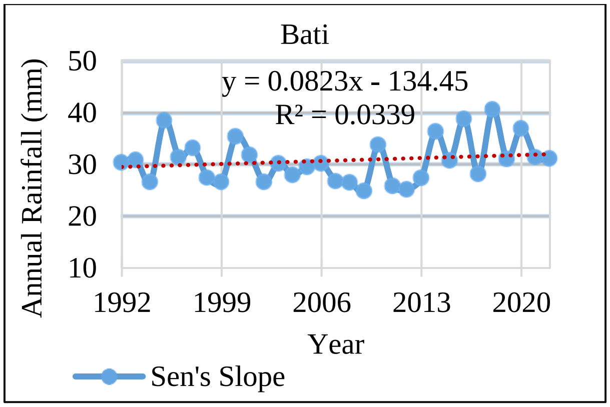

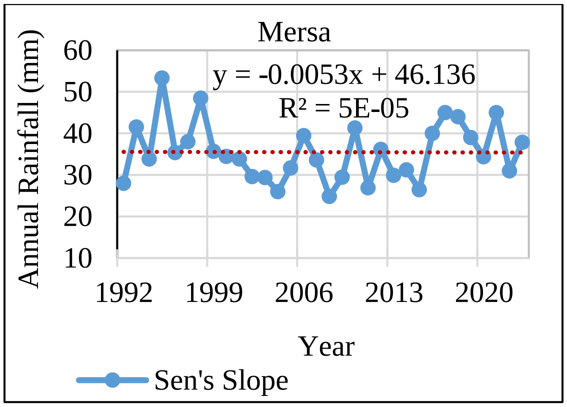

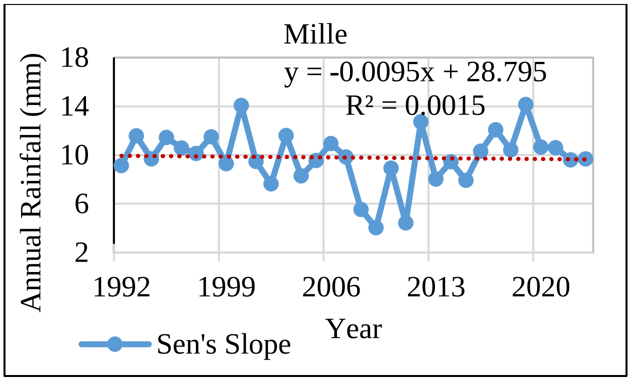

Figure 4.14: Historical annual precipitation trend analysis for each station

Monthly precipitation variations were calculated for each station using the Mann-Kendall test, and Sen's slope estimator determined the magnitude of the slope. Significant changes were observed in monthly rainfall data, with some months showing increasing (upward) trends and others showing decreasing (downward) trends. The monthly MK test showed significant decreasing trends in the Mille station for January, with (Z = -2.52 and S = -0.011), and Bati station in January, with (Z = -2.01 and S = -0.029). Similarly, the Mersa station in November with (Z = -2.01 and S = -0.029) and the month Bati station (June and August) with (Z = 2.19, 2.06 and S = 0.030, 0.073) shows significant increasing monotonic trend respectively.

Table 4.10: Historical annual precipitation trend analysis for the baseline period

Stations	Min.	Max.	Mean	STDV.	P-vale	Sen's slope	Z-value
Bati	23.8	985.49	504.65	21.58	0.987	0.063	0.89
Mersa	34.96	1135.38	585.17	30.23	0.56	0.02	0.05
Mille	6.49	313.37	159.93	6.02	0.75	-0.005	-0.05
Mean	21.75	811.42	416.58	19.28	0.489	0.026	0.297

STDV-standard deviation

Future Precipitation Trend Analysis

The results of the Mann-Kendall (MK) trend test show no significant trend in annual precipitation for the near-term (2025-2055) period under both SSP2-4.5 and SSP5-8.5 scenarios. The calculated Z (-1.076, -1.333) and Sen's slope (-3.274, -1.796) values for both respective scenarios indicate an insignificant decrease in precipitation. Although there is a decreasing trend in precipitation, it is not statistically significant since the Z value is less than 1.96, indicating that the trend is not statistically significant at the 5% significance level. Similarly, there is no significant trend in annual precipitation under SSP2-4.5 in the mid-term (2056-2085) period, since the calculated p-value is greater than the level of significance (0.05). However, in the mid-term (2056-2085) period under the SSP5-8.5 scenario, a positive significant trend is observed. The calculated Z (2.753) and Sen's slope (6.404) values indicate that the annual precipitation may significantly increase under SSP5-8.5 in the mid-term period (as shown in Table 4.12). Meanwhile, under SSP2-4.5, a slight increase in precipitation is expected, but this is not statistically significant since the Z value is less than 1.96.

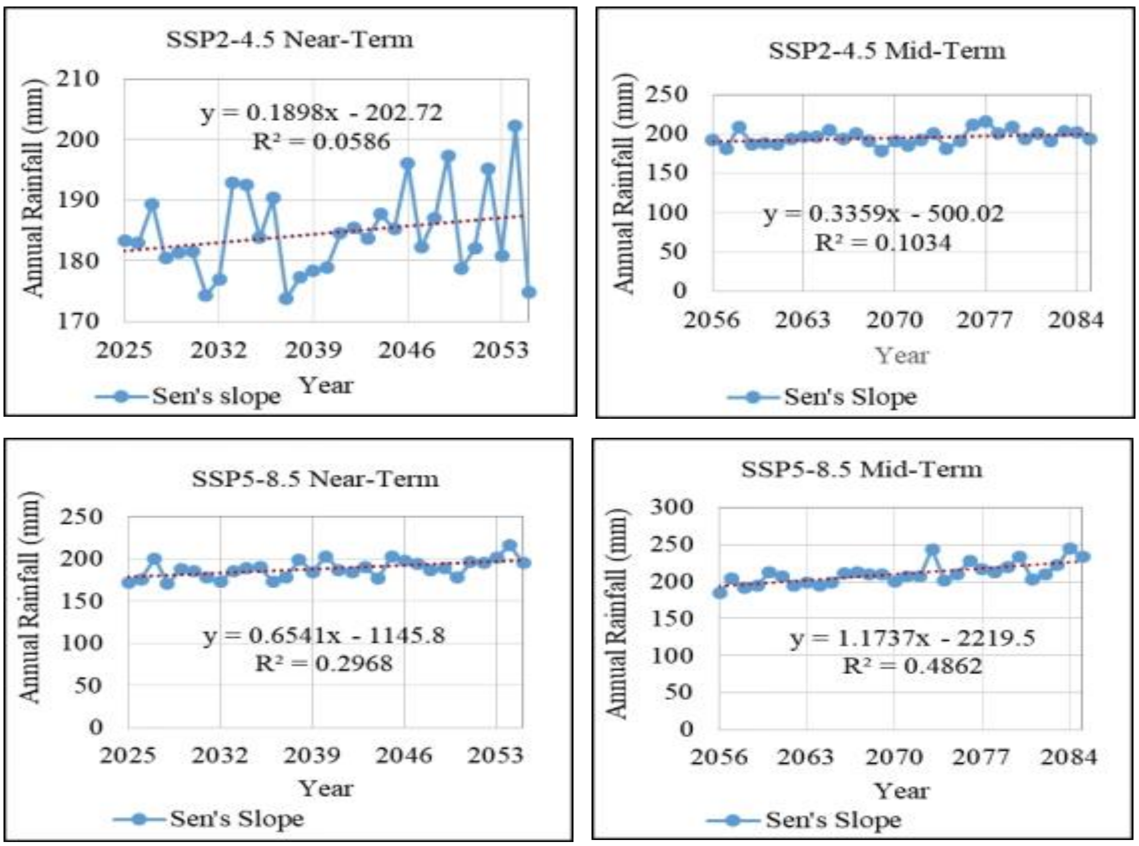

Figure 4.15: Future annual trend analysis of precipitation in the near-term and mid-term period under SSP2-4.5 and SSP5-8.5

The seasonal trend analysis shows a significant decrease in summer precipitation during the nearterm period under SSP2-4.5, with Z and Sen's slope values of -2.140 and -3.113, respectively. On the other hand, in the mid-term period, precipitation shows a positive significant trend in both spring (Z = 1.976, Sen's slope = 1.238) and summer (Z = 2.197, Sen's slope = 2.250). Similarly, precipitation is expected to increase significantly in September (Z = 2.680, Sen's slope = 0.917) during the mid-term period under SSP2-4.5 (as shown in Table 4.5). Under SSP5-8.5, the seasonal precipitation trends for the near-term period do not exhibit significant trends in most months, but a near-significant upward trend is observed in February (Z = 1.796, Sen's slope = 0.246). For the mid-term period, precipitation increases significantly in spring (Z = 3.342, Sen's slope = 0.248) and in September (Z = 2.753, Sen's slope = 1.181), indicating a potential increase in precipitation during these seasons, as shown in table (4.11).

Table 4.11: Trend analysis of future precipitation under SSP2-4.5

SSP2-4.5 Near-term					SSP2-4.5 Mid-term			
Series	P-value	Sens's slope	Z	trend	P-value	Sens's slope	Z	trend
Jan	0.133	0.08	1.473	no	1	0.004	0.017	no
Feb	0.066	0.246	1.796	no	1	0.002	0.017	no
Mar	0.568	-0.239	-0.606	no	0.916	0.06	0.121	no
Apr	0.779	-0.106	-0.284	no	0.216	-0.461	-1.229	no
May	0.231	0.45	1.264	no	0.321	0.259	0.988	no
Jun	0.953	-0.02	-0.069	no	0.126	0.26	1.507	no
Jul	0.009	-2.019	-2.511	Downward	0.238	1.077	1.195	no
Aug	0.103	-1.089	-1.61	no	0.125	1.078	1.493	no
Sep	0.201	-0.454	-1.284	no	0.008	0.917	2.68	Upward
Oct	0.678	-0.07	-0.416	no	0.641	0.131	0.506	no
Nov	0.205	0.102	1.238	no	0.621	-0.068	-0.502	no
Dec	0.039	-0.12	-2.115	Downward	0.049	-0.235	-1.962	Downward
Spring	0.596	-0.243	-0.537	no	0.043	1.238	1.976	Upward
Summer	0.029	-3.113	-2.14	Downward	0.024	2.25	2.197	Upward
Winter	0.534	0.154	0.651	no	0.359	0.5	0.912	no
Annual	0.288	-3.274	-1.076	no	0.234	3.431	1.229	no

Monthly trend analysis using the Mann-Kendall method shows that some months exhibit increasing (upward) trends, while others show decreasing (downward) trends. For example, in the near-term period under SSP2-4.5, significant decreasing trends are observed in July (Z = -2.511, Sen's slope = -2.019) and December (Z = -2.115, Sen's slope = -0.120) (Table 4.5). In the mid-term period under SSP2-4.5, monthly precipitation increases significantly in September (Z = 2.680, Sen's slope = 0.917) but decreases in December (Z = -1.962, Sen's slope = -0.235). Similarly, under SSP5-8.5, a significant increase is observed in September (Z = 2.753, Sen's slope

= 1.181) in the mid-term period, while in the near-term period, February shows a near-significant upward trend (Z = 1.796, Sen's slope = 0.246).

The analysis indicates that while no significant trends are observed in annual precipitation for the near-term period under both SSP scenarios, a significant increase in precipitation is expected in the mid-term period, especially under the SSP5-8.5 scenario. Seasonal analysis shows a significant downward trend in summer precipitation under SSP2-4.5 in the near-term period, but both spring and summer seasons exhibit significant positive trends in the mid-term period under both scenarios. Additionally, certain months, such as July and December, show decreasing trends in the near-term period, while September shows significant increasing trends in the mid-term period. These findings highlight potential future changes in precipitation patterns, especially under higher emission scenarios such as SSP5-8.5.

Table 4.12: Trend analysis of future precipitation under SSP5-8.5

SSP5-8.5 Near-term					SSP5-8.5 Mid-term			
Series	P-value	Sens's slope	Z	trend	P-value	Sens's slope	Z	trend
Jan	0.058	0.172	1.853	no	0.972	-0.013	-0.052	no
Feb	0.009	0.661	2.511	Upward	0.916	-0.041	-0.121	no
Mar	0.671	-0.253	-0.433	no	0.832	-0.178	-0.225	no
Apr	0.572	0.343	0.571	no	0.777	0.152	0.294	no
May	0.049	0.878	1.922	no	0.126	0.534	1.507	no
Jun	0.272	-0.219	-1.091	no	0.155	0.287	1.403	no
Jul	0.166	-1.426	-1.368	no	0.228	1.249	1.195	no
Aug	0.135	-1.021	-1.472	no	0.86	0.211	0.19	no
Sep	0.063	-0.476	-1.818	no	0.004	1.181	2.753	Upward
Oct	0.479	-0.144	-0.71	no	0.101	0.641	1.61	no
Nov	0.75	0.072	0.329	no	0.832	0.079	0.225	no
Dec	0.436	-0.062	-0.779	no	0.126	0.357	1.507	no
Spring	0.126	-0.67	-1.507	no	0	0.248	3.342	Upward
Summer	0.058	-2.522	-1.853	no	0.201	1.629	1.264	no
Winter	0.087	0.615	1.68	no	0.621	0.74	0.502	no
Annual	0.177	-1.796	-1.333	no	0.004	6.404	2.753	Upward

4.7.2. Temperature Trend Analysis for the historical and future periods

Historical Temperature Trend Analysis

The time series of maximum and minimum monthly temperatures were analyzed for the sub-basins using the same methods as the precipitation data. The mean annual temperature for the last 32 years is presented in Table 4.13. The mean annual Tmax during 1992-2023 was 38.73°C, with the highest recorded value being 54.07°C in 2019 and the lowest 21.50°C in 2015. The mean annual Tmin during the same period was 17.0°C, with the highest at 38.5°C (2018) and the lowest at 13.3°C (2017), as shown in Table 4.13. The Mann-Kendall (MK) trend test demonstrated a sharp, statistically significant increase in mean maximum temperatures (Z = 3.64), with a p-value below the 0.05 significance level. The annual maximum temperature increased significantly at several stations, including Bati, Mersa, and Mille. The Bati station exhibited a Z-value of 1.4 and a Sen's slope of 0.013, while the Mersa station showed a Z-value of 0.1 and a Sen's slope of 0.042. In contrast, the Mille station did not show a statistically significant trend for maximum and minimum temperatures, as its p-value exceeded the significance threshold. Additionally, seasonal trends indicated a significant increase in maximum temperatures across all seasons for the Mersa station. The Bati station also demonstrated increasing trends during the winter season. Minimum temperatures significantly increased at Bati and Mersa stations throughout all seasons, while the Mille station showed an increase in maximum temperature but was not statistically significant. Overall, the mean annual minimum temperature displayed a positive Z-value of 1.44, indicating a non-significant trend. Nonetheless, the minimum temperature for the Bati station showed a significant decreasing trend, with a p-value below 0.05 (0.001) and a negative Sen's slope of -0.088. In the remaining stations, increasing trends were observed but were not statistically significant.

Table 4.13: Historical Mean annual (maximum and minimum) temperature trend analysis

		Min.	Max.	Mean	STDV	P-value	Sen's slope	Z-value
Station	Variable							
Bati	Tmax	26.61	29.22	27.91	0.08	0.02	0.013	1.4
	Tmin	7.92	16.29	12.1	0.17	0.0012	-0.088	-0.95
Mersa	Tmax	27.38	30.62	29	0.09	0	0.042	0.1
	Tmin	9.94	14.46	12.2	0.12	0.0398	0.007	0.14

Mille	Tmax	35.74	38.73	37.24	0.11	0.5602	0.012	1.23
	Tmin	21.03	26.31	23.67	0.16	0.0028	-0.022	-0.76
Mean Annual	Tmax	29.91	32.86	31.38	0.09	0.19277	0.022	0.91
	Tmin	12.96	19.02	15.99	0.15	0.0146	-0.034	-0.523

The baseline monthly temperature trend analysis was conducted for each station within the study area. The results indicate that the mean monthly maximum temperature significantly increased at Bati station in March, and at Mersa station in March and July, all at a significance level of 0.01. At Mille station, the maximum temperature showed an increase but was not statistically significant. The mean monthly minimum temperature also shows an increasing trend at Bati station in April, July, September, October, and November; at Mersa station in July, August, and September; and at Mille station in April and November. The highest slope magnitude was recorded at Bati station in November (S = 0.138, Z = 3.45), statistically significant at 0.05. Conversely, the monthly minimum temperature significantly decreased at Bati station in all months except January, May, November, and December. In a related study, Gedefaw et al. (2021) observed an upward trend in mean annual and seasonal temperature over the Ethiopian highlands under SSP scenarios. Alemayehu et al. (2020) also reported increasing trends in both maximum and minimum temperatures in various eco-regions of Ethiopia under SSP2-4.5 and SSP5-8.5 scenarios. These findings underscore the necessity for adaptive management strategies in response to the rising temperature trends impacting agricultural practices and water resources management in the Mille River Watershed.

Future Temperature Trend Analysis

The result of the Mann-Kendall trend test shows that both annual maximum and minimum temperatures are expected to increase significantly in the future under both scenarios. The maximum and minimum temperature-increasing trend is found to be statistically significant as the computed p-value is less than the significance level alpha ≤ 0.05, one should reject the null hypothesis (Ho). For maximum temperature, the calculated Z-value is (5.44, 2.72) and (6.33, 6.54) in the near-term (2025-2055) and mid-term (2056-2085) periods under SSP2-4.5 and SSP5-8.5, respectively. Similarly, for minimum temperature, the computed Z-value is (4.47, 2.23) and (5.40, 4.54) under SSP2-4.5 and SSP5-8.5, respectively. This indicates that a significant increasing trend may be expected in the future since the calculated Z-value is greater than 1.96 for all scenarios.

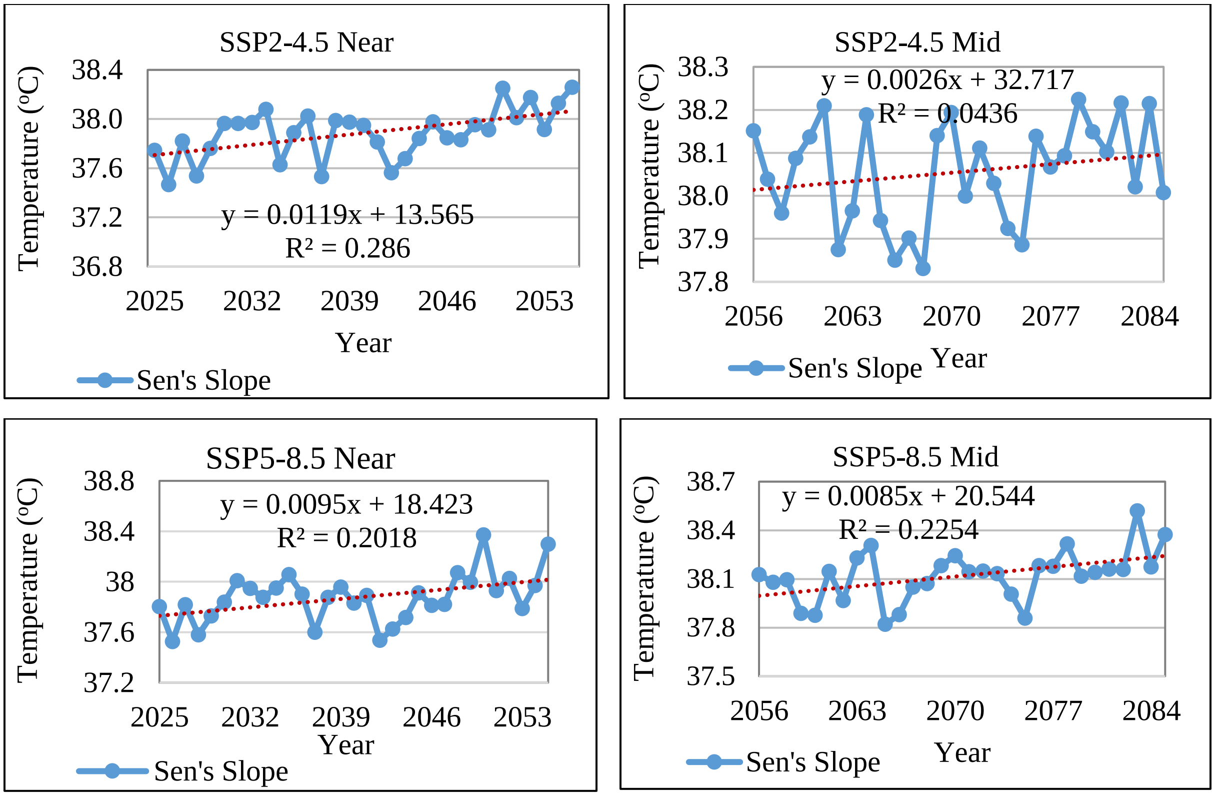

Figure 4.16: Future annual trend analysis of maximum temperature in near and midterm periods under SSP2-4.5 and SSP5-8.5

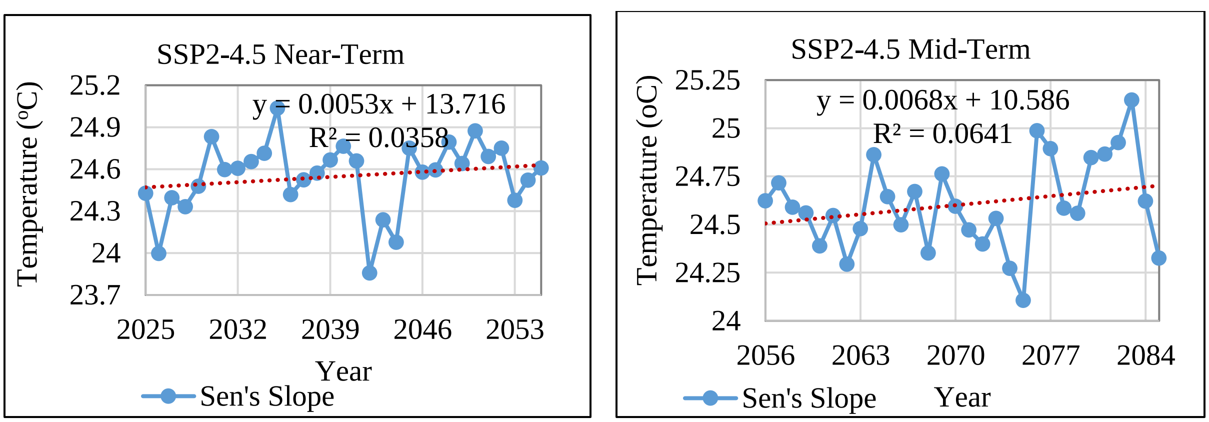

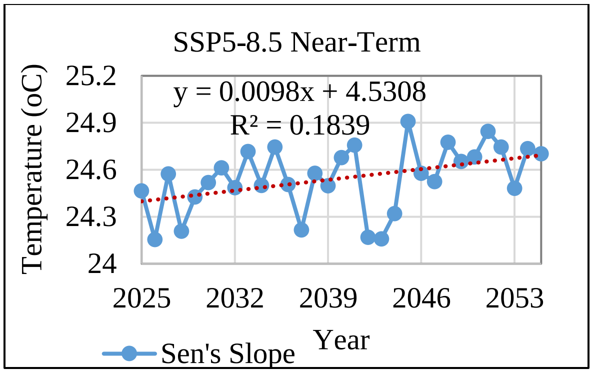

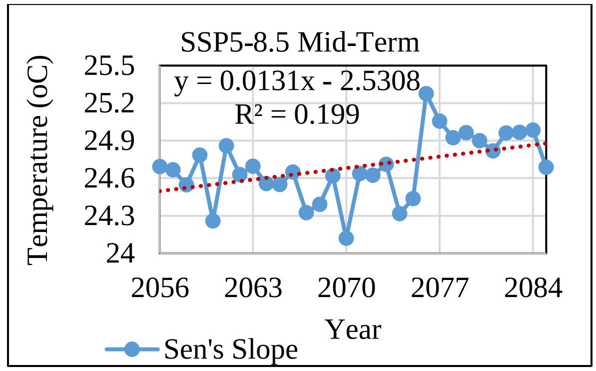

Figure 4.17: Future annual trend analysis of minimum temperature in near and midterm periods under SSP2-4.5 and SSP5-8.5

In the same manner, the seasonal Mann-Kendall trend test of temperature shows a significant trend for future periods. Accordingly, the maximum temperature shows a significant increasing trend in the near-term period in all seasons except spring, which shows a decreasing trend, and significantly increased in the winter and summer and decreased in the spring season of the mid-term period under SSP2-4.5. The minimum temperature also increased significantly in the near-term period in summer and spring, and in the mid-term period, an increasingly significant trend is expected in the winter and spring under SSP2-4.5, whereas in the mid-term period, the minimum temperature is expected to decrease significantly in the summer season. Similarly, under SSP5-8.5, the maximum temperature is expected to increase significantly in the summer and spring in the near-term period at the level of significance, since the calculated p-value is less than 0.05. Similarly, in the mid-term period, the maximum temperature may increase in all seasons (winter, spring, and summer), whereas the minimum temperature is expected to increase significantly in the summer season of the near-term period and in the winter and spring seasons of the mid-term period. The magnitude of change is higher in spring for both maximum and minimum temperatures (S=0.144, 0.124), respectively. On the other hand, the monthly maximum temperature is significantly increased in January, February, April, July, October, November, and December in the 2025-2055s, and April, May, June, and July in the 2056-2085s under SSP2-4.5. Similarly, the minimum temperature shows an increasing trend in January, April, October, November, and December under the same scenario. Under SSP5-8.5, the maximum temperature shows a significant increasing trend in the 2025-2055s from January to May as well as from October to December, and the minimum temperature in January, September, October, November, and December at the level of significance. Additionally, in the 2056-2085s, a significant trend was observed for maximum temperature from

April to December, except for October, and for minimum temperature from April to August. The related study by different scholars showed that both minimum and maximum temperatures are expected to rise in the future under SSP2-4.5 and SSP5-8.5 emission scenarios. The finding of Gedefaw et al. (2018) also showed that the temperature of the Awash River Basin may significantly increase in the future.

4.8. Calibration and Validation of SWAT Model

4.8.1. Sensitivity analysis

Sensitivity analysis was conducted on SWAT flow parameters at a monthly time step to determine the most sensitive parameters using a global sensitivity analysis approach in SWAT-CUP at the Mille gauging station. All flow parameters were analyzed to identify the most sensitive ones in the Mille watershed. In this analysis, 22 flow parameters potentially affecting streamflow were considered, and 10 parameters were found to have a significant influence on controlling the streamflow in the watershed (Table 4.14). The most sensitive parameters included Maximum Canopy Storage (CANMX), SCS Runoff Curve Number (CN2), Threshold depth of water (mm); R_REVAPMN.gw, Manning "n" value for overland flow; R_OV_N.hru, Saturated Hydraulic Conductivity (SOL_K), and Soil Evaporation Compensation Factor (ESCO). A study by (Tufa and Sarma, 2021) identified (CN2) and (SOL_K) as the most sensitive parameters for runoff estimation in the Genale watershed. Similarly, (Samuel, 2016) identified (CN2) and (CANMX) as highly sensitive parameters in the Upper Awash Basin.

Figure 4.18: Result of sensitivity analysis for flow parameters on SWAT-CUP (SUFI-2)

Table 4.14: Sensitive Flow Parameters, their rank and fitted value

Parameter Name	Sensitivity Rank	t-Stat	P-Value	Min Value	Max Value	Fitted Value
R__CN2.mgt	1	-12.6	0	-0.18	1.7	-0.12
R_OV_N.hru	2	10	0	-0.2	0.08	0.02
R__SOL_K (.).sol	3	6.78	0	-0.09	0.21	0.2
R__SOL_AWC (.).sol	4	6.7	0	-0.1	0.23	-0.01
V__CH_K2.rte	5	-3.92	0.02	30.18	85.08	75.61
V_REVAPMN.gw	6	2.1	0.03	0	500	48.3
V__GWQMN.gw	7	1.43	0.67	0.83	2.4	1.6
V__GW_DELAY.gw	8	-1.69	0.09	52.19	67.1	61.84
V__ALPHA_BANK.rte	9	-1.29	0.77	0.65	0.86	0.81
V__CANMX.hru	10	1.3	0	0	20.5	2.7

Note: "A" denotes adding the fitted value to the existing value, "V" signifies replacing the existing value with the fitted value, and "R" indicates multiplying the existing value by (1 + the fitted value).

4.8.2. Calibration and Validation of SWAT Model

The calibration results for monthly flow demonstrate a good agreement between the measured and simulated average monthly flows, with a Nash-Sutcliffe Simulation Efficiency (NSE) of 0.73 and a coefficient of determination (R^2) of 0.80, as presented in (Table 4.15) and (Figure 4.19). Similarly, (Dagnenet et al., 2018) reported a correlation coefficient ($R^2 = 0.80$) and Nash-Sutcliffe Simulation Efficiency (NSE = 0.70), indicating very good agreement between observed and simulated flows in the Upper Blue Nile River Basin during the calibration period. Hence, the SWAT model can be considered a reliable tool for simulating streamflow under various Ethiopian watershed conditions after calibration. For the study area, the measured and simulated average monthly flows during the calibration period were 9.31 m^3/s and 9.41 m^3/s, respectively, showing that the simulated streamflow slightly overestimated the observed flow. The linear regression of the scatter plot comparing observed and simulated streamflow during calibration is illustrated in (Figure 4.21).

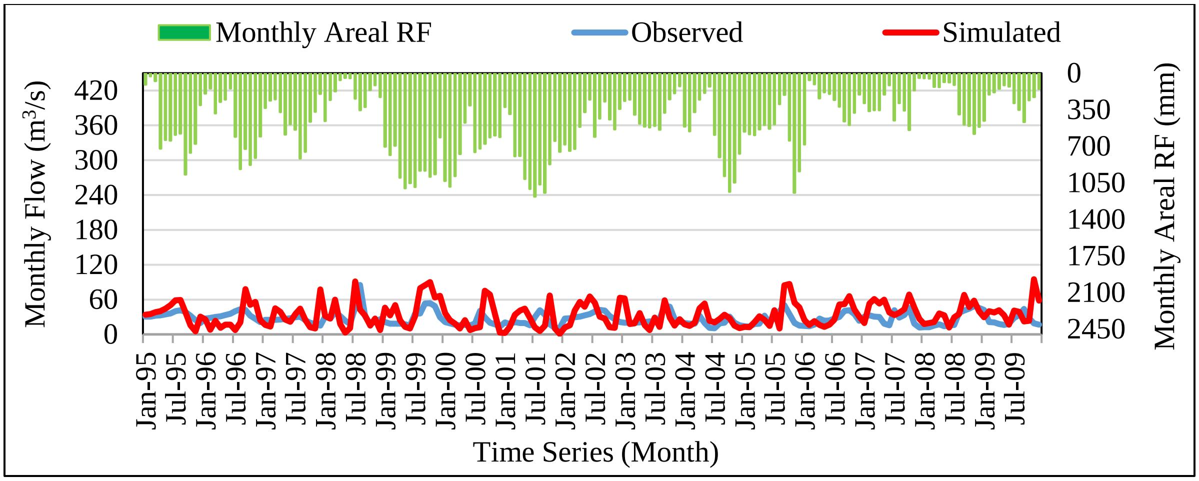

Figure 4.19: Calibration result for average monthly streamflow (1995–2009)

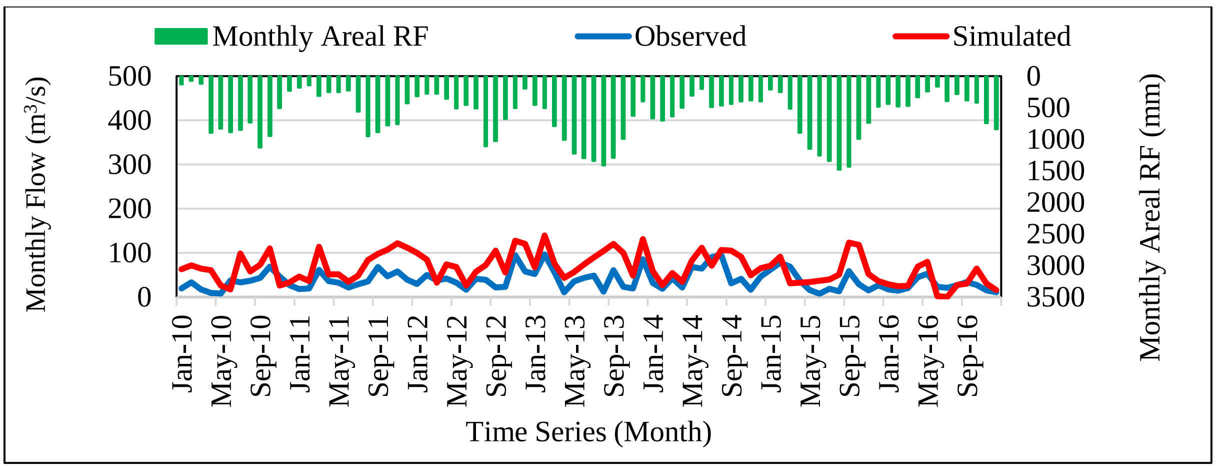

Figure 4.20: Validation result for average monthly streamflow (2010–2016).

Validation verifies the model's performance for simulating flows in periods outside the calibration period without any further parameter adjustments. The validation was conducted over seven years (2010–2016), as shown in (Figure 4.20). The coefficient of determination ($R^2 = 0.83$) and Nash-Sutcliffe Simulation Efficiency (NSE = 0.77) indicate acceptable accuracy for predicting watershed responses. These results confirm that the model performs well during validation and is capable of simulating streamflow in the study area (Table 4.15).

Wakjira et al., (2020) similarly observed good agreement between monthly measured and simulated data during the validation period, with ENS = 0.76 and $R^2 = 0.81$, for the Fincha'a Watershed. The linear regression of the scatter plot comparing observed and simulated streamflow for validation is shown in (Figure 4.22).

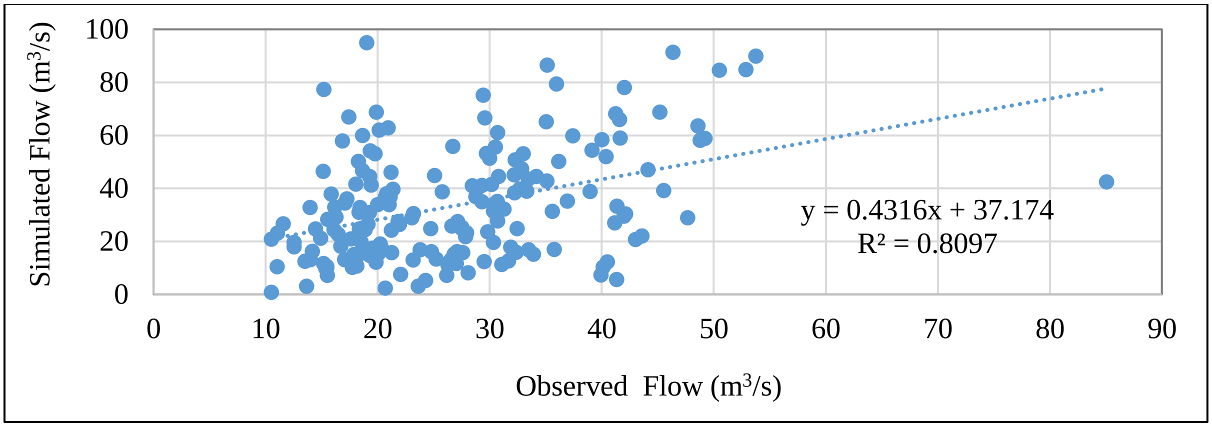

Figure 4.21: Scatter plot of observed and simulated streamflow for calibration (1995–2009)

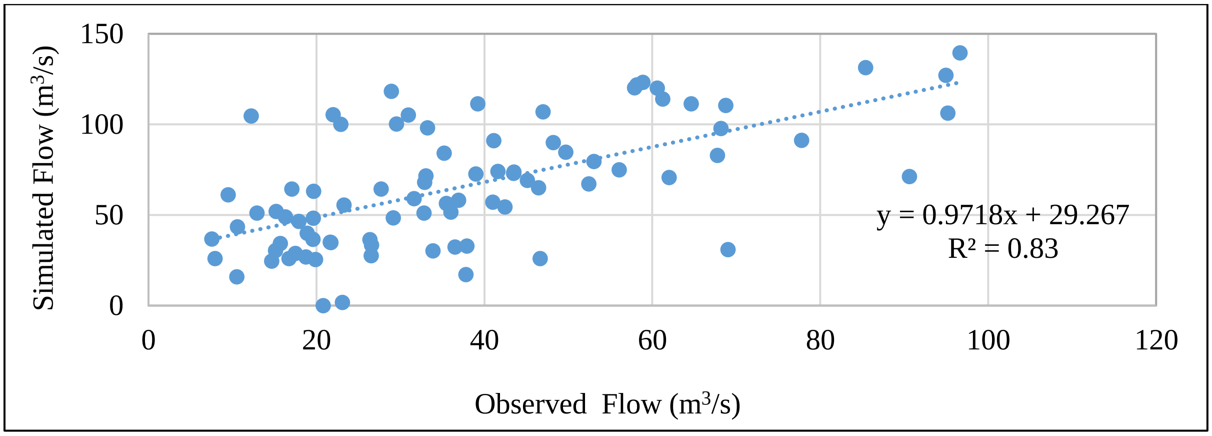

Figure 4.22: Scatter plot of observed and simulated streamflow for validation (2010–2016).

Table 4.15: Model Performance Evaluation Statistics for Calibration and Validation

	Model Performance Evaluation Criteria	
Periods	Calibration (1995–2009)	Validation (2010–2016)
R^2	0.8	0.83
NSE	0.73	0.77
% PBIAS	16.1	11.2

4.9. Independent and Combined effect of Climate and LULC changes on R-R

4.9.1. Past LULC Change Impact on Rainfall-Runoff

One of the most important parts of the study was to assess the impact of past LULC changes on the streamflow of the Mille watershed as summarized in Table 4.16. The assessment of streamflow was done in terms of annual, seasonal, and monthly basis at the outlet of the watershed.

Table 4.16: Mean Annual and Seasonal Changes of R-R results for past LULC change

	Past LULC changes			Change detection m^3/s			(%) change of flow		
Years of study	2000	2010	2020	S1	S2	S3	S1	S2	S3
Annual	574	577	581	2.6	4.6	7.24	0.5	0.8	1.26
Wet season	577	581	577	4.5	6.4	10.9	1.1	1.6	2.68
Dry season	411	417	411	-1.9	-1.8	-3.7	-1.1	-1.1	-2.2

Note: S1 Scenarios (2000–2010), S2 Scenarios (2010–2020), S3 Scenarios (2000–2020)

The simulated mean annual streamflow exhibited a higher increase in the second scenario (4.64 m^3/s, 0.80%) than the first scenario (2.6 m^3/s, 0.45%). Unfortunately, the streamflow will be lower in the first scenario compared to the second scenario due to the gradual increase of grass/range land starting from 2000 to 2010. The continued increase of agricultural and settlement lands and extraction of forest cover and woodland will further increase the mean annual flow with a magnitude of 7.24 m^3/s (1.26%) throughout the study period from 2000 to 2020. Seasonal changes of streamflow were assessed for the wet (March, April, May, August, September, October, and November) and dry (January, February, June, July, and December) seasons. As indicated in Table 4.12 above, the mean wet season flow increased by 4.47 m^3/s (1.1%) and 6.41 m^3/s (1.56%) for the first and second scenarios, respectively. This is because rainfall satisfies soil moisture deficits more quickly in agricultural and settlement areas than in forests, thereby generating more flow. Conversely, the reduction of vegetation cover and the increase of agriculture and settlement reduced the dry season flow by 1.87 m^3/s (1.11%) and 1.78 m^3/s (1.07%) for the first and second scenarios, respectively.

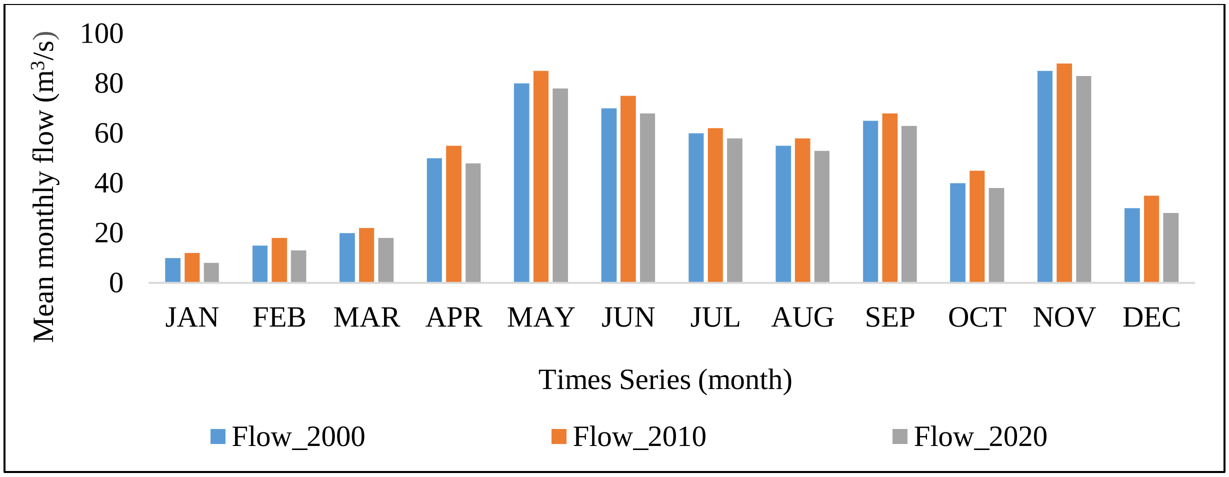

Figure 4.23: Mean Monthly Streamflow Results for the Past Three LULC Scenarios

Mean monthly streamflow depicted a higher increase in the 2020 LULC compared to 2010 and 2000. This was attributed to the increase in agricultural and settlement areas and the reduction of forest, scrub/bushland, grass/range land, and woodland cover in the watershed. As a result of expansions in agricultural land, rainfall infiltration into the soil decreased, and soil moisture deficits were more rapidly satisfied under agricultural land than forests, thereby producing more runoff. Consequently, more flow was created in the 2010 LULC than in the 2000 LULC.

During the study period from 2000 to 2020, mean monthly streamflow increased by 10.88 m^3/s for the wet season as a result of agricultural and settlement land expansion by 132.76% and 511.88%, respectively, and the decrease of other LULC types. These results are in agreement with several studies. For instance, Temesgan et al. (2018) interpreted that annual streamflow increased by 300.6 mm, 304.5 mm, and 307.3 mm for 1985, 2000, and 2015 LULC, respectively, associated with the expansion of cultivated land and built-up areas and the reduction of forest, shrub land, and grassland in the Andassa watershed, Blue Nile Basin, Ethiopia. Similarly, Moges et al. (2019) showed that increases in streamflow can be directly attributed to the expansion of cultivated lands at the expense of forested vegetation. Mesfin (2018) reported that the expansion of settlement and agricultural land resulted in mean monthly streamflow increases of 5.97 m^3/s and 0.96 m^3/s during the wet and dry seasons, respectively, in the Shaya watershed of the Genale Dawa Basin. Asmamaw (2013) reported that the increase in cultivated land and the decline in forest and shrubland resulted in increased wet-season flows, while dry-season flows decreased.

4.9.2. Future LULC Change Impact on Rainfall-Runoff Patterns

This section focuses on analyzing the impact of future LULC changes on the Mille watershed's streamflow response. Simulated streamflow due to future LULC changes was compared with past LULC changes to estimate the effects of these changes on stream flow. Table 4.17: Mean Annual and Seasonal Changes of Streamflow Results for Future LULC Change

Table 4.17: Mean Annual and Seasonal Changes of R-Runoff results for future LULC change

	Future LULC Changes			Change detection m^3/s			(%) change of flow		
Years of study	2020	2030	2050	S1	S2	S3	S1	S2	S3
Annual	581.14	584.88	588.07	3.74	3.19	6.98	0.66	0.55	1.19
Wet season	416.98	423.1	429.08	6.12	5.98	12.1	1.47	1.41	2.9
Dry season	164.15	161.79	158.99	-2.36	-2.8	-5.16	-1.44	-1.73	-3.14

Note: S1 scenarios (2030 - 2020), S2 scenarios (2050 - 2030), S3 scenarios (2020 - 2050)

Streamflow showed a slight increase in the first scenario by 3.74 m^3/s (0.64%) compared to the second scenario, 3.19 m^3/s (0.55%). Overall, streamflow increased throughout the future study period, with a magnitude of 6.93 m^3/s (1.19%). This increase was driven by the continued expansion of agricultural and settlement areas and the extraction of vegetation cover.

During the wet season, mean monthly streamflow increased by 6.12 m^3/s (1.47%) and 5.98 m^3/s (1.41%) for the first and second scenarios, respectively. Conversely, mean monthly streamflow decreased during the dry season by 2.36 m^3/s (1.44%) and 2.8 m^3/s (1.73%) for the first and second scenarios, respectively. In general, future LULC changes increased mean monthly streamflow by 12.1 m^3/s (2.9%) during the wet season from 2020 to 2050, primarily due to the expansion of agricultural and settlement lands by 44.02% and 69.20%, respectively. On the other hand, mean monthly streamflow showed a decreasing trend during the dry season, with a magnitude of 5.16 m^3/s (3.14%), reflecting a reduction in base flow caused by intensive agricultural and settlement expansion.

Streamflow contributions were higher during the wet months due to surface runoff, while during the dry months, the contributions were from groundwater. Wet season flows were less sensitive to LULC changes than dry season flows due to reduced groundwater contributions during the dry season, caused by less infiltration as a result of decreased vegetation cover. The rate of streamflow increase was higher for past LULC changes compared to future LULC changes, mainly due to the expansion of woodland and grass/range land, coupled with increases in agricultural and settlement areas.

These findings align with other studies, such as Temesgen (2018), which revealed that annual and wet season flows, surface runoff, and water yield increased, while dry season flows, groundwater flows, lateral flows, and ET decreased between 1985 and 2015 due to LULC changes in the Upper Blue Nile Basin. Rajib and Merwade (2017) also observed a 0.5%–3.5% increase in average annual streamflow at a basin outlet during 2081–2100 under future LULC scenarios. Conversion of cropland, forest, or grassland to perennial hay/pasture areas would lower surface runoff by 25%, while persistent forest cover in the northern region would cause up to a 7% increase in evapotranspiration.

4.9.3. Impact of Climate Change on Rainfall-Runoff Patterns

The impact of climate change was analyzed by comparing baseline simulated streamflow with two future flows in the near and midterm periods. The simulated mean annual streamflow is projected to increase by 7.63% and 5.76% from baseline flow in the near term under SSP2-4.5 and SSP5-8.5 scenarios, respectively. For the midterm, mean annual streamflow is expected to increase by 8.25% and 6.07%, respectively, from the baseline flow under SSP2-4.5 and SSP5-8.5 scenarios.

Table 4.18: Mean annual and seasonal change of flow under SSP2-4.5 and SSP5-8.5 scenarios for climate change only from the baseline period

	Simulated Streamflow in (m^3/s)				% Change of Stream Flow			
Scenarios	SSP2-4.5		SSP5-8.5		SSP2-4.5		SSP5-8.5	
Period	Near-term	Mid-term	Near-term	Mid-term	Near-term	Mid-term	Near-term	Mid-term
Annual	625.5	629.1	614.6	616.4	7.6	8.3	5.8	6.1
Wet season	452.3	456	443	447.1	8.5	9.4	6.2	7.2
Dry season	173.1	173	171.7	169.3	5.5	5.4	4.6	3.2

The seasonal variation of projected streamflow from the baseline period was computed for the wet (March to May and August to November) and dry (January, February, June, July, and December) seasons. Understanding future changes in streamflow for wet and dry seasons is crucial for assessing the hydrological impacts of climate change.

The wet season mean streamflow of the watershed is expected to increase by 8.48% and 6.23% from the baseline flow in the near term under SSP2-4.5 and SSP5-8.5 scenarios, respectively. For the midterm, the wet season streamflow may increase by 9.36% and 7.21% under SSP2-4.5 and SSP5-8.5 scenarios, respectively. The dry season mean streamflow is projected to increase by 5.46% and 4.57% in the near term under SSP2-4.5 and SSP5-8.5 scenarios, respectively, while for the midterm, increases of 5.41% and 3.16% are expected under SSP2-4.5 and SSP5-8.5 scenarios.

The mean monthly percentage change in streamflow for the near and midterm under SSP2-4.5 and SSP5-8.5 scenarios from the baseline is presented in Figure 4.25. The mean monthly streamflow is expected to increase for all months except February, July, August, and September, which show decreases in the near and midterms under SSP2-4.5 and SSP5-8.5 scenarios.

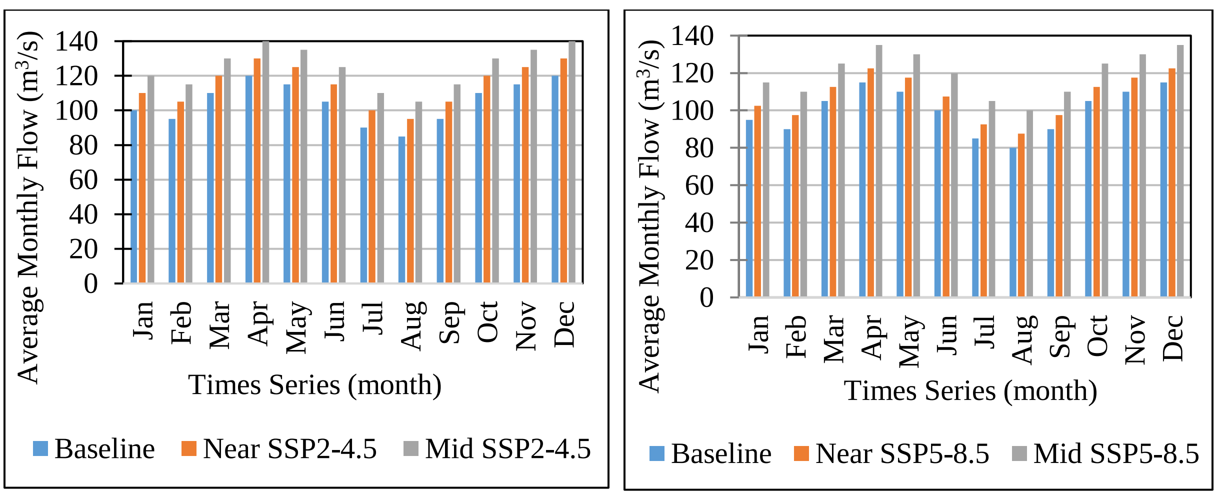

Figure 4.24: Mean monthly flow for near and midterm under SSP2-4.5 and SSP5-8.5 scenarios from the baseline period.

The maximum increase in mean monthly streamflow is expected in May, with increases of 45.4 m³/s (45.4%) and 54.9 m³/s (54.9%) in the near- and mid-term, respectively, while a significant decline is projected in September, with decreases of 69.1 m³/s (69.1%) and 126.1 m³/s (126.1%) for the near- and mid-term under SSP2-4.5.

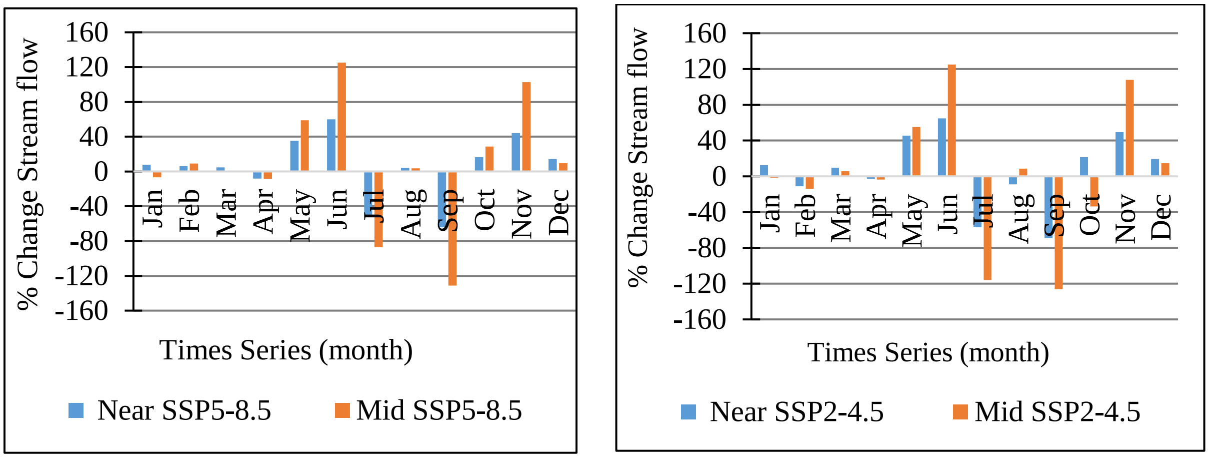

Figure 4.25: Percentage change of flow for near and midterm future under SSP2-4.5 and SSP5-8.5 scenarios compared to the baseline period.

Under SSP5-8.5 scenarios, the highest increase in mean monthly streamflow occurs in May, with increases of 35.4 m³/s (35.4%) and 58.9 m³/s (58.9%) for the near- and mid-term, respectively. The maximum reduction occurs in September, with decreases of 64.1 m³/s (64.1%) and 131.1 m³/s (131.1%) in the near- and mid-term. High-flow months like June and November show significant increases under both SSP2-4.5 and SSP5-8.5 scenarios, with increases of 124.9% (Mid SSP2-4.5) and 107.6% (Mid SSP2-4.5), respectively. Overall, the annual, seasonal, and monthly streamflow is expected to increase in some months but decrease in others under both SSP2-4.5 and SSP5-8.5 scenarios. The highest reductions are observed during low-flow months like September, while high-flow months like May are projected to experience significant increases in streamflow.

The projected increase in streamflow aligns with studies by (Tufa and Sarma, 2021), which reported a consistent increase in mean annual streamflow due to changes in rainfall and temperature in the Genale watershed. Similarly, (Tesfaye et al., 2019) noted increases in annual, seasonal, and monthly flow volume for the period 2018 to 2077, corresponding to increases in precipitation for the Awata River watershed in the Genale Dawa Basin. Anwar et al., (2016) also projected increases in mean annual streamflow for the Upper Gilgel Abay Watershed under future scenarios. Therefore, fluctuations in mean streamflow, especially during the annual, wet, and dry months, due to climate change in the Afar Highlands, will not only affect the livelihood of people in the mille Zone but also impact all inhabitants downstream who depend on the flow of the Mille

River. These findings indicate that climate change will influence streamflow variability, significantly impacting the livelihoods of downstream communities dependent on the River.

4.9.4. Combined Impact of Climate and LULC Change on Rainfall-Runoff Patterns

To evaluate the combined impacts of climate and LULC changes on streamflow, four simulations were conducted using two future LULC scenarios (2030 for the near term and 2050 for the midterm) combined with SSP2-4.5 and SSP5-8.5 scenarios. The combined impacts were simulated using the calibrated SWAT model, with results presented in Table 4.19.

Table 4.19: Mean Annual and Seasonal change of flow under SSP2-4.5 and SSP5-8.5 scenarios for combined climate and LULC change from the baseline period

	Streamflow (m^3/s)				% Change of Stream Flow			
Scenario	SSP2-4.5		SSP5-8.5		SSP2-4.5		SSP5-8.5	
Period	Near-term	Mid-term	Near-term	Mid-term	Near-term	Mid-term	Near-term	Mid-term
Annual	628	633	618	621	8	9	6	7
Wet Season	453	452	444	443	9	8.4	7	6
Dry Season	175	181	174	177	7	10	6	8

Note: Near-term (2025–2055) and midterm (2056–2085).

In the midterm, mean annual streamflow is projected to increase by 8.96% and 6.77% under SSP2-4.5 and SSP5-8.5 scenarios, respectively, from baseline flow. The changes in streamflow due to combined climate and LULC impacts align with the trends observed for climate change alone. However, under SSP5-8.5 in the midterm, higher temperatures and increased evapotranspiration led to slightly lower streamflow than SSP2-4.5, despite higher rainfall.

If LULC changes are held constant, higher evaporation rates due to warming are likely to affect streamflow in Ethiopia and the broader East African region, impacting regional economies. Streamflow sensitivity to temperature changes is expected to outweigh the impacts of rainfall and LULC changes for the midterm in the Mille watershed.

The seasonal variation of streamflow for the projected climate parameter change from the baseline period was computed for wet and dry seasons (Table 4.19). The mean wet season streamflow may increase by 8.72% and 6.46%, while the dry season flow may increase by 6.62% and 5.76% from the baseline period for the near-term under SSP2-4.5 and SSP5-8.5 scenarios, respectively. For the midterm, the mean wet season flow will increase by 8.39% and 6.25%, while the dry season flow is expected to increase by 8.07% and 10.42% from the baseline period under SSP2-4.5 and SSP5-8.5 scenarios, respectively. The combination of LULC and climate change scenarios will have an additive effect on streamflow simulation. Simulation results showed that, if all other variables are held constant, an increase in river flow may be expected in the future due to climate and LULC changes. Impacts associated with these changes should be effectively planned for and mitigated. Hence, mean wet and dry season streamflow may increase for the coming century under both SSP scenarios from the baseline period.

Mean monthly change of streamflow indicates there may be an increase during the months of (January, March, April, May, June, October, November, and December), while a decrease is observed for the months of (February, July, August, and September) under both SSP scenarios from the baseline period for the near and midterm, respectively, as shown in (Figure 4.26).

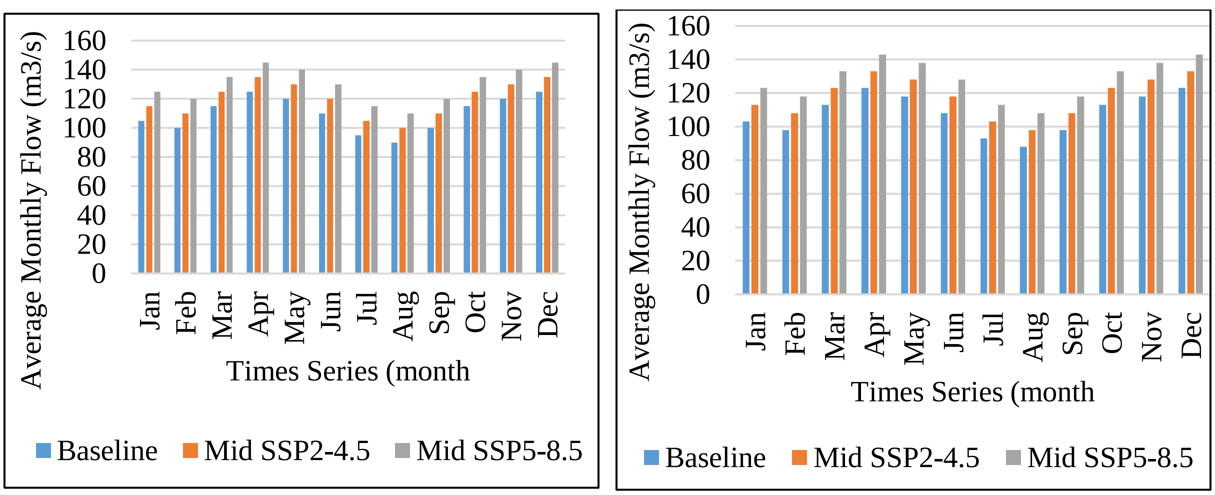

Figure 4.26: Mean monthly streamflow for near and midterm under SSP2-4.5 and SSP5-8.5 scenarios compared to the baseline period.

The maximum mean monthly flow increment was observed in May by 35.39 m³/s (39.4%) and 31.77 m³/s (35.36%), while the minimum increment occurred in December and March by 5.87 m³/s (15.81%) and 2.3 m³/s (11%) for the near-term under SSP2-4.5 and SSP5-8.5, respectively, from the baseline period. Mean monthly flow showed a maximum reduction in August by 28.66 m³/s (63.9%) and 27.12 m³/s (60.46%), whereas the minimum reduction occurred in February by

1.53 m³/s (12.3%) and 2.3 m³/s (18.45%) for the near-term under SSP2-4.5 and SSP5-8.5, respectively.

The largest percentage change in mean monthly flow increment was observed in June by 34.39 m³/s (38.28%) and 31.27 m³/s (34.80%), while the smallest nominal increment occurred in August by 4.19 m³/s (20.09%) and 2.3 m³/s (11.03%) during the midterm under SSP2-4.5 and SSP5-8.5, respectively (Figure 4.27).

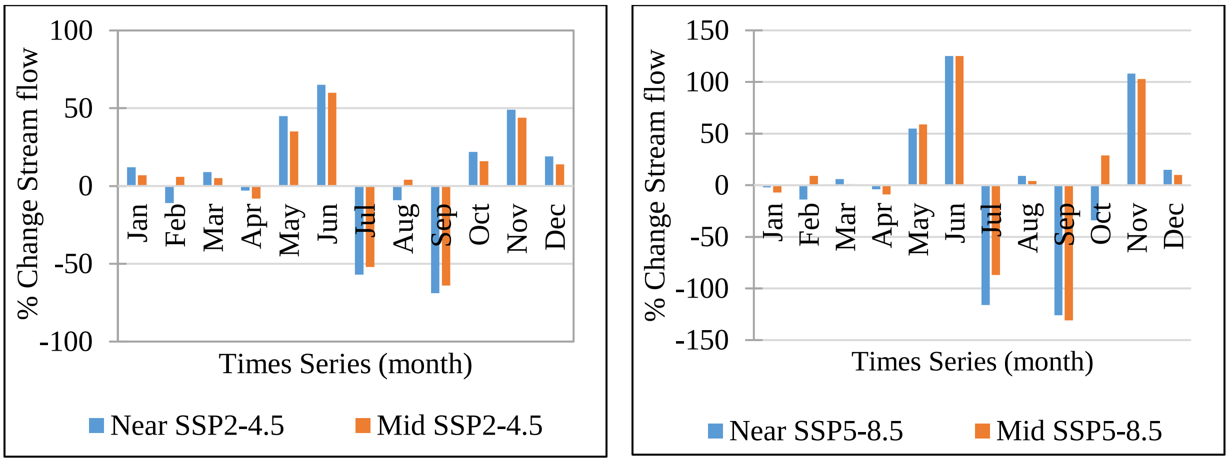

Figure 4.27: Percentage change in flow for near-term and mid-term under SSP2-4.5 and SSP5-8.5 scenarios compared to the baseline period.

Simulated mean monthly streamflow showed a significant decline in August by 27.7 m³/s (61.76%) and 27.12 m³/s (60.46%), whereas the minimum reduction occurred in February by 0.6 m³/s (4.82%) and 1.3 m³/s (10.42%) during the midterm under SSP2-4.5 and SSP5-8.5, respectively. Comparing the impacts of climate change and LULC change on streamflow, it is evident that climate change had a dominant impact, increasing streamflow compared to the baseline period. Streamflow is more sensitive to climate change than to changes in LULC. Consequently, the changes in streamflow under future conditions of climate and LULC change are remarkably consistent with those in scenarios where only future climate changes, while LULC played a secondary role. Changes in future LULC produced small variations in streamflow, while combined scenarios predicted larger changes in streamflow than those considering only LULC or climate change from the baseline period. Results indicate that combined climate and LULC changes have a more noticeable effect on streamflow compared to the baseline period, with a gradual increase in streamflow observed in the future.

The results of this study align with other regional and local climate change impact assessments. For example, Birhan et al. (2021) observed increasing trends in streamflow related to temperature and precipitation increases in the Lake Tana Basin, Upper Blue Nile River Basin, by the end of the 21st century. Similarly, a study in the Kesem sub-basin of the Awash River Basin showed an increase in mean annual streamflow by 14.5% and 19.1% for SSP2-4.5 and by 4.7% and 6.9% for SSP5-8.5 scenarios, parallel to rainfall and temperature increases from the 2050s to the 2080 period (Negash et al., 2020). Dagnenet et al. (2018) reported a precipitation increase of up to 25% in the Upper Blue Nile River Basin, leading to projected streamflow and lateral flow increases of up to 12.85% (9.9%), 28.5% (20.03%), and 26.4% (29.12%) under LULC, climate, and combined scenarios, respectively. Similarly, Babur et al. (2016) found an increase in mean annual flow under SSP2-4.5 and SSP5-8.5 scenarios for 2011–2040, 2041–2070, and 2071–2100 in Pakistan. Thus, soil and water conservation activities should be adopted, and water harvesting structures should be properly designed and implemented to compensate for flow fluctuations in the Mille River. Additionally, larger increments in streamflow from baseline scenarios may cause flooding in floodplain zones. Considering and implementing integrated water resources management is crucial to address the increasing water demand due to the high population growth rate.

5. SUMMARY, CONCLUSIONS AND RECOMMENDATION

5.1. Summary and Conclusions

This study focused on analyzing the impacts of climate change and land use/land cover (LULC) changes on the hydrology of the Mille River Watershed in the Lower Awash River Basin, Ethiopia. Using the SWAT model for hydrological simulations, the CA-Markov model for predicting LULC changes, and SDSM for downscaling climate data, the research assessed both historical trends and future projections of LULC and climate data. The study found a significant increase in agricultural land, rising from 6.11% in 2000 to 20.47% in 2020, while forest cover decreased from 7.45% to 6.35% during the same period. These trends suggest that agricultural expansion has had a notable impact on surface runoff and groundwater recharge. Future projections for 2030 and 2050 indicate a continuation of these trends, with agricultural areas expected to increase by 4.79% between 2020 and 2050, while forest cover is likely to decrease further after a temporary rise by 2030. The climate change projections under SSP2-4.5 and SSP5-8.5 scenarios predict a rise in temperatures by 0.65°C and 1.05°C by 2050, respectively, along with a 15% increase in precipitation. This shift is expected to intensify flood risks and water scarcity in the region. The hydrological impact simulations using the SWAT model revealed a significant increase in streamflow due to the combined effects of climate and LULC changes. The model projections indicated that streamflow could rise by 7.63% under the SSP2-4.5 scenario and 8.13% under the SSP5-8.5 scenario, which could result in more frequent flooding events while reducing water availability during dry periods. The SWAT model was calibrated and validated successfully, showing reliable performance with NSE values of 0.78 and 0.75, and R^2 values of 0.82 and 0.79. Based on these findings, the study concludes that sustainable land use management, including reforestation, afforestation, and controlled urban expansion, is crucial to mitigate the adverse impacts on hydrology. Additionally, adopting climate change adaptation strategies such as improving water storage, flood control systems, and water-efficient irrigation techniques is essential for managing the challenges of extreme weather events. Integrated watershed management, which considers both LULC and climate change, is necessary to enhance the region's resilience. Furthermore, policymakers should incorporate climate projections and LULC data into water resource planning and develop climate-resilient infrastructure. Future research should explore socio-economic factors, refine hydrological modeling, and improve data resolution for better predictions. This study provides a foundation for future research and actionable recommendations to improve watershed management and safeguard water resources in the Mille River Watershed.

5.2. Recommendation

This study highlights the significant impacts of climate change and land use/land cover (LULC) changes on the hydrology of the Mille River Watershed in Ethiopia. Several key recommendations are proposed to ensure sustainable water management in the region.

Firstly, Integrated Water Resources Management (IWRM) should be adopted to balance social, economic, and environmental needs while engaging stakeholders in addressing increasing water demand and flood risks. Climate adaptation strategies are essential and should include land-use planning, the development of climate-resilient infrastructure (such as flood control systems and reservoirs), agro-ecological practices, soil conservation, and rainwater harvesting. These measures will help mitigate streamflow variability and reduce the adverse impacts of runoff.

Promoting sustainable land-use practices, such as forest restoration, conservation agriculture, and the development of green infrastructure, can help reduce surface runoff, improve water quality, and protect ecosystems. Additionally, designing and implementing water harvesting structures and soil conservation measures will regulate flow fluctuations and enhance water availability for irrigation and other uses.

Long-term monitoring systems are also crucial. Establishing real-time tracking of hydrological variables, coupled with advanced climate modeling (e.g., CMIP6), will improve the reliability of future projections. Future research should focus on the effects of LULC changes, population growth, and water use efficiency on hydrology, with an emphasis on integrated water and land management strategies in the Lower Awash Basin. Strengthening local governance and fostering regional cooperation is critical to enhancing resilience to climate and LULC changes, ensuring sustainable water resource management.

The following specific recommendations are drawn from the study's findings:

- Effective water management strategies should align with future rainfall trends, addressing the temporal shifts in peak rainfall and their direct impact on the Mille River Watershed. Soil and water conservation measures should be implemented, and water harvesting structures must be designed and applied to mitigate flow fluctuations.
- Water plays a vital role in both small- and large-scale irrigation. Therefore, mitigating the adverse impacts of climate change and LULC changes is crucial. This study emphasizes the

importance of helping communities adapt to changing climatic conditions and reduce the associated negative impacts.

- Future research should expand on additional factors influencing hydrology, such as LULC changes alone, population growth, and water use efficiency, particularly in the Lower Awash River sub-basin. Utilizing outputs from GCMs of CMIP6 will improve the reliability of climate projections.
- Given the increasing streamflow trends, IWRM practices should be adopted to meet the growing water demand driven by population growth and address potential flooding in floodplain areas.

By implementing these recommendations, communities and policymakers can effectively manage water resources and reduce the risks associated with climate and LULC changes in the Mille River Watershed.

6. REFERENCES

Abbaspour, K.C. (2020). SWAT-CUP 2012: SWAT calibration and uncertainty programs–A user manual.Duebendorf, Switzerland: Eawag.

Adamu, A. (2013). Assessing the Impacts of Land Use and Cover Change on Hydrology of Watershed the Case Study on Gilgel Abbay Watershed, Lake Tana Basin, Ethiopia.

Adane Mezgebu and Getachew Workineh, 2017. Changes and drivers of afro-alpine forest ecosystem: future trajectories and management strategies in the Bale eco-region, Ethiopia. *Ecological Processes*, 6(1), pp. 1-13.

Alemayehu, A., Shawul, Sumedha, Chakma, 2020. Suitability of global precipitation estimates for hydrologic prediction in the main watersheds of Upper Awash Basin. *Environmental Earth Sciences*, 10.1007/S12665-019-8801-3.

Alemu, A. (2011). Evaluation of Climate Change Impact on Extreme Hydrological Event, Case Study: Addis Ababa and Surrounding Watershed. Msc. Thesis. Addis Ababa: Addis Ababa Institute of Technology.

Alemu, G., & Woldeyes, T. (2023). Land use and water resources dynamics in the Fetam watershed: A SWAT model approach. *Environmental Management*, 68(3), 512–528. https://doi.org/10.1007/s13201-023-01914-5

Anand, J., Gosain, A. K., Khosa, R. (2018). Prediction of land use changes based on Land Change Modeler and attribution of changes in the water balance of Ganga basin to land use change using the SWAT model Science of the Total Environment, 644, 503-519.

Anwar, A., Seifu, A., Essayas, K., Abeyou, W., Tewodros T., Shimelis, B., and Assefa, M., 2016. Climate change impact on streamflow in the upper Gilgel Abay Watershed, Blue Nile Basin, Ethiopia. In *Landscape Dynamics, Soils and Hydrological Processes in Varied Climates* (pp. 645-673). Springer, Cham.

Aragaw, H. M., Goel, M. K., & Mishra, S. K. (2021). Hydrological responses to human-induced land use/land cover changes in the Gidabo River basin, Ethio. HYDROLOGICAL JOURNAL, 66(4), 17. https://doi.org/DOI:10.1080/02626667.2021.1890328

Arnold, J.G., Srinivasan, R., Muttiah, R.S., & Williams, J.R. (2012). SWAT: Model use, calibration, and validation. *Transactions of the ASABE, 55*(4), 1491–1508. DOI: 10.13031/2013.42256.

Asamen, Birara, Asnake, Melkamu, Teshome, Ayana, Adane, A., Awass, Demelash, Wondimagegnehu, Goshime, 2021. Transformation of climate and its sway on hydro-climatology using representative concentration pathways (RCP) in Geba watershed of Ethiopia. *Modeling Earth Systems and Environment*, 10.1007/S40808-020-01029-9.

Ashenafi, Yimam, Kassaye, Guangcheng, Shao, Xiaojun, Wang, Eshetu, Shifaw, Shiqing, Wu, 2021. Impact of climate change on the staple food crops yield in Ethiopia: implications for food security. *Theoretical and Applied Climatology*, 10.1007/S00704-021-03635-8.

Asmamaw Adamu, (2013). Assessing the impacts of Land use land cover change on the hydrology of watershed: a case study on Gigel-Abbay Watershed, Lake Tana Basin, Ethiopia (Doctoral dissertation).

Associated Press (AP News). (2024). *Climate change and rapid urbanization worsened the impact of East African rains, scientists say.* Retrieved from https://apnews.com.

Azari, M., Moradi, H. R., Saghafian, B., & Faramarzi, M. (2016). Climate change impacts on Streamflow and sediment yield in the North of Iran. Hydrological Sciences Journal, 61(1), 123–133. https://doi.org/10.1080/02626667.2014.967695

Ba, W., Du, P., Liu, T., Bao, A., Luo, M., Hassan, M., and Qin, C., 2018. Simulating hydrological responses to climate change using dynamic and statistical downscaling methods: a case study in the Kaidu River Basin, Xinjiang, China. *Journal of Arid Land*, 10(6), pp. 905-920.

Babur, M., Babel, M.S., Shrestha, S., Kawasaki, A., and Tripathi, N.K., 2016. The Impact of Climate Change on Reservoir Inflows Using Multi Climate-Model under RCPs' Including Extreme Events—A Case of Mangla Dam, Pakistan.

Behailu, Birhanu, Seifu, Kebede, Katrina, Charles, Meron, Teferi, Taye, Ayele, Atlaw, Michael, Birhane, 2021. Impact of natural and anthropogenic stresses on surface and groundwater supply sources of the upper awash sub-basin, central Ethiopia. *Frontiers in Earth Science*, 10.3389/FEART.2021.656726.

Belay, K., Alemayehu, E., & Tesfaye, D. (2022). Impacts of LULC changes on water resources in Ethiopia's Central Rift Valley. *Hydrological Research*, 55(2), 83–99. https://doi.org/10.2166/hr.2022.067

Belete, A., Teshome, W., & Kifle, S. (2023). Impact of climate change on rainfall-runoff processes in the Awash River Basin. *Hydrology Journal*.

Beven, K.J.; (2012). Rainfall Runoff Modelling. The primer.Wiley. 360 p.

Bhasin, S., Sharma, P., & Kaur, A. (2023). *Evaluation of CMIP6 models for simulating climate variables affecting rainfall-runoff processes*. Journal of Climate Studies, 22(1), 50–67.

Bireda Alemayehu, 2015. GIS and remote sensing-based land use/land cover change detection and prediction in Fagita Lekoma Woreda, Awi Zone, and Northwestern Ethiopia. Addis Ababa, Ethiopia: Addis Ababa University.

Birhan Getachew, B.R. Manjunatha, and H.G. Bhat, 2021. Modeling projected impacts of climate and land use/land cover changes on hydrological responses in the Lake Tana Basin, upper Blue Nile River Basin, Ethiopia. *Journal of Hydrology*, 595, p. 125974.

Bjornaes, C., & Ni, E. (2020). A guide to Representative Concentration Pathways.

Burke, M., Hsiang, S. M., & Miguel, E. (2024). Global non-linear effect of temperature on economic production. *Nature Climate Change*, 14(1), 43-50. Retrieved from https://www.nature.com.

Canton, M., Gassman, P.W., & Teshager, A.D. (2015). Comparison of SWAT and SWAT+ for modeling agricultural watersheds in the Upper Mississippi River Basin. *International SWAT Conference Proceedings*.

Chen, C.-N., Tfwala, S. S., & Tsai, C.-H. (2020). Climate Change Impacts on Soil Erosion and Sediment Yield in a Watershed. Water, 12(8), 2247. https://doi.org/10.3390/w12082247

Chen, J., Brissette, F.P., Leconte, R. and Caron, A., 2012. A versatile weather generator for daily precipitation and temperature. *Transactions of the ASABE*, 55(3), pp.895-906.

Climate Extremes. (2021). *Differences between dynamical and statistical downscaling*. Retrieved from Climate Extremes.

Copernicus Climate Change Service. (2021). *Introduction to downscaling methods*. Retrieved from Copernicus Climate.

Cousino, L. K., Becker, R. H., & Zmijewski, K. A. (2020). Modeling the effects of change water, sediment, and nutrient yields from the Maumee River watershed. Hydrology: Regional Studies, 4, 762–775.https://doi.org/10.1016/j.ejrh.2020 .06.017

Daba, M. H., & You, S. (2020). Assessment of climate change impacts on river flow regimes upstream of the awash basin, Ethiopia: Based on IPCC fifth assessment report (ar5 climate change scenarios. Hydrology, 7(4), 1–22 https://doi.org/10.3390/hydrology7040098

Dagnenet Fenta, Z., Duan, T., Rientjes, T., and Markus Disse, 2018. Analysis of combined and isolated effects of land-use and land-cover changes and climate change on the upper Blue

Nile River basin's streamflow. *Hydrology and Earth System Sciences*, 22(12), pp. 6187-6207.

Desalegn, T., Cruz, F., Kindu, M., Turrión, M.B., and Gonzalo, J., 2014. Land-use/land-cover (LULC) change and socioeconomic conditions of local communities in the central highlands of Ethiopia. *International Journal of Sustainable Development & World Ecology*, 21(5), pp. 406-413.

Dessalegn, Worku, Ayalew, Tirusew, Asefa, Mamaru, A., Moges, Sileshie, Mesfin, Leyew, 2021. Evaluating the potential impact of climate change on the hydrology of Ribb Watershed, Blue Nile Basin, Ethiopia. *Journal of Water and Climate Change*, 10.2166/WCC.2021.049.

Desta, M., Mekonnen, A., & Bekele, G. (2023). Effects of LULC changes on streamflow in the Bilate catchment, Ethiopia. *Water Resources Research*, 59(4), 112-130. https://doi.org/10.1080/24749508.2023.2237323

Dibaba, W. T., Demissie, T. A., & Miegel, K. (2020). Watershed Hydrological Response to Combined Land Use/Land Cover and Climate Change in Highland Ethiopia: Fincha'a Catchment. *Water*, *12*(6), 1801. https://doi.org/10.3390/w12061801

Dibaba, W.T., (2016). The effects of land use land cover change hydrological process of Gilgel Gibe, Omo Gibe Basin. International Journal of and Engineering Research, 7, 8.

Dile, Y. T., Berndtsson, R., & Setegn, S. G. (2013). Hydrological Response to Climate for Abay River, in the Lake Tana Basin - Upper Blue Nile Basin of Ethiopia. 8(10), 12–17 https://doi.org/10.1371/journal.pone.0079296

Dyer, E., Washington, R., & Taye, M. T. (2020). Evaluating the CMIP5 ensemble in Ethiopia: Creating a reduced ensemble for rainfall and temperature in Northwest Ethiopia and the Awash Basin. *International Journal of Climatology*, 40(5), 2555-2573.

East African Rainfall. URL https://doi.org/10.1175/JCLI-D-12-00708.1

Emiru, N. C., Molla, M. B., Mengistu, G. M., & Solomon, D (2021). Impact of Climate Change on the Hydrology of the Upper Awash River Basin Ethiopia. Hydrology, 9(1), 3. https://doi.org/10.3390/hydrology9010003

Endris HS, Omondi P, Jain S, Lennard C, Hewitson B, Chang'a L, Nikulin, C GJJO (2013). Assessment of the Performance of CORDEX Regional Climate Models in Simulating

ERDAS Field Guide (2014): User manual of ERDAS IMAGINE.

Eyring, V., Bony, S., Meehl, G.A., Senior, C.A., Stevens, B., Stouffer, R.J., and Taylor, K.E., 2016. Overview of the Coupled Model Intercomparison Project Phase 6 (CMIP6) experimental design and organization. *Geoscientific Model Development*, 9, 1937–1958. https://doi.org/10.5194/gmd-9-1937-2016.

FOWLER, K. J. A., (2016). Simulating runoff under changing climatic conditions addressing a perceived shortcoming in conceptual rainfall-runoff models 52, 1820-1846, Water Resources Research.

Gao., X., Wang, J., & Li, J. (2020). *Assessing the combined impact of climate and land use on hydrologic processes using the SWAT model*. Environmental Hydrology, 31(3), 190–204.

Gassman, P.W., Reyes, M.R., Green, C.H., & Arnold, J.G. (2007). The Soil and Water Assessment Tool: Historical development, applications, and future research directions. *Transactions of the ASABE*, 50(4), 1211-1250.

Gebrechorkos SH, Hülsmann S, Bernhofer C (2019b) statistically downscaled climate for Africa. Sci Data 6(1):31–31, DOI: 10.1038/s41597 -019-0038-1

Gebrehiwot, T., & van der Veen, A. (2013). Climate change vulnerability in Ethiopia: Disaggregation of Tigray Region. *Journal of Eastern African Studies*, 7(4), 607-629.

Gebremedhin, E. T. (2020).Crowdsourcing and interactive modelling for urban flood management. Journal Risk Management, 13(2), 1-15 [e12602]. https://doi.org/10.1111/jfr3.12602

Gebrie, M. J. (2016). Evaluation of Land Use Land Cover Change on Stream Flow: A Case Study of Dedissa Sub Basin, Abay Basin, South Western Ethiopia. International Journal of Innovations in Engineering Research and Technology, 3.

Geman, H., & Venkatraman, S. (2024). Why Everywhere Seems to Be Flooding Right Now. *Vox*. Retrieved from https://www.vox.com.

Getachew, R. (2018). Simulation of runoff considering the historical impacts of land use and land cover and future climate change: A case study of the Anger sub-basin. Master's thesis, Addis Ababa University, 110 pages.

Getahun, Y.S. and Van Lanen, H.A.J. (2020). Assessing the impacts of land use-cover hydrology of Melka Kuntrie subbasin in Ethiopia, using a conceptual hydrological model Hydrology: Current Research, 6(3), pp.1.

Gomez, C., White, J. C., and Wulder, M. A. (2016). A comprehensive review of optical remotely sensed time series data for land cover classification. ISPRS Journal of Photogrammetry and Remote Sensing, 116, 55-72.

Hailemariam, K. (1999). Impact of climate change on the water resources of Awash River Basin, Ethiopia. *Climate Research,* Vol. 12:91-96.

Hartmann, D. L., Klein Tank, A. M. G., Rusticucci, M., & Alexander, L. V. (2013). Observations: Atmosphere and Surface. *Climate Change 2013: The Physical Science Basis*. Contribution of Working Group I to the Fifth Assessment Report of the Intergovernmental Panel on Climate Change.

Hurni, H., et al. (2016). "Impacts of climate change on Ethiopian agriculture and water resources." *Environmental Systems Research*, 5(1), 1-10.

Intergovernmental Panel on Climate Change (IPCC). (2021). *Climate Change 2021: The Physical Science Basis. Contribution of Working Group I to the Sixth Assessment Report of the IPCC.* Retrieved from https://www.ipcc.ch.

IPCC, 2019. *Climate Change and Land: IPCC Special Report on Climate Change, Desertification, Land Degradation, Sustainable Land Management, Food Security, and Greenhouse Gas Fluxes in Terrestrial Ecosystems*, 1–1542.

IPCC. (2013). IPCC The physical science basis. Contribution of working group I to the assessment report of the intergovernmental panel on climate change, pp.159 254 Cambridge, UK and New York: Cambridge University Press, NY, 1535 pp.

IPCC. (2014). Summary for Policymakers integrated view of climate change as the final part the IPCC's Fifth Assessment Report (AR5). Cambridge, UK: Cambridge University Press.

IPCC-TGICA, A., 2007. General guidelines on the use of scenario data for climate impact and adaptation assessment (p. 66). Version 2. Tech. rep.

Jothityangkoon, C., Zhou, X., & Xie, H. (2021). Framework for simulating rainfall-runoff under future climate scenarios in Southeast Asia. *Water Resources Research*.

Kaini S, Nepal S, Pradhananga S, Gardner T, Sharma AK (2020) Representative models and downscaling of climate data for the transboundary Koshi river basin in China Nepal International Journal of Climatology 40(9):4131–4149, DOI 10.1002/joc.6447

Kifle, S., Ayele, S., & Teshome, W. (2021). The impact of land use change on rainfall-runoff processes in the Blue Nile Basin. *Journal of Hydrology*.

Kinati Chimdessa, S. Quraishi, Asfaw Kebede, Tena Alamirew, (2019). Effect of land use cover climate Change on river flow and soil loss in Didessa River Basin, Southest Blue Nile Ethiopia. Hydrology 6(1), p.2.

Kriegler, E., et al. (2013). The Shared Socioeconomic Pathways: An Overview. *Global Environmental Change*, 22(4), 1177–1187.

Laprise, Tete et al. (2013.). Climate projections over CORDEX Africa domain using the fifth generation Canadian Regional Climate Model (CRCM5). . Climate Dynamics, 41(11-12), pp.3219-3246.

Lemesa Muleta, 2017. Impact of climate change on water availability in the Genale River sub-basin, southeastern Ethiopia (Doctoral dissertation, Haramaya University).

Liu, H., Zhang, S., & Xu, Y. (2022). Effects of urbanization on rainfall-runoff processes in the Yangtze River Basin. *Urban Water Journal*.

Long S-M, Li G (2021) Model uncertainty in the projected Indian summer monsoon change under low-emission scenarios. Atmosphere 12(2):248

Maloney ED, Camargo SJ, Chang E, Colle B, Fu R, Geil KL, Karnauskas, C KBJJO (2014). North American Climate in CMIP5 Experiments: Part III: Assessment of Twenty-First-Century Projections, URL https://doi.org/10.1175/JCLI-D-13-00273.1

Mammo, A. (2017). "Impact of climate change on water resources and water availability in Ethiopia." *Environmental Change and Security Program Report*, 22(1), 1-10.

Mansour, Almazroui, Fahad, Saeed, Sajjad, Saeed, Muhammad, Ismail, Azhar, Ehsan, M., Nazrul, Islam, Muhammad, Abid, Adnan, Enda, O'Brien, Kamil, Shahzad, Ur Rashid, Imran, Nadeem, 2021. Projected changes in climate extremes using CMIP6 simulations over SREX regions. *10.1007/S41748-021-00250-5.*

McDonnell, J. J., et al. (2020). The complexities of rainfall-runoff processes in forested watersheds. *Hydrological Processes*.

Megersa Adugna Nura Boru and Abebe Debele, 2021. Modeling climate change impact on the streamflow in the Upper Wabe Bridge Watershed in the Wabe Shebele River Basin, Ethiopia. *International Journal of River Basin Management*, (just-accepted), pp. 1-46.

Mekasha, T. (2014). Trends in daily observed temperature and precipitation extremes over three Ethiopian eco-environments. International Journal of Climatology, 34(6), 1990–1999.DOI: 10.1002/joc.3816

Mekonnen, A., & Ludi, E. (2018). "Climate change and its implications on rainfed agriculture in Ethiopia." *Environmental Systems Research*, 5(1), 1-10.

Mekonnen, B., Asfaw, H., & Zewdie, Y. (2023). Combined impacts of LULC and climate change on the hydrology of the Birr River watershed, Ethiopia. *Journal of* Environmental Studies, 76(1),49–64.https://doi.org/10.1177/11786221231200106

Mesfin Reta, 2018. Impact of land use and land cover change on streamflow using MIKE SHE: Case study of Shaya watershed, Ethiopia.

Mesgana, Seyoum, Gizaw, Getu, Fana, Biftu, Thian, Yew, Gan, Semu, Ayalew, Moges, Harri, Koivusalo, 2017. Potential impact of climate change on streamflow of major Ethiopian rivers. *Climatic Change*, 10.1007/S10584-017-2021-1.

Mishra, V.N., and Rai, P.K., 2016. A remote sensing aided multi-layer perceptron Markov chain analysis for land use and land cover change prediction in Patna district (Bihar), India. *Arabian Journal of Geosciences*, 9(4): 1-18.

Moges Kidane, Alemu Bezie, Nega Kesete, and Tefere Tolessa, 2019. The impact of land use and land cover (LULC) dynamics on soil erosion and sediment yield in Ethiopia. *Heliyon*, 5(12), p. e02981.

Mostafa, Abdel-Hameed, Mohamed, Mohamed, El-Sayed, El-Mahdy, 2021. Evaluation of climate change impact on extreme temperature variability in the Blue Nile Basin, Ethiopia. 10.5194/GI-10-45-2021.

National Centers for Environmental Information. (2023). Global Climate Report - Annual 2023. *National Oceanic and Atmospheric Administration*. Retrieved from https://www.ncei.noaa.gov.

Negash Tessema, Asfaw Kebede, Dame Yadeta, 2020. Modeling the effects of climate change on streamflow using climate and hydrological models: the case of the Kesem sub-basin of the Awash River basin, Ethiopia. *International Journal of River Basin Management*, pp. 1-12.

Neitsch, S.L., Arnold, J.G., Kiniry, J.R., & Williams, J.R. (2011). *Soil and Water Assessment Tool Theoretical Documentation Version 2009*. Texas Water Resources Institute.

Nguyen, T., Li, Y., & Zhou, W. (2023). *The combined effects of climate and land-use changes on river runoff: A case study using the SWAT model*. Hydrological Research Letters, 18(2), 75–89.

Ning, T., Li, Z. and Liu, W., (2016). Separating the impacts of climate change and land alteration runoff reduction in the Jing River watershed of China. Catena, 147, pp.80-86

O'Neill, B. C., et al. (2017). The Scenario and the Implications of SSPs. *Nature Climate Change*, 7, 703–709.

Parsa, V.A., Yavari, A., Nejadi, A., 2016. Spatio-temporal analysis of land use/land cover pattern changes in Arasbaran Biosphere Reserve, Iran. *Modeling Earth Systems and Environment*, 2(4): 178.

Per-Erik, Mellander, Solomon, Gebreyohannis, Gebrehiwot, Annemieke, Gärdenäs, Woldeamlak, Bewket, Kevin, Bishop, 2013. Summer rains and dry seasons in the upper Blue Nile Basin: the predictability of half a century of past and future spatiotemporal patterns. *PLOS ONE*, 10.1371/JOURNAL.PONE.0068461.

Priyanka, Jawale, Aruna, Dattatraya, Thube. (2024). Gis Based Hydrological Modelling for Urban Flood Simulation Using Soil and Water Assessment Tool (SWAT). Doi: 10.21203/rs.3.rs-4555982/v1

R., N., Adhikari, S., Chattarajan., US, Pattnaik., MM, Srjvastava. (2022). Rainfall-runoff relationship based on the model of runoff formation at the natural storage. Mausam, 40(3):81-84. Doi: 10.54302/mausam.v40i3.2132

Rajib, A., and Merwade, V., 2017. Hydrologic response to future land use change in the Upper Mississippi River Basin by the end of the 21st century. *Hydrological Processes*, 31(21): 3645-61.

Renaud, F. G., et al. (2017). "The impact of climate change on human migration and displacement." *Environmental Change and Security Program Report*, 22(1), 1-10.

Reuters. (2024). *Africa faces steep costs as temperatures soar, says WMO.* Reuters Climate News. Retrieved from https://www.reuters.com.

Reza, K. (2014). Assessment of Climate Change Impact on Runoff and Peak Flow-A Case Study on Klang Watershed in west Malaysia.

Riahi, K., et al. (2017). The Shared Socioeconomic Pathways and Climate Change Projections. *Climate Change*, 3(5), 268–285.

Rwigi, S.K., (2014). Analysis of Potential Impacts of Climate Change and Deforestation Surface Yields from the Mau Forest Complex Watersheds in Kenya (Doctoral Dissertation University of Nairobi).

Sahalu, Atalel, 2014. Analysis of urban land use and land cover changes: a case of study in Bahir Dar, Ethiopia (Doctoral dissertation).

Samuel K., Abdella K., & Santosh M.P, (2016). The impact of land use land cover change on watershed hydrology (a case study upper awash basin). DOI: https://doi.org/10.59122/13529D1

Shimeles Molla. (2017). Assessment of Climate Change Impact on streamflow of Baro- River Basin Case study of Baro Watershed.

Shimelis, Gebriye, Setegn, Assefa, M., Melesse, David, Rayner, Bijan, Dargahi, 2014. Climate change impact on water resources and adaptation strategies in the Blue Nile River Basin. *10.1007/978-3-319-02720-3_20.*

Shrestha, R. R., et al. (2021). Evaluating the uncertainties in hydrological response to change considering multiple land use scenarios. Journal of Hydrology, 599, 126681.

Sigmond, M., Anstey, J., Arora, V., Digby, R., Gillett, N., Kharin, V., Merryfield, W., Reader, C., Scinocca, J., Swart, N., Virgin, J., Abraham, C., Cole, J., Lambert, N., Lee, W.-S., Liang, Y., Malinina, E., Rieger, L., von Salzen, K., … Yang, D. (2023). Improvements in the Canadian Earth System Model (CanESM) through systematic model analysis: CanESM5.0 and CanESM5.1. *Geosci. Model Dev.*, *16*, 6553–6591. https://doi.org/10.5194/gmd-16-6553-2023

Simane, B., Beyene, H., Deressa, W., Kumie, A., & Berhane, K. (2022). Review of Climate Change and Health in Ethiopia. *The Ethiopian Journal of Health Development*, 36(2).

Sisay Nune, Teshome Soromessa and Demel Teketay. (2016). Land use land cover change in the Bale Mountain Eco-Region of Ethiopia during 2000 to 2020. Land, 5(4), p.41.

Smith, R., Peterson, A., & Evans, B. (2020). *Comparative evaluation of CMIP5 and CMIP6 models for hydrological modeling*. Climate Dynamics, 45(2), 215–230.

Stouffer RJ, Eyring V, Meehl GA, Bony S, Senior C, Stevens B, Taylor K (2017) scientific gaps and recommendations for CMIP6. Bull Am Meteorol Soc 98(1):95–105

Subramanya, K., 2013. Hydraulic machines. Tata McGraw-Hill Education.

Swart, N.C., Cole, J., Kharin, S., Lazare, M., Scinocca, J., Gillett, N., Anstey, J., Arora, V., Christian, J., Hanna, S., Jiao, Y., Lee, W., Majaess, F., Saenko, O., Seiler, C., Seinen, C., Shao, A., Solheim, L., von Salzen, K., Yang, D., and Winter, B., 2019. The Canadian Earth System Model (CanESM), v5.0.3. https://doi.org/10.5281/zenodo.3251114.

Tadese, M., Kumar, L., Koech, R., and Kogo, B.K., 2020. Mapping land-use/land-cover changes and its dynamics in the Awash River Basin using remote sensing and GIS. *Remote Sensing Applications: Society and Environment*, 19(December 2019), 100352. https://doi.org/10.1016/j.rsase.2020.100352.

Tadesse, T., et al. (2016). "Climate change and its implications for rainfed agriculture in Ethiopia." *Environmental Systems Research*, 5(1), 1-10.

Tariku, G., et al. (2021). "Hydrologic extremes in the upper Blue Nile under future climate scenarios." *Water Resources Research*, 57(9), 1-15.

Tariku, T. B., (2021). Impact of Climate Change on Hydrology and Hydrologic Extremes Upper Blue Nile River Basin. Journal of Water Resources Planning and Management, 147(204020104. https://doi.org/10.1061/ (ASCE) wr.1943-5452.0001321

Tassew, B.G., Belete, M.A., Miegel, K., (2019). Application of HEC-HMS model for flow. Simulation in the Lake Tana Basin: the case of Gilgel Abay Watershed, Upper Blue Nile Basin, Ethiopia. Hydrology 6 (21). https://doi.org/10.3390/hydrology6010021.

Taylor, K.E., Stouffer, R.J. and Meehl, G.A., 2012. An overview of CMIP5 and the experiment design. *Bulletin of the American meteorological Society*, 93(4), pp.485-498.

Tekalegn Ayele, Nadir Ahmed, L. Ribbe, and J. Heinrich., (2018). Watershed response to climate and land use changes in the Upper Blue Nile sub-basins, Ethiopia. Science of the total environment, 644, pp.193-206.

Temesgen Gashaw, Taffa Tulu, Mekuria Argaw, Abeyou W., Terefe Tolessa, and Mengistie Kindu, 2018. Estimating the impacts of land use/land cover changes on Ecosystem Service Values: The case of the Andassa watershed in the Upper Blue Nile basin of Ethiopia. *Ecosystem Services*, 31, pp. 219-228.

Tesfa Worku Meshesha, Sangharsh Kumar Tripathi, (2016). Farmer's Perception on Soil Erosion and Land Degradation Problems and Management Practices in the Beressa Watershed of Ethiopia. *J Water Resources Ocean Sci*. 2016; 5(5):64-72. Doi: 10.11648/j.wros.20160505.11

Tesfaye Gragn, Asfaw Kebede and Shimelies Berhanu, 2019. Evaluation of climate change impacts on the water resources of Awata River Watershed, Genale Dawa Basin: Southern Ethiopia.

Tessema, Z. K., et al. (2016). "Climate change and its implications on rainfed agriculture in Ethiopia." *Environmental Systems Research*, 5(1), 1-10.

Tigabu, T. B., Wagner, P. D., Hörmann, G., Kiesel, J., & Fohrer, N. (2021). Climate impacts on the water and groundwater resources of the Lake Tana Basin, Ethiopia. Journal of and Climate Change, 12(5), 1544–1563. https://doi.org/10.2166/wcc.2020.126

Touré, Kyei-Baffour et al. (2017). Assessment of changing trends of daily precipitation and temperature extremes in Bamako and Segou in Mali from 1961–2014. . Weather Clim. Extrem., 18, 18-16. DOI: 10.1016/j.wace.2017.09.002

Trzaska S, & Schnarr E (2014). A review of downscaling methods for climate change projections United States Agency for International Development by. Tetra Tech ARD pp 1–42

Tufa Negewo and A.K. Sarma, 2021. Evaluation of climate change-induced impact on streamflow and sediment yield of Genale Watershed, Ethiopia.

United Nations Framework Convention on Climate Change (UNFCCC). (2024). *Climate change is an increasing threat to Africa.* UNFCCC Newsroom. Retrieved from https://unfccc.int.

Van Vuuren, D. P., et al. (2013). The Shared Socioeconomic Pathways: A Framework for Climate Change Research. *Global Environmental Change*, 22(4), 204–211.

Van Vuuren, D.P., and Oostenrijk, R., (2011). RCP2. 6: exploring the possibility to keep global mean temperature increase below 2 C. Climatic change, 109(1), pp.95-116.

Wakjira Takala, K. Miegel, and Tamene A. Demissie, 2020. Watershed hydrological response to combined land use/land cover and climate change in highland Ethiopia: Fincha'a watershed. *Water*, 12(6), p. 1801.

Wassie S. B. (2020). Natural resources degradation tendencies in Ethiopia: a review. Environmental Systems Research 9 (1), 33. https://doi.org/10.1186/s40068-020-00194-1.

Water Utility Climate Alliance (WUCA). (2018). *Training on downscaling techniques: Statistical and dynamical approaches*. Retrieved from WUCA Online.

Wilby & Dawson. (2007). Statistical Downscaling Model SDSM, Version 4.2 User Manual. UK.

Wilby, R. L., & Dawson, C. W. (2013). The Statistical Downscaling Model: insights from one decade of application. *Int. J. Climatol.*, *33*, 1707–1719. https://doi.org/10.1002/joc.3544

Woldeamlak Bewket and Solomon Abebe, S., 2013. Land-use and land-cover change and its environmental implications in a tropical highland watershed, Ethiopia. *International Journal of Environmental Studies*, 70(1), pp. 126-139.

Woldesenbet T. A., Elagib N. A., Ribbe L. & Heinrich J. (2018). Watershed response to climate and land use changes in the Upper Blue Nile sub-basins, Ethiopia. Science of the Total Environment 644, 193–206. https://doi.org/10.1016/j.scitotenv.2018.06.198.

Worku, G., Teferi, E., Bantider, A., & Dile, Y. T. (2021). Modelling processes under change scenarios in the Jemma sub-basin of upper Blue Nile Basin, Ethiopia. Climate Management, 31, 100272. https://doi.org/10.1016/j.crm.2021.100272

World Meteorological Organization (WMO). (2024). *Africa faces steep costs as temperatures soar.* World Meteorological Organization News. Retrieved from https://www.wmo.int.

Wuletaw Abera, Lulseged Tamene, Assefa Abegaz and Dawit Solomon, (2019). Understanding climate and land surface changes impact on water resources using Budyko framework and remote sensing data in Ethiopia. Journal of Arid Environments, 167, pp.56-64.

Xiang, Y., Wang, Y. Chen, Y, Zhang, Q. (2021).Impact of Climate Change on the Regime of the Yarkant River Basin, China: An Assessment Using Three SSP Scenarios of GCMs. Remote Sens, 14, 115.

Xie, K., Chen, H., Qiu, Y., Kim, J.-S., Yoon, S.-K., Lin, Y., Liu, B., Wang, J., Chen, J., Zhang, S. (2021). Exploring and Predicting the Individual, Combined, and Synergistic Impact Land-Use Change and Climate Change on Streamflow, Sediment, and Total Loads. Frontiers in Environmental Science, 9, 726793 https://doi.org/10.3389/fenvs.2021.726793

Xu, W., Zhang, Z., & Li, F. (2021). A comparative analysis of rainfall-runoff processes in China. *Journal of Hydrological Engineering*.

Yaari, A. Ducharne., A Thiery, A W., Cheruy, F., & Lawrence, D. (2022). The role of expansion on historical climate change: Insights from CMIP6. Earth's Future, 10, e2022EF002859.

Yang, D., Yang, Y., & Xia, J. (2021). Hydrological cycle and water resources in a world: review. Geography and Sustainability, 2(2), 115–122.https://doi.org/10.1016/j.geosus.2021.05.003

Yang, L., (2017). Identifying separate impacts of climate and land use/cover change hydrological Processes in upper stream of Heihe River, Northwest China. Hydrological Processes, 31(5), pp.1100

Yimer, A. (2018). Evaluation of climate change impact on streamflow of Mille watershed.

Yimer, T., & Bekele, A. (2023). Assessing LULC change impacts on surface water in the Laga-Arba watershed, Awash Basin, Ethiopia. *Water Resources Management*, 37(5), 843–860.https://doi.org/10.1007/s382184962

Yin, J., He, F., & Qiu, G. Y. (2017). Effects of land use/land cover and climate changes Surface runoff in a semi-humid and semi-arid transition zone in northwest China. Hydrol. Earth Syst. Sci, 21, 183–196. https://doi.org/10.5194/hess-21-183-2017

Zhang, Y., Li, L., & Liu, X. (2019). *A comprehensive description of the CanESM5 model and its performance in climate simulations*. Climate Change Review, 32(4), 305–320.

Zhao T, (2017) Uncertainties in historical changes and future projections of drought. Part II: Model Simulated historical and future drought changes. Climate Change 144(3):535–548

Zhou, Y., Xu, Y., Xiao, W., Wang, J., Huang, Y., & Yang, H. (2017). Climate Change Impacts on Flow and Suspended Sediment Yield in Headwaters of High-Latitude Regions—A Case Study in China's Far Northeast. Water, 9(12), 966. https://doi.org/10.3390/w9120966

7. APPENDICES

7.1. Appendix A. Tables

Table 1: List of the 26 Predictor Variable IDs and Corresponding Variable Names

No.	ID	Predictor Variable	No.	ID	Predictor Variable
1	mslp	Mean sea level pressure	14	p8_f	850 hPa Wind Speed
2	p1_f	1000 hPa Wind Speed	15	p8_u	850 hPa Zonal Wind Component
3	p1_u	1000 hPa Zonal Wind Component	16	p8_v	850 hPa Meridional Wind Component
4	p1_v	1000 hPa Meridional Wind Component	17	p8_z	850hPa Relative Vorticity of True wind
5	p1_z	1000hPa Relative Vorticity of True Wind	18	p8th	850 hPa Wind Direction
6	p1th	1000 hPa Wind Direction	19	p8zh	850 hPa Divergence of True Wind
7	p1zh	1000 hPa Divergence of True Wind	20	p500	500 hPa Geopotential
8	p5_f	500 hPa Wind Speed	21	p850	850 hPa Geopotential
9	p5_u	500 hPa Zonal Wind Component	22	prcp	Total Precipitation
10	p5_v	500 hPa Meridional Wind Component	23	s500	500 hPa Specific Humidity
11	p5_z	500 hPa Relative Vorticity of True Wind	24	s850	850 hPa Specific Humidity
12	p5th	500 hPa Wind Direction	25	shum	1000 hPa Specific Humidity
13	p5zh	500 hPa Divergence of True Wind	26	temp	Air Temperature at 2 m

Table 2: Mean Monthly Flow for LULC under Baseline and Future Periods

	Past Land Use Land Cover			Future Land Use Land Cover	
Month	LULC 2000	LULC 2010	LULC 2020	LULC 2030	LULC 2050
JAN	18.57	18.63	18.12	18.23	18.48
FEB	12.89	12.42	12.12	12.46	12.05
MAR	20.58	20.16	20.87	21.57	21.92
APR	67.58	67.58	66.59	67.75	68.73
MAY	88.32	89.35	89.64	92.06	93.17
JUN	53.82	54.08	54.16	52.26	51.28
JUL	44.75	43.54	42.64	42.45	41.4
AUG	42.13	43.21	44.84	45.67	45.88
SEP	45.26	45.51	46.98	46.37	46.78
OCT	81.17	82.4	82.87	83.46	84.97

NOV	61.06	62.37	65.19	66.22	67.63
DEC	37.77	37.26	37.11	36.39	35.79
Annual	573.9	576.5	581.14	584.9	588.06

Table 3: Major soil type of the Mille watershed

No	Soil Types	Area in (ha)	Area in (KM^2)	Area in (%)
1	Eutric Cambisols	240562.7	2405.63	41.41
2	Lithosols	40409.7	404.1	6.96
3	Calcic Xerosols	218093.9	2180.94	37.55
4	Eutric Gleysols	81755.9	817.56	14.07
5	Calcic Xerosols	49.4	0.49	0.01

Table 4: Meteorological data used for SWAT model (1992-2023) for Mille Stations

Mille Rainfall Station												
Description	Jan	Feb	Mar	Apr	May	Jun	Jul	Aug	Sep	Oct	Nov	Dec
PCP_MM	6.26	6.66	24.4	29.3	12.2	11.7	65.0	84.4	33.0	11.9	7.28	7.76
PCPSTD	0.65	1.29	3.14	2.64	1.27	1.29	2.98	4.69	2.36	1.33	1.23	1.51
PCPSKW	4.36	11.4	9.9	6.33	8.64	6.86	2.94	4.87	5.44	8.96	9.21	12.6
PR_W1	0.08	0.07	0.13	0.19	0.15	0.19	0.35	0.54	0.28	0.07	0.04	0.04
PR_W2	0.66	0.55	0.68	0.73	0.59	0.57	0.84	0.8	0.74	0.64	0.6	0.66
PCPD	5.78	4.31	9.31	13.1	8.75	9.56	21.9	23.6	16.9	6.75	3.69	3.75
TMPMX	33.83	35.2	37.3	38.9	40.7	42.3	39.3	37.4	37.8	36.6	35.6	33.9
TMPMN	20.3	22.7	24.3	26.0	27.1	28.7	27.8	26.7	26.4	22.5	20.6	18.9
TMPSTDMX	2.23	3.77	2.66	2.31	2.2	2.95	2.51	2.01	1.77	2.18	1.83	2.08
TMPSTDM	4.4	4.87	3.64	3.03	2.82	2.57	2.7	2.34	3.15	3.7	4.2	4.44
RAINHHMX1	0.63	0.97	3.02	2.8	1.38	1.4	3.73	5.18	2.71	1.38	1.14	1.18
SOLARAV1	5.9	6.57	7.56	10.0	9.7	9.26	9.7	10.3	9.68	7.37	5.2	6.2
DEWPT1	0.55	0.53	0.5	0.48	0.47	0.36	0.43	0.57	0.47	0.43	0.48	0.51
WNDAV1	3.03	3.12	3.14	3.13	3.08	3.25	3.27	2.98	2.55	2.65	2.9	3.01

Table 5: Meteorological data used for SWAT model (1992-2023) for Bati Stations

Bati Rainfall Station												
Description	Jan	Feb	Mar	Apr	May	Jun	Jul	Aug	Sep	Oct	Nov	Dec
PCP_MM	40.3	38.75	72.89	80	75.21	51.7	183.63	196.19	96.57	54.36	54.22	42.9
PCPSTD	4.28	4.91	7.47	7.36	7.91	6.14	10.56	10.57	7.49	5.48	7.23	5.25
PCPSKW	5.69	6.43	5.19	4.73	6.53	7.38	3.02	2.64	4.53	5.1	7.65	5.79
PR_W1	0.12	0.12	0.16	0.23	0.17	0.14	0.45	0.48	0.3	0.11	0.1	0.09
PR_W2	0.74	0.77	0.7	0.6	0.64	0.68	0.7	0.7	0.63	0.73	0.76	0.78
PCPD	10.44	10.28	11	11.11	10.15	9.57	18.73	19.17	13.57	9.42	9.2	9.13
TMPMX	24.81	25.8	27.81	29.25	30.54	32.61	30.43	28.71	28.85	28.22	26.9	25.46
TMPMN	10.22	11.6	12.93	14.11	14.92	16.07	15.98	15.22	14.34	11.28	10.01	9.35
TMPSTDMX	2.24	4.19	2.48	2.14	3.25	1.71	2.21	1.62	1.52	1.48	1.63	1.75
TMPSTDM	4.13	4.72	3.58	3.03	3.21	3.09	2.55	2.37	2.61	3.47	3.67	4.18
RAINHHMX1	4.96	5.15	8.88	9.08	9.73	6.89	12.59	12.03	9.52	6.78	7.35	4.72
SOLARAV1	7.9	8.57	9.56	12.04	11.7	11.26	11.7	12.32	11.68	9.37	7.2	8.2
DEWPT1	0.73	0.67	0.66	0.64	0.57	0.5	0.62	0.7	0.68	0.63	0.65	0.67
WNDAV1	0.75	0.83	0.89	0.84	0.84	0.98	1.07	0.94	0.64	0.58	0.69	0.71

Table 6: Meteorological data used for SWAT model (1992-2023) for Mersa Stations

Mersa Rainfall Station												
Description	Jan	Feb	Mar	Apr	May	Jun	Jul	Aug	Sep	Oct	Nov	Dec
PCP_MM	36.37	35.39	86.58	94.99	65.41	38.63	242.91	265.96	101.85	48.91	36.26	33.86
PCPSTD	5.87	6.4	7.91	7.75	6.13	4.82	11.93	11.99	7.79	5.58	5.34	6.28
PCPSKW	13.59	8.88	4.49	4.59	4.07	6.95	2.15	2	3.62	6.45	6.88	9.33
PR_W1	0.08	0.06	0.14	0.17	0.14	0.1	0.42	0.49	0.24	0.11	0.06	0.05
PR_W2	0.61	0.58	0.62	0.62	0.53	0.45	0.7	0.73	0.58	0.47	0.55	0.51
PCPD	5.46	3.84	8.4	9.46	7.4	4.71	18.18	20.03	11.18	5.65	3.68	3.09
TMPMX	26.9	27.69	28.76	29.86	31.29	32.51	30.71	29.41	29.58	28.74	27.98	26.92
TMPMN	11.35	11.7	12.87	14.16	14.59	14.89	14.84	14.17	13.66	12.06	11.19	10.13

TMPSTDMX	2.22	2.33	2.32	1.94	2.26	2.19	2.09	1.71	1.61	1.75	1.78	1.89
TMPSTDM	3.08	3.07	2.78	2.12	1.88	1.96	2.04	2.13	2.09	2.44	2.92	3.38
RAINHHMX1	5.24	4.99	9.86	9.24	7.28	5.95	14.25	14.36	10.05	7.23	5.67	4.36

Table 7: Mean monthly flow for climate change only simulation under SSP2-4.5 and SSP5-8.5

	Land Use Near future 2030 (2025-2055) and Land Use Mid future 2050 (2056-2085)			
Month	Near-term SSP2-4.5	Mid-term SSP2-4.5	Near-term SSP5-8.5	Mid-term SSP5-8.5
JAN	22.99	25.89	24.23	24.92
FEB	11.94	11.61	11.7	10.97
MAR	27.31	26.06	27.23	24.05
APR	77.08	76.77	71.56	71.95
MAY	126.45	124	121	120.59
JUN	61.91	58.51	59.52	56.72
JUL	35.14	32.61	33.54	32.15
AUG	16.05	16.69	15.25	17.32
SEP	26.92	20.84	26.42	21.47
OCT	95.13	105.59	95.43	106.25
NOV	83.41	86.06	86.09	85.43
DEC	41.13	44.42	42.66	44.57
Annual	625.46	629.06	614.61	616.4

Table 8: Mean monthly Flow for Combined simulation under SSP2-4.5 and SSP5-8.5

	Land Use 2030 (2025-2055)		Land Use 2050 (2056-2085)	
Month	Near-term SSP2-4.5	Near-term SSP5-8.5	Mid-term SSP2-4.5	Mid-term SSP5-8.5
JAN	23.05	24.31	26.54	25.53
FEB	11.92	11.69	11.85	11.15
MAR	27.17	27.09	25.06	23.16
APR	77.2	71.73	74.68	70.22
MAY	127.24	121.81	124.23	121.11
JUN	62.91	60.51	62	60.28

JUL	35.66	34.05	34.44	33.99
AUG	16.19	15.36	17.15	17.74
SEP	26.79	26.27	20.3	20.82
OCT	95.07	95.33	103.42	103.73
NOV	83.67	86.33	87.14	86.28
DEC	41.48	43.03	46.42	46.44
Annual	628.36	617.52	633.23	620.47

Table 9: Projected maximum and minimum Temperature for near and midterm under SSP2-4.5 and SSP5-8.5 Scenarios.

Baseline		Max Temp SSP2-4.5		Max Temp SSP5-8.5	
	Tmp Max	Near SSP2-4.5	Mid SSP2-4.5	Near SSP5-8.5	Mid SSP5-8.5
JAN	33.32	33.55	33.85	33.56	34
FEB	36.32	36.03	35.88	36.01	35.7
MAR	37.6	37.72	37.78	37.84	37.95
APR	39.13	39.14	39.08	39.15	39.09
MAY	40.73	41.06	41.27	41.04	41.43
JUN	42.73	43.37	43.93	43.34	44.09
JUL	39.45	39.62	39.88	39.61	39.95
AUG	37.91	38.46	38.89	38.63	39.29
SEP	38.72	39.21	39.35	39.02	39.27
OCT	37.29	37.93	38.2	37.83	38.5
NOV	35.31	35.19	35.14	35.15	35.04
DEC	33.49	33.37	33.27	33.31	33.14
Annual	37.67	37.89	38.04	37.87	38.12
	Tmp Min	Near SSP2-4.5	Mid SSP2-4.5	Near SSP5-8.5	Mid SSP5-8.5
JAN	21.08	20.96	21.02	20.94	20.95
FEB	23.98	23.95	23.89	23.92	23.85
MAR	25.02	25.06	25.14	25.1	25.47

APR	26.62	26.34	26.18	26.29	25.95
MAY	28.12	27.7	27.43	27.78	27.32
JUN	29.03	28.82	28.79	28.81	28.64
JUL	27.8	28.75	29.51	28.94	30.32
AUG	27.34	26.81	26.33	26.12	25.57
SEP	25.71	26.07	26.57	26.56	27.83
OCT	22.73	23.75	24.38	23.96	25.32
NOV	18.91	18.86	18.94	18.84	18.63
DEC	17.57	17.34	17.17	17.2	16.72
Annual	24.49	24.53	24.61	24.54	24.71

Table 10: Projected mean monthly and % of rainfall under SSP2-4.5 and SSP5-8.5

		SSP2-4.5				SSP5-8.5			
Month	A	NRF	%	MRF	%	NRF	%	MRF	%
JAN	4.82	4.8	-0.5	4.58	-4.9	4.94	2.5	4.25	-11.7
FEB	5.54	7.7	39	8.45	52.4	8.15	47.1	11.42	106
MAR	21.91	20.85	-4.8	21.36	-2.5	21.85	-0.3	21	-4.2
APR	27.62	25.68	-7	25.39	-8	24.02	-13	23.86	-13.6
MAY	10.21	10.24	0.3	10.4	1.9	10.25	0.4	10.61	3.9
JUN	5.83	8.66	48.6	8.98	54.1	9.03	54.8	11.37	94.9
JUL	62.17	62.71	0.9	63.14	1.6	62.92	1.2	64.75	4.2
AUG	79.64	80.02	0.5	78.74	-1.1	78.87	-1	78.56	-1.4
SEP	21.48	28.65	33.4	35.57	65.6	34.19	59.1	55.02	156.1
OCT	9.88	10.81	9.4	11.88	20.3	11.01	11.5	12.2	23.5
NOV	10.8	14.21	31.6	17.33	60.4	15.04	39.3	21.34	97.6
DEC	9.43	10.15	7.6	10.27	9	10.31	9.4	9.86	4.6

Note: A = Represent observed rainfall, **NRF** = Near-term rainfall, **MRF** = mid-term rainfall

% = percentage change of future rainfall from baseline period.

7.2. Appendix B. Figures

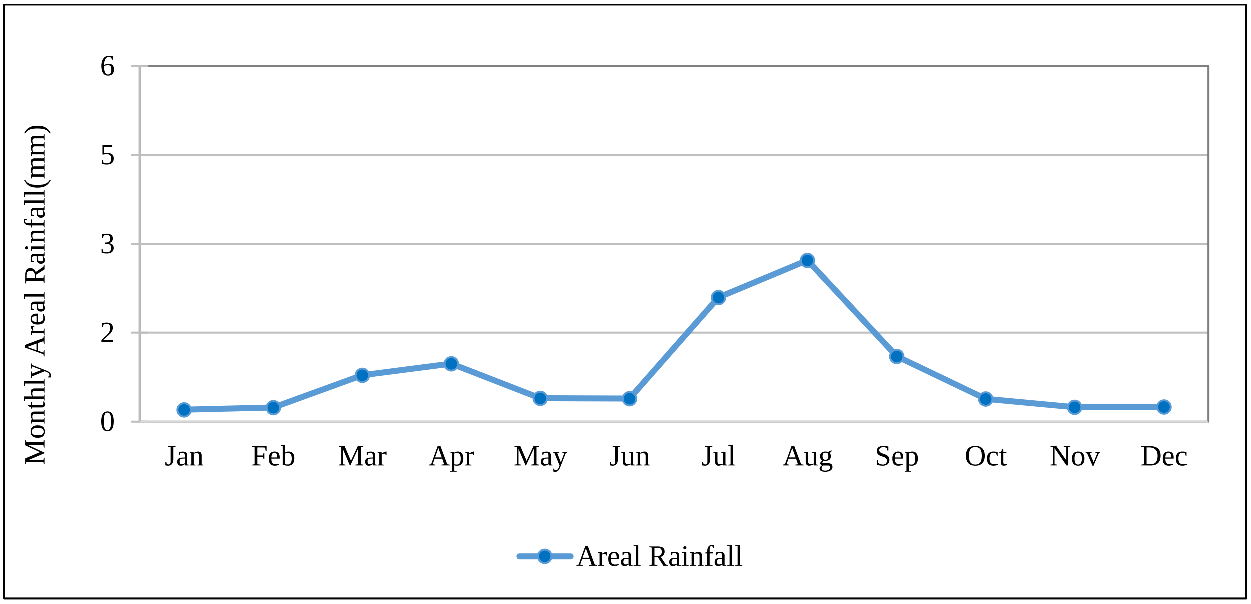

Figure 1: Mean areal Rainfall of the watershed from (1992-2023)

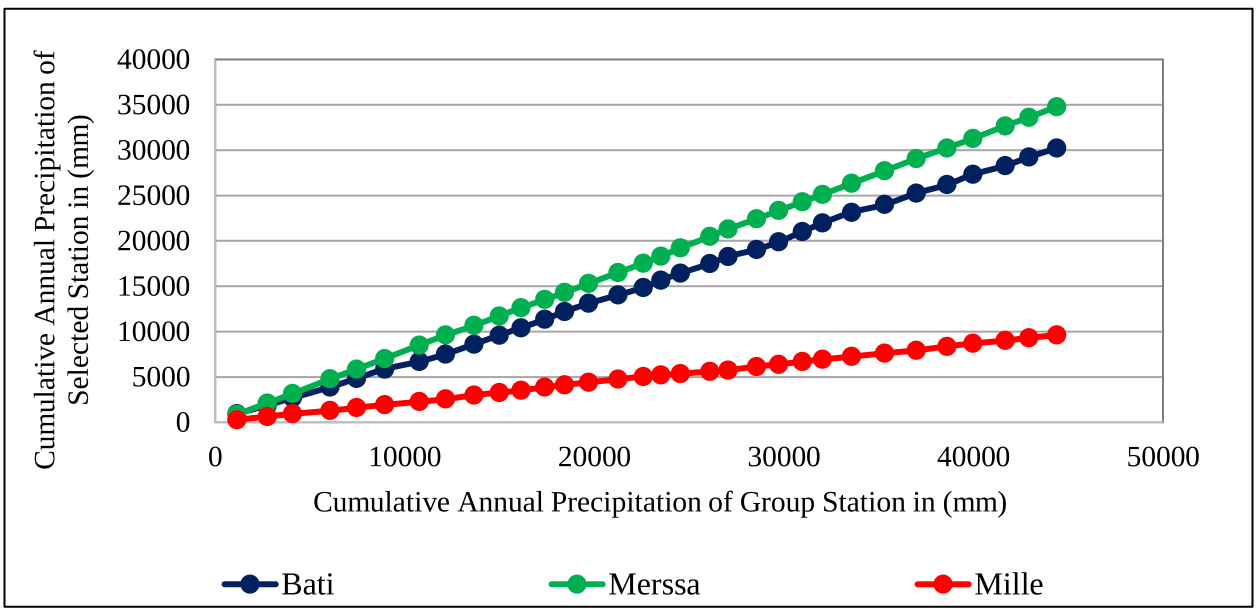

Figure 2: Double Mass Curves for the Station

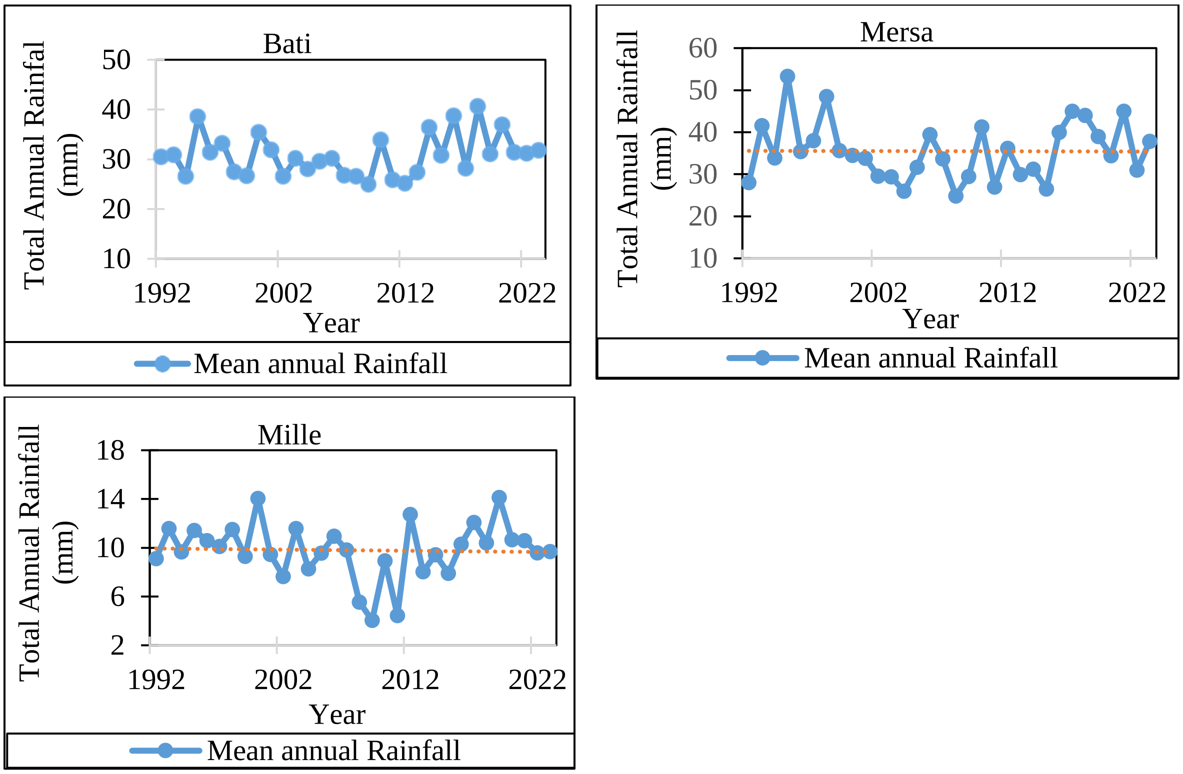

Figure 3: Homogeneity Tests for Annual Rainfall Data from Individual Rain Gauge Stations

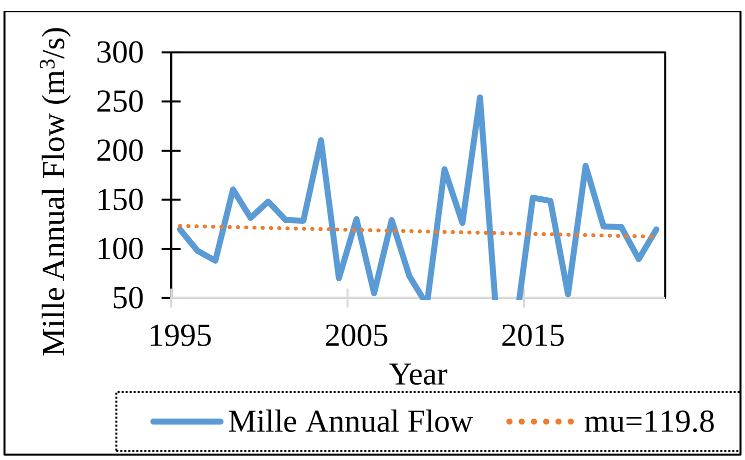

Figure 4: Pettitt's Homogeneity Test for Annual Streamflow Data

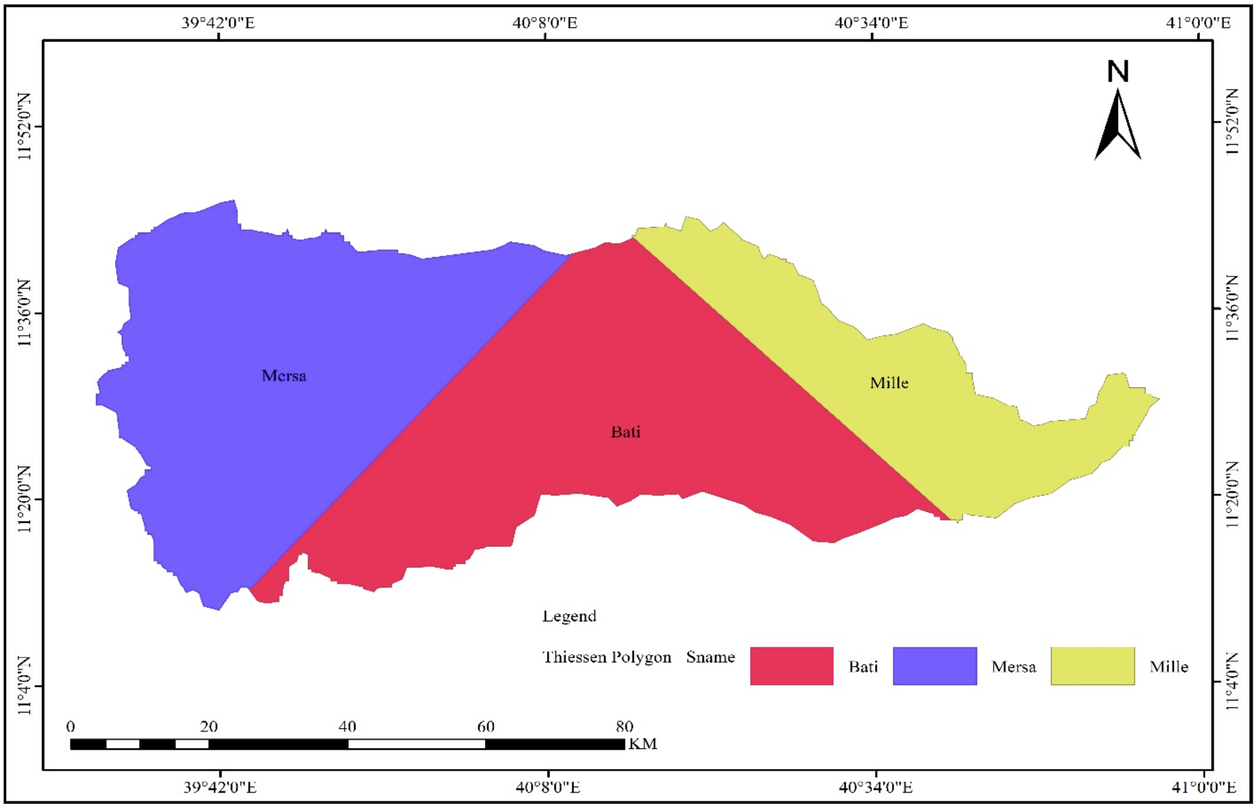

Figure 5: Thiessen polygon of the station

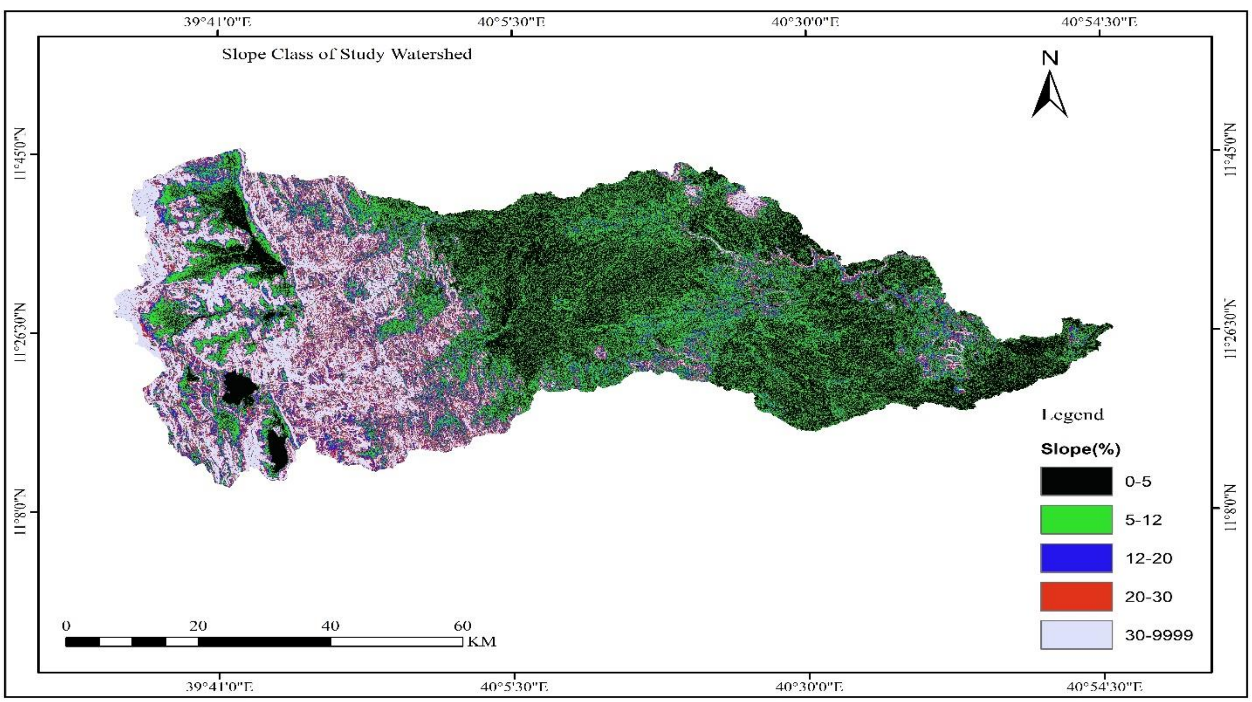

Figure 6: Slope Class Map of Study Area

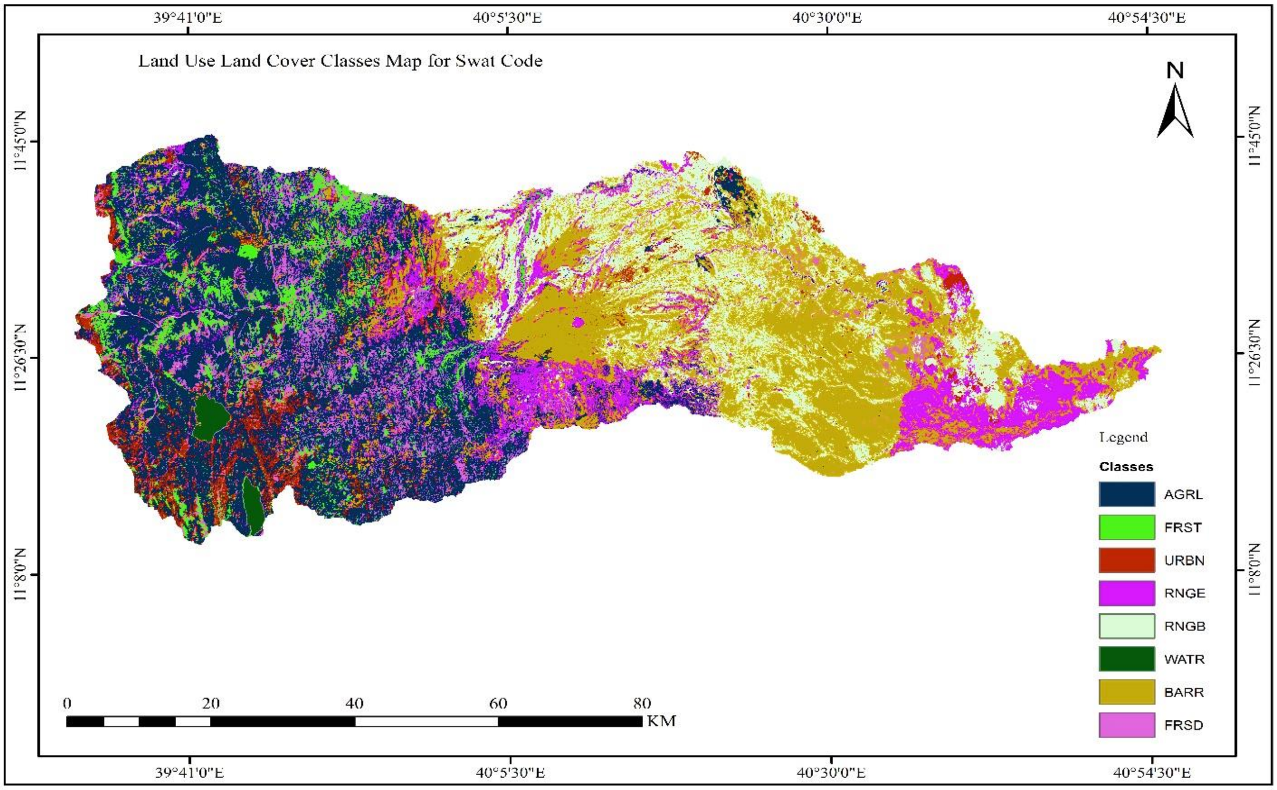

Figure 7: Land Use Land Cover Map for Swat Code

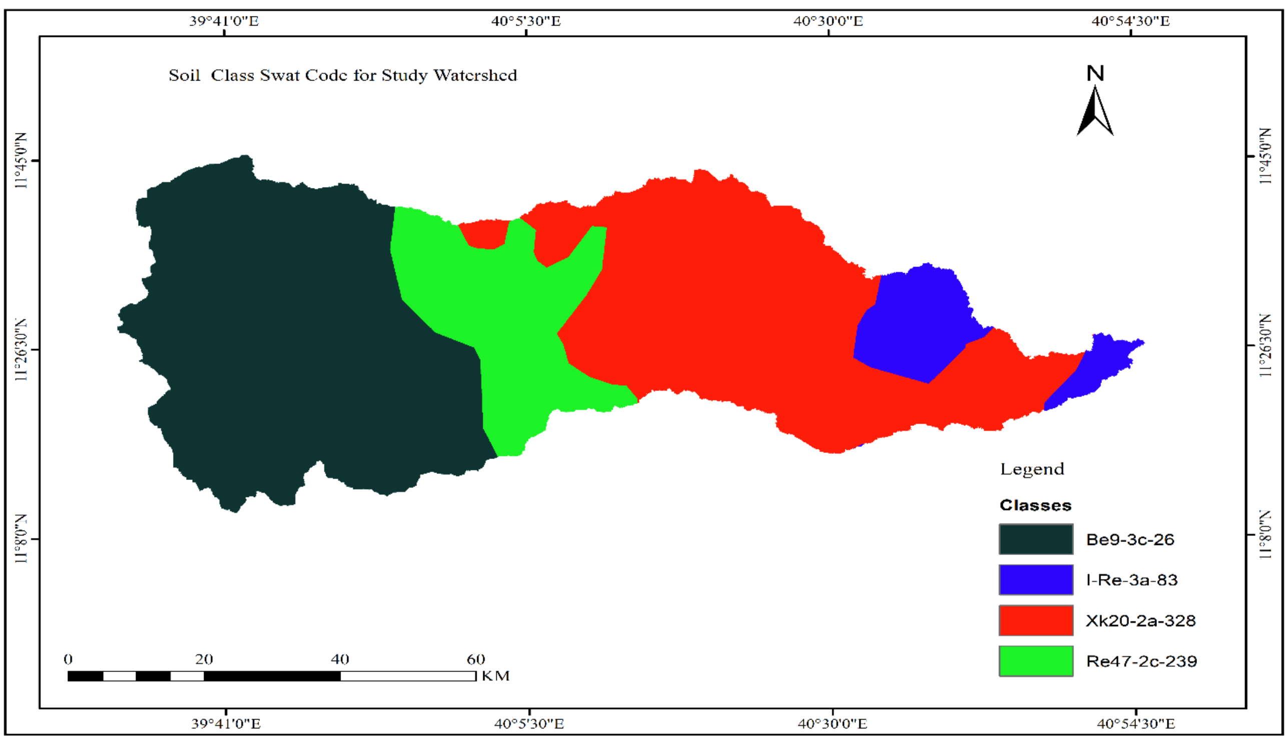

Figure 8: Soil Map for Swat Code